

Modulation of Incommensurately Modulated Structures Studied by the Maximum Entropy Method

Von der Universität Bayreuth
zur Erlangung der Grades eines
Doktors der Naturwissenschaften (Dr. rer. nat.)
genehmigte Abhandlung

von
Li Liang
aus Jinan, China

1. Gutachter: Prof. dr. Sander van Smaalen
2. Gutachter: PD. Dr. Natalia Dubrovinskaia

Tag der Einreichung: 26. 10. 2010

Tag der Kolloquiums: 17. 01. 2011

以此文献给生我养我的母亲齐芬，父亲李道渭。

Contents

1	Introduction	1
2	Aperiodic crystallography and superspace	3
2.1	Aperiodic crystallography	3
2.1.1	Incommensurate modulated structures	4
2.1.2	Incommensurate composite structures	6
2.1.3	Quasicrystals	7
2.2	Superspace	7
2.2.1	Reciprocal and direct superspace	7
2.2.2	Symmetry in superspace	10
2.3	Modulation functions	12
2.3.1	Different types of modulation functions	13
2.3.2	Modulation functions used in the present thesis	14
3	The Maximum Entropy Method	17
3.1	Applications of the MEM	17
3.2	Principle of the MEM - BayMEM	18
4	Integration of aperiodic crystals diffraction data	23
4.1	The EVAL15 method	23
4.2	Integrating of diffraction data of aperiodic crystals	23
4.3	Case study: data integration of Rb_2ZnCl_4 by EVAL15	25
4.3.1	Indexing of reflections	29
4.3.2	Refinement	30

4.3.3	Finding the \mathbf{q} -vector	35
4.3.4	Integration	38
4.3.5	Data analysis and data reduction	45
4.4	Special problem in CCD detector data integration.	53
5	Incommensurately modulated Rb_2ZnCl_4	57
5.1	Abstract	57
5.2	Introduction	58
5.3	Experimental	61
5.3.1	Crystal growth and the diffraction experiment	61
5.3.2	Structure refinements	65
5.3.3	MEM calculations	68
5.4	Discussion	74
5.4.1	Nature of the modulation	74
5.4.2	Relation to the soliton model	79
5.4.3	Origin of the modulation	81
5.5	Conclusions	82
6	Incommensurately modulated $\text{Cr}_2\text{P}_2\text{O}_7$	85
6.1	Abstract	85
6.2	Introduction	86
6.3	The maximum entropy method	88
6.4	Experimental	93
6.4.1	Structure refinements	93
6.4.2	MEM calculations	96
6.5	Discussion	99
6.6	Conclusions	106
7	Summary	109
8	Zusammenfassung	113
A	Supplementary materials: Rb_2ZnCl_4	119

CONTENTS

iii

Declaration

149

Chapter 1

Introduction

Entropy is a concept used in thermodynamics to describe the state of order of a system. This term is also used as a measure of amount of information in a data set. The Maximum Entropy Method (MEM) is a general method for data analysis, which is employed to extract the maximum amount of information from the data, without the introduction of artifacts or assumptions concerning a model.

In crystallography, MEM has been used to reconstruct the electron density distribution in a unit cell allowed by the X-ray diffraction data. For aperiodic crystals, many more parameters are needed to describe a structure, take the incommensurately modulated structure as an example, which this thesis is focuses on, basic-structure, atomic displacement parameters (ADPs) and an infinite number (in principle) of parameters defining the modulation functions are used to describe one independent atom in the unit cell. The conventional structure refinement methods can determine a finite number of parameters at best, modulation functions are usually described by truncated Fourier series. Large number of parameters cannot be refined due to interdependencies among them. Even some special shaped functions (crenel function and sawtooth function) are used as modulation functions, but the result of structure refinements is still restricted by the choice of parameters for the modulation functions. The result may differ from the true functions and it may not reflect the information content of the diffraction data. The MEM has been proposed as a model-independent tool to obtain the most probable generalized electron density in the unit cell of superspace. Analysis of this superspace electron density

map then provides a model-independent estimate of the modulation functions. This thesis concentrates on the Maximum Entropy Method study of the modulated properties of incommensurate modulated structures. The modulation of the anharmonic ADPs is found to be important, it affects the shape of modulation functions and the fitting of the model to the diffraction data.

The theory of aperiodic crystallography is described in Chapter 2. The basic concept of incommensurate modulated structures, incommensurate composite structures and quasicrystals are given. The idea of superspace together with symmetry options in superspace are introduced.

The concept of entropy is presented in Chapter 3. The principles of the Maximum Entropy Method and its applications in crystallography are described. BAYMEM (van Smaalen et al., 2003) and the Cambridge algorithm (Skilling and Bryan, 1984) are introduced.

Chapter 4 focuses on the problem of extracting integrated intensities of Bragg reflections from area detector data for incommensurately modulated crystals. The X-ray diffraction data integration software EVAL15 is introduced. Integration of X-ray diffraction data measured with CCD detector on beamline F1 (HASYLAB, Hamburg) is described step by step.

Chapter 5 reports on the application of MEM to the X-ray diffraction data of incommensurately modulated rubidium tetrachlorozincate. The MEM study combined with refinement method and difference-Fourier map study have uncovered the modulated properties of both the harmonic and anharmonic atomic displacement parameters of the atoms.

Chapter 6 reports the application of MEM to the X-ray diffraction data of incommensurately modulated Chromium pyrophosphate. The modulation functions, according to atoms-in-molecules theory was presented. A new model was constructed based on the results of the analysis of the MEM density. The modulated structure in the disordered region was studied.

Chapter 2

Aperiodic crystallography and superspace

2.1 Aperiodic crystallography

Crystals are assemblies of atoms which possess long-range translational symmetry. Atoms are arranged according to a lattice in the unit cell, and the structure of the whole crystal can be constructed as a periodic repetition of the unit cell along three linearly independent directions. The position of atom μ with respect to the origin of the unit cell is

$$x^0(\mu) = x_1^0(\mu)\mathbf{a}_1 + x_2^0(\mu)\mathbf{a}_2 + x_3^0(\mu)\mathbf{a}_3, \quad (2.1)$$

$[x_1^0(\mu), x_2^0(\mu), x_3^0(\mu)]$ are relative coordinates with respect to the basis vectors $\{\mathbf{a}_1, \mathbf{a}_2, \mathbf{a}_3\}$. Translational symmetry can be characterized by the lattice $\Lambda = \{\mathbf{a}_1, \mathbf{a}_2, \mathbf{a}_3\}$ with lattice vectors

$$\mathbf{L} = l_1\mathbf{a}_1 + l_2\mathbf{a}_2 + l_3\mathbf{a}_3, \quad (2.2)$$

where $l_i (i = 1, 2, 3)$ are integers.

Aperiodic crystals lack this three-dimensional lattice periodicity, while they are still long-range ordered. The aperiodic crystals can be divided into three main classes (van Smaalen, 2007): modulated structures (Section 2.1.1), incommensurate composite crystals (Section 2.1.2) and quasicrystals (Section 2.1.3).

2.1.1 Incommensurate modulated structures

Incommensurate modulated structures have an average three-dimensionally periodic structure, but the atoms are periodically modulated according to a modulation function with a period that is incommensurate to the periodicity of the basic structure. The real structure is therefore not periodic.

There are mainly three kinds of modulations: a displacive modulation results in the atoms deviated from their basic structure positions, an occupational modulation affects the occupancy of atomic sites by atoms or vacancies, the modulation of ADPs affects the displacement of the atoms about their time-averaged positions. A modulation in the real structures can be a combination of these modulations. Displacements of atoms from the positions in the basic structure towards the positions in the superstructure can have both longitudinal and transversal components (Figure 2.1). Modulation functions are wave functions, they are characterized by a wave vector \mathbf{q} which gives the direction and wavelength of the wave. The components of \mathbf{q} are given with respect to the basis vectors of the reciprocal lattice of the basic structure, $\Lambda^* = \{\mathbf{a}_1^*, \mathbf{a}_2^*, \mathbf{a}_3^*\}$, according to

$$\mathbf{q} = \sigma_1 \mathbf{a}_1^* + \sigma_2 \mathbf{a}_2^* + \sigma_3 \mathbf{a}_3^*. \quad (2.3)$$

Wave functions $\mathbf{u}(\bar{x}_4)$ are periodic functions with

$$\bar{x}_4 = t + \mathbf{q} \cdot \bar{\mathbf{x}}. \quad (2.4)$$

t is the phase of modulation function. $\bar{\mathbf{x}}$ stands for the basic positions of the atoms,

$$\bar{\mathbf{x}} = \bar{x}_1 \mathbf{a}_1 + \bar{x}_2 \mathbf{a}_2 + \bar{x}_3 \mathbf{a}_3, \quad (2.5)$$

where \bar{x}_i is the basic-structure coordinate of atoms along the direction \mathbf{a}_i . The scalar product of vectors \mathbf{q} and $\bar{\mathbf{x}}$ is:

$$\mathbf{q} \cdot \bar{\mathbf{x}} = \sigma_1 \bar{x}_1 + \sigma_2 \bar{x}_2 + \sigma_3 \bar{x}_3. \quad (2.6)$$

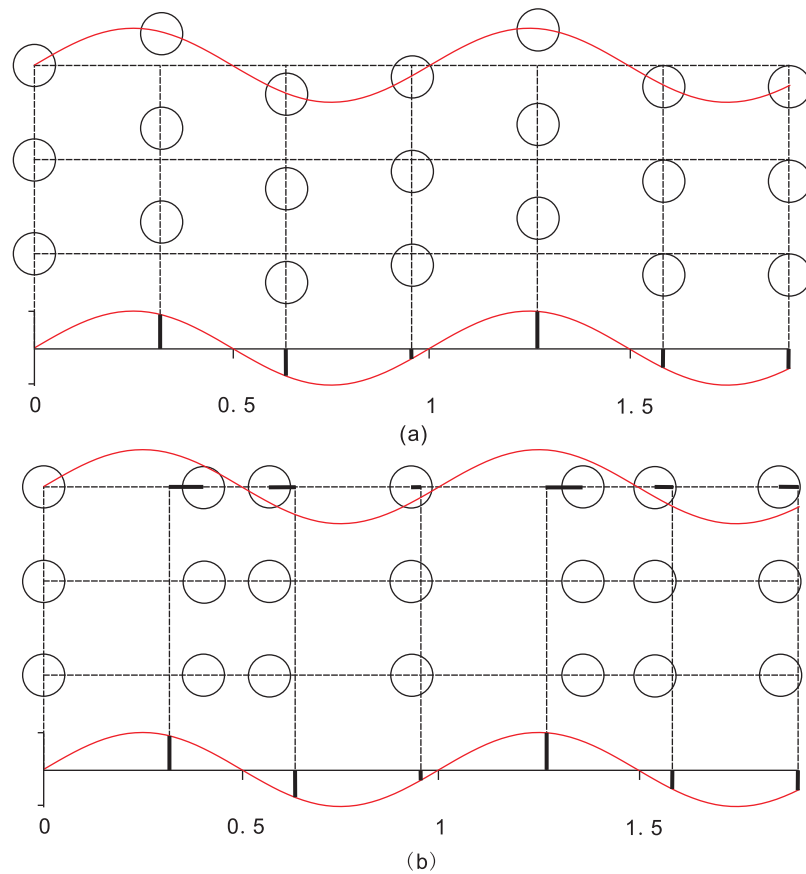


Figure 2.1: Schematic representation of a two-dimensional incommensurate transversal (a) and longitudinal (b) modulated crystal structure, circles are atoms which shift out of lattice periodic positions by varying amounts given by the heavy bars. Numbers count the period of the modulation waves (Equation 2.7).

The modulation functions of atom μ are periodic functions:

$$\mathbf{u}^\mu(\bar{x}_4 + 1) = \mathbf{u}^\mu(\bar{x}_4). \quad (2.7)$$

The displacement of atom μ with the basic position of \bar{x} is

$$\mathbf{u}^\mu(\bar{x}_4) = u_1^\mu(\bar{x}_4)\mathbf{a}_1 + u_2^\mu(\bar{x}_4)\mathbf{a}_2 + u_3^\mu(\bar{x}_4)\mathbf{a}_3. \quad (2.8)$$

The position of atom μ with basic position of $\bar{\mathbf{x}}$ in the crystal is obtained as:

$$\mathbf{x}^\mu = \bar{x}_1\mathbf{a}_1 + \bar{x}_2\mathbf{a}_2 + \bar{x}_3\mathbf{a}_3 + u_1^\mu(\bar{x}_4)\mathbf{a}_1 + u_2^\mu(\bar{x}_4)\mathbf{a}_2 + u_3^\mu(\bar{x}_4)\mathbf{a}_3. \quad (2.9)$$

Any periodic function can be written as a Fourier series:

$$u_i^\mu(\bar{x}_4) = \sum_{n=1}^{\infty} A_i^n(\mu) \sin(2\pi n\bar{x}_4) + B_i^n(\mu) \cos(2\pi n\bar{x}_4). \quad (2.10)$$

$$\mathbf{A}^n(\mu) = [A_x^n(\mu), A_y^n(\mu), A_z^n(\mu)] \quad (2.11)$$

$$\mathbf{B}^n(\mu) = [B_x^n(\mu), B_y^n(\mu), B_z^n(\mu)] \quad (2.12)$$

The Fourier amplitudes $\mathbf{A}^n(\mu)$ and $\mathbf{B}^n(\mu)$ define the modulation functions of atom μ .

2.1.2 Incommensurate composite structures

In general, composite structures are basically combinations of two or more structures. The incommensurate composite crystals are based on two or more interpenetrating periodic structures (named as subsystems), and the basic structures of these subsystems are mutually incommensurate. The interactions between the subsystems affect the periodicity of these subsystems, that make all subsystems modulated. So the incommensurate composite structures can be considered as the intergrowth of two or more incommensurately modulated structures. A parameter has been introduced to describe the periodicity of substructures: $\nu = 1, 2, \dots$ for first, second and further subsystems. The approximate translational symmetry of subsystem ν

is characterized by the lattice:

$$\Lambda_\nu = \{\mathbf{a}_{\nu 1}, \mathbf{a}_{\nu 2}, \mathbf{a}_{\nu 3}\}. \quad (2.13)$$

The modulation wave vector of subsystems ν is

$$\mathbf{q}_\nu = \sigma_{\nu 1} \mathbf{a}_{\nu 1}^* + \sigma_{\nu 2} \mathbf{a}_{\nu 2}^* + \sigma_{\nu 3} \mathbf{a}_{\nu 3}^*, \quad (2.14)$$

the argument of the modulation functions of subsystem ν is given by

$$\bar{x}_{\nu 4} = t_\nu + \mathbf{q}_\nu \cdot \bar{\mathbf{x}} \quad (2.15)$$

(van Smaalen, 2007).

2.1.3 Quasicrystals

Quasicrystals always exhibit a non-crystallographic point-symmetry which is forbidden in periodic structures (Shechtman et al., 1984; Steurer, 2004). Quasicrystals do not have a three-dimensional periodic basic structure, the basic structure is incommensurate. The structures of quasicrystals are described using different approach than is used for the description of the structures of modulated crystals and composite crystals. One dominated difference is that it is not simple to distinguish main and satellites reflections for quasicrystals. Quasicrystals are not discussed in this thesis and the considerations in following sections are related only to the modulated structures and composite structures.

2.2 Superspace

2.2.1 Reciprocal and direct superspace

Because of the three-dimensional long-range order of the atomic arrangement in crystals, the Bragg reflections diffracted by periodic crystals can be indexed by an

integer combination of three independent basis vectors.

$$\mathbf{H} = \sum_{k=1}^3 h_k \mathbf{a}_k^*. \quad (2.16)$$

\mathbf{a}_1^* , \mathbf{a}_2^* , \mathbf{a}_3^* are the reciprocal lattice vectors. The diffraction pattern of aperiodic crystals is not indexable with three integer indices. For example, the diffraction pattern of modulated crystals consists of reflections corresponding to the basic structure (main reflections) and reflections corresponding to the modulation wave (satellites). In the reciprocal space, the satellite reflections located between main reflections, as they are still points in a general three-dimensional space (reciprocal space), they do not need more than three basis vectors for indexing (not integers anymore). These satellite reflections are away from the main reflections which belong to the integer combination of the basis vectors indexing (Equation 2.16), so the satellite reflections can only be indexed with non-integer combination of the basis vectors. With this method, all reflections can be indexed by $(3 + d)$ ($d \geq 1$) vectors with 3 basic vectors for main reflections and d additional vectors for satellite reflections. The first three vectors are linearly independent and the additional vectors can be expressed as:

$$\mathbf{a}_{3+j}^* = \sum_{i=1}^3 \sigma_{ji} \mathbf{a}_i^*, \quad j = 1, \dots, d. \quad (2.17)$$

The diffraction vector \mathbf{H} of each reflection can be indexed by $(3 + d)$ integers:

$$\mathbf{H} = \sum_{k=1}^{3+d} h_k \mathbf{a}_k^*. \quad (2.18)$$

Take one-dimensional modulated structures as example, four ($= 3 + 1$) integers have to be used to index the reflections:

$$\mathbf{H} = h_1 \mathbf{a}_1^* + h_2 \mathbf{a}_2^* + h_3 \mathbf{a}_3^* + h_4 \mathbf{a}_4^*. \quad (2.19)$$

The first three basis vectors define a reciprocal lattice,

$$\Lambda^* = \{\mathbf{a}_1^*, \mathbf{a}_2^*, \mathbf{a}_3^*\}, \quad (2.20)$$

the fourth basis vector can be expressed as:

$$\mathbf{a}_4^* = \sigma_1 \mathbf{a}_1^* + \sigma_2 \mathbf{a}_2^* + \sigma_3 \mathbf{a}_3^*. \quad (2.21)$$

This is actually the definition of \mathbf{q} vector (Equation 2.3). Because at least one of σ_i ($i = 1, 2, 3$) is irrational, so the set

$$\Lambda_4^* = \{\mathbf{a}_1^*, \mathbf{a}_2^*, \mathbf{a}_3^*, \mathbf{a}_4^*\} \quad (2.22)$$

is rationally independent and the indices (h_1, h_2, h_3, h_4) are unique. Then Equation 2.19 can be transformed to

$$\mathbf{H} = (h_1 + \sigma_1 h_4) \mathbf{a}_1^* + (h_2 + \sigma_2 h_4) \mathbf{a}_2^* + (h_3 + \sigma_3 h_4) \mathbf{a}_3^*. \quad (2.23)$$

This confirms that satellite reflections are located between the main reflections in reciprocal space. Customarily, the three-dimensional space is called external space and the (+1)-dimension is named to internal space (van Smaalen, 2007).

The idea of superspace is describing aperiodic functions as periodic functions in an abstract space with $(3 + 1)$ dimensions. The four reciprocal vectors $(\mathbf{a}_1^*, \mathbf{a}_2^*, \mathbf{a}_3^*, \mathbf{q})$ in three dimensional space are considered to be the projection of four reciprocal basis vectors in $(3+1)$ dimensional space. So a reflection indexed with (h_1, h_2, h_3, h_4) can be identified with the reciprocal lattice point in $(3 + 1)$ dimensional space by the same indices:

$$\mathbf{H}_s = h_1 \mathbf{a}_{s1}^* + h_2 \mathbf{a}_{s2}^* + h_3 \mathbf{a}_{s3}^* + h_4 \mathbf{a}_{s4}^*. \quad (2.24)$$

The reciprocal lattice in superspace is defined by (van Smaalen, 2007):

$$\Sigma^* : \begin{cases} \mathbf{a}_{si}^* = (\mathbf{a}_i^*, 0) & i = 1, 2, 3 \\ \mathbf{a}_{s4}^* = (\mathbf{a}_4^*, \mathbf{b}^*). \end{cases} \quad (2.25)$$

The vector \mathbf{b}^* is perpendicular to real space, it has no physical meaning, the length is arbitrary and here is set to one. The direct superspace lattice corresponding to the reciprocal lattice Σ^* is (van Smaalen, 2007):

$$\Sigma : \begin{cases} \mathbf{a}_{si} = (\mathbf{a}_i, -\sigma_i \mathbf{b}) & i = 1, 2, 3 \\ \mathbf{a}_{s4} = (0, \mathbf{b}). \end{cases} \quad (2.26)$$

Vectors in direct superspace with coordinates relative to Σ are defined by :

$$\mathbf{x}_s = x_{s1} \mathbf{a}_{s1} + x_{s2} \mathbf{a}_{s2} + x_{s3} \mathbf{a}_{s3} + x_{s4} \mathbf{a}_{s4}. \quad (2.27)$$

2.2.2 Symmetry in superspace

General position vector

In three-dimensional space, the position vector \mathbf{r} of a point is defined as the sum of the products of the fractional coordinates of this point with the respective lattice vectors:

$$\mathbf{r} = x\mathbf{a}_1 + y\mathbf{a}_2 + z\mathbf{a}_3. \quad (2.28)$$

In superspace the rule does not change, for simplification reason, in (3+1)-dimensional superspace a general point can be written as:

$$\mathbf{r}_s = (\mathbf{r}, \mathbf{r}_I) = x\mathbf{a}_{s1} + y\mathbf{a}_{s2} + z\mathbf{a}_{s3} + x_4\mathbf{a}_{s4}. \quad (2.29)$$

With the definition of direct superspace lattice in Equation 2.26, we get:

$$\begin{aligned} \mathbf{r}_s &= x(\mathbf{a}_1, -\sigma_1 \mathbf{b}) + y(\mathbf{a}_2, -\sigma_2 \mathbf{b}) + z(\mathbf{a}_3, -\sigma_3 \mathbf{b}) + x_4(0, \mathbf{b}) \\ &= (x\mathbf{a}_1 + y\mathbf{a}_2 + z\mathbf{a}_3) + x_4 \mathbf{b} - (x\sigma_1 + y\sigma_2 + z\sigma_3) \mathbf{b}, \end{aligned} \quad (2.30)$$

it is easy to get:

$$(x\sigma_1 + y\sigma_2 + z\sigma_3) = (\sigma_1 \mathbf{a}_1^* + \sigma_2 \mathbf{a}_2^* + \sigma_3 \mathbf{a}_3^*) \cdot (x\mathbf{a}_1 + y\mathbf{a}_2 + z\mathbf{a}_3) \quad (2.31)$$

according to Equation 2.28 and Equation 2.3, the general point position can be derived as:

$$\mathbf{r}_s = \mathbf{r} + [x_4 - \mathbf{q} \cdot \mathbf{r}^0] \mathbf{b}, \quad (2.32)$$

\mathbf{b} is the unit vector along \mathbf{a}_{s4} . Comparing to Equation 2.29, \mathbf{r}_I can be derived as:

$$\begin{aligned} \mathbf{r}_I &= [x_4 - \mathbf{q} \cdot \mathbf{r}^0] \mathbf{b} \\ r_I &= x_4 - \mathbf{q} \cdot \mathbf{r}^0 \end{aligned} \quad (2.33)$$

which indicates the internal part of the position vector r_I is identical with the phase of the modulation t :

$$r_I = t = x_4 - \mathbf{q} \cdot \mathbf{r}^0. \quad (2.34)$$

General symmetry operation

In three-dimensional space groups, a general symmetry element is defined as

$$g = \{R \mid \mathbf{v}\}, \quad (2.35)$$

where R is the rotational part of the symmetry element while \mathbf{v} is the translational part of the symmetry element. Applying this symmetry to a general point described by \mathbf{r} gives:

$$\mathbf{r}' = g\mathbf{r} = R\mathbf{r} + \mathbf{v}. \quad (2.36)$$

General symmetry element in superspace groups can be defined in the same way, in $(3 + 1)$ -dimensional superspace it is:

$$\begin{aligned} g_s &= \{R_s \mid \mathbf{v}_s\} \\ &= \{R, R_I \mid \mathbf{v}, \mathbf{v}_I\}. \end{aligned} \quad (2.37)$$

In $(3 + 1)$ -dimensional superspace, R_I and \mathbf{v}_I are written as ε and Δ respectively:

$$\begin{aligned} g_s &= \{R, \varepsilon \mid \mathbf{v}, \Delta\} \\ &= \{R \mid \mathbf{v}\} \{\varepsilon \mid \Delta\}. \end{aligned} \quad (2.38)$$

In this way, a general symmetry operation in $(3 + 1)$ -dimensional superspace was separated into two parts, a general symmetry operation in external space and a symmetry operation in the internal space. Δ is the translation operation in the internal space, for the $(3+1)$ -dimensional superspace, it becomes the phase shift operation. ε is the internal transformation which correspond to rotation operation in three dimensional symmetry operation. It is assigned to the values $\varepsilon = \pm 1$, and if $\varepsilon = -1$, a phase inversion of the modulation functions is performed. The ε element is fixed by the relation

$$R\mathbf{q} = \varepsilon\mathbf{q}. \quad (2.39)$$

Applying a superspace operation Equation 2.38 to a general vector \mathbf{r}_s gives:

$$\begin{aligned} \mathbf{r}'_s &= g_s \mathbf{r}_s \\ &= \{R \mid \mathbf{v}\} \{\varepsilon \mid \Delta\}(\mathbf{r}, t) \\ &= \{R\mathbf{r} + \mathbf{v}\} \{\varepsilon t + \Delta\}. \end{aligned} \quad (2.40)$$

$\mathbf{v} = \Delta$ is a translational operation in the internal space, and of course it is a vector of internal space. The general equation of vectors in internal space (Equation 2.34) can be applied:

$$\mathbf{v}_I = x_4 - \mathbf{q} \cdot \mathbf{v}. \quad (2.41)$$

2.3 Modulation functions

Various properties of atoms, like position, site, ADPs (both harmonic and anharmonic) can be modulated. Usually combinations of several properties can be modulated. Modulation functions can be either continuous or discontinuous functions, like block waves and linear functions. Use of harmonic functions to describe discontinuous modulation is possible but require a large number of harmonics to achieve the proper shape of the modulation function. So several special functions have been introduced to describe modulation functions in a simple way, for example: crenel function and sawtooth function.

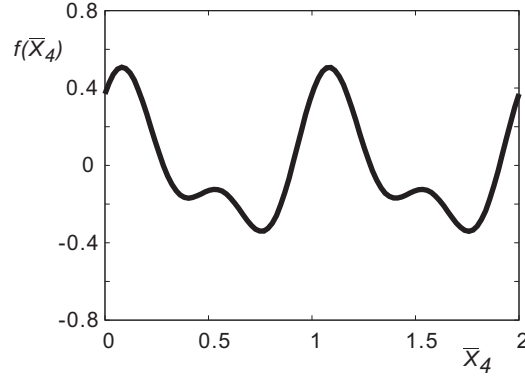


Figure 2.2: An anharmonic function following the definition in Equation 2.42 with $A_1 = 0.25$, $B_1 = 0.22$, $A_2 = 0.12$ and $B_2 = 0.14$.

2.3.1 Different types of modulation functions

Harmonic and anharmonic functions

A Fourier series is defined as

$$f(\bar{x}_4) = x_i^0 + A_1 \cdot \cos(2\pi \cdot 1\bar{x}_4) + B_1 \cdot \sin(2\pi \cdot 1\bar{x}_4) + A_2 \cdot \cos(2\pi \cdot 2\bar{x}_4) + B_2 \cdot \sin(2\pi \cdot 2\bar{x}_4) + \dots \quad (2.42)$$

Normally, the modulation function formed by only one *sine* or *cosine* function is called harmonic function, otherwise, it is named as anharmonic function. In Figure. 2.2, an example anharmonic function is drawn.

Crenel function

Very often modeling the proper shape of the occupational modulation function requires a large number of harmonics. In these cases more efficient way is to use crenel function defined as:

$$\begin{aligned} f(\bar{x}_4) &= 1 & \bar{x}_4 &\in [\bar{x}_4^0 - \Delta/2, \bar{x}_4^0 + \Delta/2] \\ f(\bar{x}_4) &= 0 & \bar{x}_4 &\notin [\bar{x}_4^0 - \Delta/2, \bar{x}_4^0 + \Delta/2] \end{aligned} \quad (2.43)$$

while x_4^0 is the center and Δ is the width. In Figure. 2.3, an example crenel function is drawn.

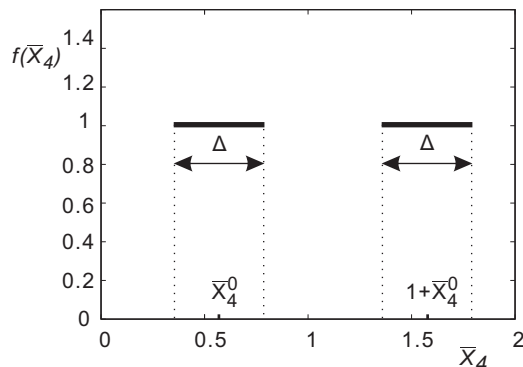


Figure 2.3: An crenel function with width $\Delta = 0.43$ and center $\bar{x}_4^0 = 0.57$.

Sawtooth function

The sawtooth function is defined by its width Δ , center \bar{x}_4^0 and the slope. In Figure. 2.4, an example sawtooth function is drawn.

2.3.2 Modulation functions used in the present thesis

In this thesis, the modulated properties of the harmonic ADPs and anharmonic ADPs (Chapter 5), and also the modulated structure with combination of modulated positions, modulated occupancies and modulated anharmonic ADPs in the disorder region (Chapter 6) are studied for Rb_2ZnCl_4 and $\text{Cr}_2\text{P}_2\text{O}_7$ respectively. In Section 5.3.1, crenel function has been used to describe the occupation of all atoms except atom O1. Furthermore, harmonic function has been used to describe the occupational modulation of atoms P(a) and P(b). Anharmonic functions have been used to describe displacement modulation functions of all atoms, the modulation of atomic displacement parameters (ADPs) of all atoms and the third-order anharmonic ADPs of atoms P (Section 5.3.2), Rb1, Rb2 and Cl3 (Section 6.4.1).

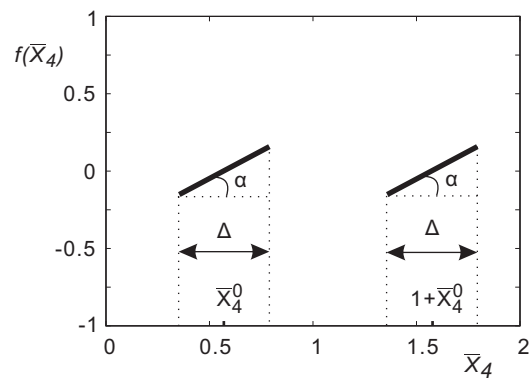


Figure 2.4: A sawtooth function defined with width $\Delta = 0.43$, center $\bar{x}_4^0 = 0.57$ and the slope = 0.5.

Chapter 3

The Maximum Entropy Method in crystallography

3.1 Applications of the MEM

Entropy is a concept used in thermodynamics to describe the state of order of a system, and entropy is used as a measure of the amount of information in a message: higher entropy less information. The Maximum Entropy Method is a general method for data analysis, which is employed to extract the maximum amount of information from the data, without the introduction of artifacts or assumptions concerning a model (Jaynes, 1957).

In X-ray diffraction studies, MEM helps to determine the most probable electron density distribution in the unit cell allowed by the data (Sakata and Sato, 1990; Gilmore, 1996). The analysis of the reconstructed electron density in the unit cell can provide information about disorder (Dinnebier et al., 1999; Wang et al., 2001), anharmonic thermal motion (Kumazawa et al., 1995; Bagautdinov et al., 1998), and chemical bonding (Sakata and Sato, 1990; Takata, 2008; van Smaalen and Netzels, 2009). In superspace, MEM has already been implemented to determine the most probable electron density distribution in $(3+d)$ -dimensional space (van Smaalen et al., 2003; van Smaalen, 2007). The shapes of the modulation functions of modulated crystals have been determined by the analysis of the reconstructed electron density

in $(3+d)$ -dimensional space (Palatinus and van Smaalen, 2004; van Smaalen and Li, 2009). In this thesis, MEM together with refinement methods have been used to study the modulated properties of the harmonic ADPs and anharmonic ADPs in Chapter 5, and also the modulated structure which combined of modulated positions, modulated occupancies and modulated anharmonic ADPs in the disorder region in Chapter 6. In addition, the MEM can also be used for deconvolution of powder diffraction data (Gilmore, 1996), and to extract phases from intensities of Bragg reflections (Bricogne, 1988), which are not going to be discussed in this thesis.

3.2 Principle of the MEM - BayMEM

The case of the X-ray diffraction will be considered here, even though the principle of the MEM can be applied in many fields of science. The generalized electron density $\rho_s(\mathbf{x}_s)$ in n -dimensional superspace is discretized on a grid of $N_p = N_1 \times N_2 \times \dots \times N_n$ pixels over the whole unit cell. $n = 3$ or $n > 3$ are used for periodic structures or superspace electron density distribution respectively. N_i is the number of pixels along dimension i . The grid is required to obey the symmetry of the crystal. This symmetry restriction has important consequence on the choice of the grid of the discrete density. Each grid point must be transformed onto itself or onto another grid point by all possible symmetry operators which implies that the space around each grid point must have the shape of the Wigner-Seitz unit cell of the lattice (Schneider and van Smaalen, 2000).

The entropy is defined as (van Smaalen et al., 2003):

$$S = - \sum_{k=1}^{N_{pix}} (\rho_k \ln[\rho_k/\rho_k^{prior}] - \rho_k + \rho_k^{prior}), \quad (3.1)$$

where $\rho_k = \rho_s(\mathbf{x}_{sk})$ is the electron density at the k^{th} grid point and ρ_k^{prior} is the corresponding value of the reference density or PRIOR. The MEM defines the optimal electron density as the electron density $\{\rho_k\}$ which maximizes the entropy S (Equation 3.1) subject to several constraints. (In the absence of constraints, the solution is $\rho_k = \rho_k^{prior}$, the reconstructed electron density is as same as the reference

density.) The normalization of $\{\rho_k\}$ is the first constraint which is named as C_N constraint (van Smaalen, 2007):

$$C_N = \frac{V}{N_{pix}} \sum_{k=1}^{N_{pix}} \rho_k - N_e \quad (3.2)$$

where N_e is the number of electrons in the unit cell and V is its volume. Diffraction data are incorporated in the form of the so-called F -constraint, C_F , with (Sakata and Sato, 1990)

$$C_F = -1 + \frac{1}{N_F} \sum_{i=1}^{N_F} w_i \left(\frac{|F_{obs}(\mathbf{H}_i) - F_{MEM}(\mathbf{H}_i)|}{\sigma_i} \right)^2. \quad (3.3)$$

The sum runs over all independent structure factors N_F in the data set. $F_{obs}(\mathbf{H}_i)$ is the phased observed structure factor of the reflection with scattering vector \mathbf{H}_i , and σ_i is the standard uncertainty of $|F_{obs}(\mathbf{H}_i)|$. $F_{MEM}(\mathbf{H}_i)$ is obtained by n -dimensional Fourier transform of the trial density $\{\rho_k\}$. The standard version of the MEM employs weights $w_i = 1$. The F -constraint then represents χ^2 of the data with an expectation value of one. in the present thesis, different weighting method has been used for all calculations, details are described in Section 6.3.

To determine the most probable density, the problem of the maximum of the entropy has to be solved. The method of Lagrange multipliers (named after Joseph Louis Lagrange) provides a strategy for finding the maximum of the entropy subject to all these constraints. The maximum of the Lagrangian

$$Q(\rho_k) = S(\rho_k) - \lambda_N C_N(\rho_k) - \lambda_F C_F(\rho_k) \quad (3.4)$$

has to be determined for variations of λ_N , λ_F and $\{\rho_k\}$. λ_N and λ_F are Lagrange multipliers, C_N is the normalization constraint (Equation 3.2) and C_F is the diffraction-data constraint (Equation 3.3). The maximum of Q respect to λ_n ($n = 0, 1, \dots$) results in C_N and C_F equal to zero. The constraints (Equation 3.2 and Equation

3.3) are take into account of the maximum procedure by :

$$\begin{cases} C_N = \frac{V}{N_{pix}} \sum_{k=1}^{N_{pix}} \rho_k - N_e = 0 \\ C_F = -1 + \frac{1}{N_F} \sum_{i=1}^{N_F} w_i \left(\frac{|E_{obs}(\mathbf{H}_i) - F_{MEM}(\mathbf{H}_i)|}{\sigma_i} \right)^2 = 0. \end{cases} \quad (3.5)$$

The maximum of Q respect to ρ_k is defined by $\partial Q / \partial \rho_k = 0$. Differentiating equation 3.4 with respect to ρ_k gives:

$$\frac{\partial Q}{\partial \rho_k} = \frac{\partial S}{\partial \rho_k} - \lambda_N \frac{\partial C_N}{\partial \rho_k} - \lambda_F \frac{\partial C_F}{\partial \rho_k}, \quad (3.6)$$

using the definition of entropy (Equation 3.1) we get:

$$\frac{\partial S(\rho_k)}{\partial \rho_k} = -\ln[\rho_k / \rho_k^{prior}], \quad (3.7)$$

considering for constraints C_N and C_F (Equation 3.2 and Equation 3.3):

$$-\ln[\rho_k / \rho_k^{prior}] = \lambda_N \frac{\partial C_N}{\partial \rho_k} + \lambda_F \frac{\partial C_F}{\partial \rho_k}. \quad (3.8)$$

Take the normalization constraint $C_N = 0$ into account, after the elimination of the Lagrange multiplier λ_N , the form of the normalized electron density is:

$$\rho_k = \rho_k^{prior} \exp \left[-\lambda_F \frac{\partial C_F}{\partial \rho_k} \right] / \sum_{j=1}^{N_{pix}} \rho_j^{prior} \exp \left[-\lambda_F \frac{\partial C_F}{\partial \rho_j} \right], \quad (3.9)$$

for simplicity,

$$Z(\lambda_F) = \sum_{j=1}^{N_{pix}} \rho_j^{prior} \exp \left[-\lambda_F \frac{\partial C_F}{\partial \rho_j} \right] \quad (3.10)$$

was introduced, the final electron density form is

$$\rho_k = \frac{1}{Z(\lambda_F)} \rho_k^{prior} \exp \left[-\lambda_F \frac{\partial C_F}{\partial \rho_k} \right]. \quad (3.11)$$

Equation 3.13 together with Equation 3.3 give a set of $N_{pix} + 1$ nonlinear equa-

tions which cannot be solved analytically. Several algorithms (Skilling and Bryan, 1984; Sakata and Sato, 1990; Kumazawa et al., 1995) have been suggested to solve the problem iteratively. In the computer program BAYMEM (van Smaalen et al., 2003), the Cambridge algorithm (Skilling and Bryan, 1984) [via the MemSys5 package (Gull and Skilling, 1999)] and the Sakato-Sato algorithm (Sakata and Sato, 1990; Kumazawa et al., 1995) are included to determine the values $\{\rho_k^{MEM}\}$ of the density $\rho^{MEM}(\mathbf{x})$ optimized by the MEM. The Cambridge algorithm optimizes the λ_F and ρ_k simultaneously. It starts with a small λ_F ($\lambda_F^{(0)}$) value, a density $\rho_k^{(0)}$ equals to ρ_k^{prior} and an equation of the iterates of density defined as

$$\rho_k^{(n+1)} = \frac{1}{Z(\lambda_F^{(0)})} \rho_k^{prior} \exp \left[-\lambda_F \frac{\partial C_F^{(n)}}{\partial \rho_k} \right]. \quad (3.12)$$

When $\rho_k^{(n+1)}$ is sufficiently close to $\rho_k^{(n)}$, the iteration converged and will repeated with a higher value of λ_F ($\lambda_F^{(1)}$). The iteration is considered to be converged if the constraint equation $C_F = 0$ is fulfilled. The Sakato-Sato algorithm uses a fixed, sufficiently small value of λ_F and optimizes the $\rho^{MEM}(\mathbf{x})$. Additionally, the iteration derived values $\rho_k^{(n)}$ are used as PRIOR density for the next iteration step:

$$\rho_k^{(n+1)} = \frac{1}{Z(\lambda_F)} \rho_k^{(n)} \exp \left[-\lambda_F \frac{\partial C_F^{(n)}}{\partial \rho_k} \right]. \quad (3.13)$$

A detailed comparison of both algorithms with the computer program BAYMEM (van Smaalen et al., 2003) shows that the Cambridge algorithm converges faster and more reliably than the Sakato-Sato algorithm, and the differences between the two algorithms derived ρ^{MEM} are less than the noise in the resulting density (van Smaalen et al., 2003). Thus, the MEM calculations of the present work have been performed with the computer program BAYMEM (van Smaalen et al., 2003) and the Cambridge algorithm (Section 5.3.3 and Section 6.4.2).

Chapter 4

Integration of aperiodic crystals diffraction data

4.1 The EVAL15 method

EVAL15 is a diffraction data integration method based on *ab initio* calculation of the three-dimensional reflection profiles from several parameters of the crystal and the instruments. With the software package EVAL15, complete three-dimensional reflection profiles are calculated from different impacts such as crystal size and shape, beam focus dimension and divergence, wavelength dispersion, experimental geometry, detector point spread and mosaicity of crystal. Description of the method in detail can be found in Schreurs et al. (2010).

4.2 Integrating of diffraction data of aperiodic crystals

The diffraction pattern of aperiodic crystals is not indexable with three integer indices, as discussed in Section 2.2. For the incommensurately modulated structures, $(3 + d)$ ($d \leq 3$) vectors have been used for the indexing of all reflections (Equation 2.18). The normal integration software uses three vectors for the reflection indexing, they are not suitable for the integration of satellite reflections.

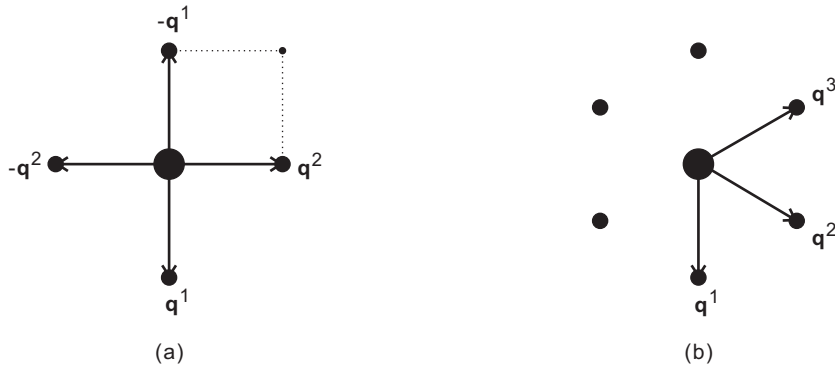


Figure 4.1: Schematic diffraction pattern of two-dimensional modulated orthorhombic structure (a) and two-dimensional modulated hexagonal structure (b). Large, and small discs represent main reflections, and first-order satellite reflections respectively.

CrysAlis (Oxford-Diffraction, 2006) is one option for integration of satellite reflections, but it cannot handle data from diffractometers other than Oxford-Diffraction instruments. Furthermore, the order of satellite reflections is defined depend on the crystal systems. For the triclinic, monoclinic and orthorhombic crystal systems, the order of the satellite reflections is defined as the sum of the absolute values of the satellite indices. For examples: The order of a satellite reflection (h, k, l, m) from diffraction of an one-dimensional modulated monoclinic structure is defined as $|m|$. The order of a satellite reflection (h, k, l, m_1, m_2) from diffraction of a two-dimensional modulated orthorhombic structure is defined as $|m_1| + |m_2|$. If the angle between these two modulation wave vectors change from 90° to 60° , like the case of diffraction of a two-dimensional modulated hexagonal structure, the combination of $-\mathbf{q}^1 + \mathbf{q}^2$ generates the third but equivalent modulation wave vector \mathbf{q}^3 instead of a wave vector of a second order satellite reflection (Figure 4.1). The order of these satellite reflections is then defined as (van Smaalen, 2007):

$$\frac{1}{2}(|m_1| + |m_2| + |m_1 + m_2|). \quad (4.1)$$

Integration of satellite reflections was incorporated into EVAL15 by Schreurs et al. (2010) in collaboration with us (Laboratory of Crystallography, University Bayreuth, Germany). A **QVC** (**q**-vector) is defined in the orientation matrix file. With different combinations of **QVC**, users can freely choose the integration of satellite

reflections with certain orders.

4.3 Case study: data integration of Rb_2ZnCl_4 by EVAL15

X-ray diffraction experiment of Rb_2ZnCl_4 was performed on beamline F1 Hasylab (DESY, Germany) with CCD detector, details are described in Section 5.3. In this chapter, the integration of one run of data by EVAL15 is detailed. The bad pixel problem during the integration and its solution are presented.

The measured frames are saved on the central data server of the laboratory, `btakr1.kri.uni-bayreuth.de`. The IP-address is `132.180.126.46`. Parameter of this data is give in Table 4.1. The EVAL15 software is installed on the Linux computer

Table 4.1: Experimental details of the X-ray diffraction data.

$2\theta(^{\circ})$	$\omega(^{\circ})$	$\chi(^{\circ})$	$\phi(^{\circ})$	Time (Sec.)	$\Delta\phi(^{\circ})$	Frames	Name	New name
-31	0	0	$37.3 \sim 142.3$	64	0.3	350	rbzncl_4b	s04

`btakxc.kri.uni-bayreuth.de`, the IP-address is `132.180.126.49`.

- Create softlinks to the images on `btakr1.kri.uni-bayreuth.de`:
`~/rbzbcl> ln -s /home/btak07/dsk2/ hasyF1.0710_rbzncl/rbzncl_4b/*` .
- Rename the frames to systematic names:
`~/rbzncl> renameimages`
 The new file type is `mccd`, the scan name `rbzncl_4b` is renamed to `s04`. The log file `renameimages.log` will be created.
- Copy the files `goniostat.vic` and `view.init` to the experiment directory:
`~/rbzbcl> cp /usr/local/utrecht_mark/initdoc/initdoc_F1/*` .
 In `goniostat.vic`, information about the goniostat is given, like goniostat type and rotation direction of axis. `view.init` defines how the software read in the frames. In case of missing header information, new header information can be specified in this file also.

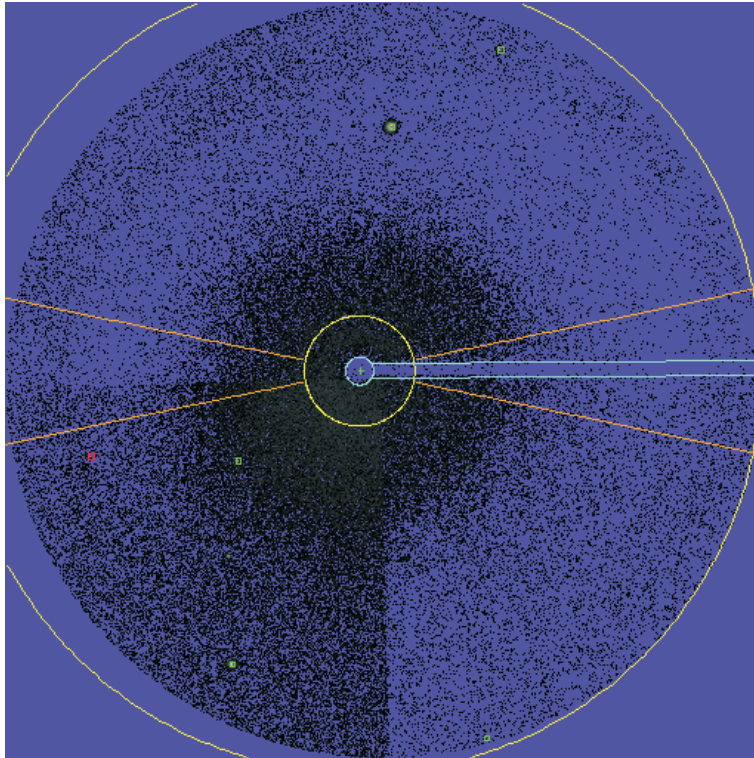


Figure 4.2: The frame s02f0001 plotted with VIEW.

- Check the data:

```
~/rbzncl> scancheck
```

The averaged background, the duration of each frames are checked. Substract AdcZero off is selected for frame measured at beamline F1. This will generate the file scanchecks04f.log .

- Create the low image:

```
~/rbzncl> low3
```

This will generate the files s04flow.mccd and s04fhome.mccd . The minimum value of each pixel during the experiment and its location are restored in s04flow.mccd and s04fhome.mccd respectively.

To find out the beamstop position and the primary beam position, one frame without 2θ offset is copied to the current directory and renamed to s02f0001.

- Launch the program:

Table 4.2: The displayed parameters for frame s04f0001.

	Dist	Swing	Omega	Chi	Phi	Axis	Start	End
old	0.00	0.00	0.00	0.00	0.00	1		
new	225.00	-31.00	0.00	0.00	0.00	3	1.00	1.30

Table 4.3: DIRAX result, Acl is the number of the solution, and H is the number of vector fitting to the solution. Parameters of the unit cell: a, b, c, alpha, beta, gamma and volume are given.

Acl	H	a	b	c	alpha	beta	gamma	Volume
572	78	9.217	14.434	50.780	89.51	88.67	89.81	6754
541	81	7.249	9.235	12.520	89.78	89.75	89.76	838
488	74	7.223	9.189	12.489	90.59	90.09	90.38	829
443	69	7.173	9.225	12.502	90.37	90.20	90.50	827
399	98	9.179	7.199	12.500	89.98	90.50	90.05	826
308	133	7.222	9.177	12.507	90.46	90.16	90.17	829
305	123	7.222	9.173	12.508	90.47	90.16	90.18	829
302	114	7.213	9.250	12.498	90.47	89.98	90.20	834
283	61	3.611	9.239	12.515	90.19	90.19	89.95	417
272	88	7.196	9.209	12.479	90.77	90.16	90.30	827
249	78	7.208	9.164	12.434	91.36	90.32	90.44	821
216	43	7.209	9.162	12.384	91.89	90.42	90.34	817
211	115	9.149	7.212	12.479	89.99	90.86	90.09	823
199	58	7.196	9.213	12.402	91.70	90.61	91.12	822
151	42	7.242	9.241	12.380	91.71	90.26	90.36	828
145	109	7.227	9.264	12.511	90.11	89.97	90.36	838
130	123	7.221	9.227	12.511	90.22	90.11	90.03	834
115	126	9.194	7.217	12.498	90.04	90.48	90.04	829
111	88	7.228	9.195	12.529	90.17	90.32	90.27	833
92	113	9.152	7.213	12.478	90.03	90.85	89.96	824
84	78	7.234	9.143	12.536	90.35	90.42	90.54	829
51	5	1.099	1.557	9.043	88.50	87.90	77.61	15
30	3	2.174	2.732	4.924	73.96	79.25	88.92	28

```
~/rbzncl> view
```

- Read-in one frame without 2θ offset:

```
View> read s02f0001
```

- Plot this frame to screen:

```
View> plot
```

- Display the position of the primary beam:

```
View> markprimary
```

A blue cross will appear at the (theoretical) primary beam position.

- Correct the detector position:

```
View> detectorshift dist hor ver
```

A positive number for *hor* shifts the detector to the right, a negative one to the left, a positive number for *ver* shifts it to the top, a negative one to the bottom.

Save the final setting into the file `detalign.vic` :

```
View> save detalign
```

- Display the beamstop:

```
View> drawbeamstop
```

With the command `beamstopangle` one corrects the orientation, with `beamstopwidth` and `beamstopdiameter` the dimensions. Save the final setting into the file `beamstop.vic` :

```
View> save beamstop
```

- Search for peaks in the present frame:

```
View> peak2
```

(Figure 4.2)

- Quit the program VIEW :

```
View> exit
```

- Launch the program VIEW again:
`~/rbzncl> view`
- Read-in one frame with 2θ offset:
`View> read s04f0001`
Check the displayed parameters (Table 4.2).
- Quit the program VIEW:
`View> exit`
- Build a script for peak search:
`~/rbzncl> buildsearch`
Prefix name: *a* , the parameters are saved in the file *asearch.vic* . Select search type 3, which means, that a continuous set of frames will be analysed. Search five peaks per frame.
- Start program VIEW:
`~/rbzncl> view`
- Read-in one frame:
`View> read s04f0001`
- Do the peak search:
`View> @asearch`
The software start to look for five peaks on each frames, and the found peaks are used to calculate the unit cell parameters.
- Quit the program VIEW:
`View> exit`
The results of the peak search are written into the files *a1.pk* and *a1.drx* .

4.3.1 Indexing of reflections

The indexing is done with the program DIRAX .

- Launch the DIRAX program:
`~/rbzncl> dirax`

- Read-in the `.drx` file:
Dirax> read *a1.drx*
- Start the indexing:
Dirax> go
The index result is given in Table 4.3.
- Chose the solution:
Dirax> acl *308*
The solution of number 308 with 133 fitted vectors is selected.
- Save the found orientation matrix:
Dirax> ccd *a*
The matrix is saved to the file *a.rmat* , this is the initial orientation matrix, the accuracy will be improved with the following steps.
- Quit the indexing program DIRAX :
Dirax> exit

4.3.2 Refinement

In the next step one has to refine the lattice, detector, and goniometer parameters with the program `PEAKREF` .

- Launch the program:
~/rbznc1> peakref
- First read-in the orientation matrix:
Peakref> rmat *a*
- Then read in the peak list:
Peakref> pk *a1.pk*
- Check the current parameters:
Peakref> status
The status is shown in Table 4.4.

Table 4.4: Status of parameters at the beginning of PEAKREF, 655 of 960 reflections are used for the refinement.

	ref	current	previous	change	initial	change	shift
a	No	7.22198			7.22198		0.03611
b	No	9.17671			9.17671		0.04588
c	No	12.50730			12.50730		0.06254
alpha	No	90.46388			90.46388		1.00000
beta	No	90.16324			90.16324		1.00000
gamma	No	90.17368			90.17368		1.00000
orx	No	0.85030			0.85030		0.00203
ory	No	-0.48556			-0.48556		0.00203
ora	No	-145.42537			-145.42537		1.00000
zerodist	No	0.00000			0.00000		0.10000
zerohor	Yes	0.00000	0.00000	0.00000	0.00000	0.00000	0.10000
zerover	Yes	0.00000	0.00000	0.00000	0.00000	0.00000	0.10000
xtalx	No	0.00000			0.00000		0.10000
xtaly	No	0.00000			0.00000		0.10000
xtalz	Fix	0.00000			0.00000		0.10000
Vol		828.87	828.87	0.00	828.87	0.00	655
mm		0.38030	0.38030	0.00000	0.38030	0.00000	655
mmAng	+	0.09684	0.09684	0.00000	0.09684	0.00000	655
rotpartial	+	0.00000	0.00000	0.00000	0.00000	0.00000	0
rotoutside		0.04289	0.04289	0.00000	0.04289	0.00000	123
rotinside		0.00000	0.00000	0.00000	0.00000	0.00000	532
rotall		0.00805	0.00805	0.00000	0.00805	0.00000	655
res		0.09684	0.09684	0.00000	0.09684	0.00000	

- Start refinement:

```
Peakref> go3
```

- Give the parameters of orientation matrix free and redo the refinement:

```
Peakref> free rmat
```

```
Peakref> go3
```

- Control the symmetry by modifying the point group tolerance:

```
Peakref> pgzero 0.1 1
```

0.1 is the tolerance (mm) for the axis lengths (compared to each other) and

Table 4.5: Status after refining all the parameters. 679 of 960 reflections are used in the refinement (Part 1).

	ref	current	previous	change	initial	change	shift
a	Yes	7.20677	7.20716	-0.00039	7.22198	-0.01521	0.03611
b	Yes	9.15398	9.15460	-0.00062	9.17671	-0.02273	0.04588
c	Yes	12.56825	12.56840	-0.00014	12.50730	0.06095	0.06254
alpha	Fix	90.00000			90.46388		1.00000
beta	Fix	90.00000			90.16324		1.00000
gamma	Fix	90.00000			90.17368		1.00000
orx	Yes	0.84865	0.84871	-0.00006	0.85030	-0.00165	0.00203
ory	Yes	-0.48862	-0.48847	-0.00015	-0.48556	-0.00306	0.00203
ora	Yes	-145.24277	-145.22879	-0.01397	-145.42537	0.18261	1.00000
zerodist	Yes	0.62243	0.63462	-0.01219	0.00000	0.62243	0.10000
zerohor	Yes	-0.37664	-0.38867	0.01203	0.00000	-0.37664	0.10000
zerover	Yes	0.45308	0.45925	-0.00617	0.00000	0.45308	0.10000
detrotx	Yes	0.47287	0.46517	0.00771	0.00000	0.47287	0.20000
detroty	Yes	0.08671	0.08803	-0.00133	0.00000	0.08671	0.20000
detrotz	Yes	-0.13997	-0.13243	-0.00754	0.00000	-0.13997	0.20000
swing	Fix	0.00000			0.00000		0.10000
xtalx	Yes	-0.02402	-0.01411	-0.00991	0.00000	-0.02402	0.10000
xtaly	Yes	-0.04288	-0.04372	0.00085	0.00000	-0.04288	0.10000
xtalz	Fix	0.00000			0.00000		0.10000
gonio1	Yes	0.00988	0.00000	0.00988	0.00000	0.00988	0.10000
gonio2	Yes	-0.01245	0.00000	-0.01245	0.00000	-0.01245	0.10000
gonio3	Fix	0.00000			0.00000		0.10000
focusdist	Fix	1000.00000			1000.00000		10.00000

Table 4.6: Status after refining all the parameters. 679 of 960 reflections are used in the refinement (Part 2).

focushor	No	0.00000			0.00000		0.10000
focusver	No	0.00000			0.00000		0.10000
rotax1	Fix	0.00000			0.00000		0.10000
rotax2	Fix	1.00000			1.00000		0.10000
rotax3	Fix	0.00000			0.00000		0.10000
kch1	Fix	1.00000			1.00000		0.10000
kch2	Fix	0.00000			0.00000		0.10000
kch3	Fix	0.00000			0.00000		0.10000
swing1	Fix	0.00000			0.00000		0.10000
swing2	Fix	1.00000			1.00000		0.10000
swing3	Fix	0.00000			0.00000		0.10000
lambda	Fix	0.49999			0.49999		0.01000
Vol		829.14	829.25	-0.11	828.87	0.26	655
mm		0.01745	0.01777	-0.00032	0.38030	-0.36285	655
mmAng	+	0.00444	0.00453	-0.00008	0.09684	-0.09240	655
rotpartial	+	0.00000	0.00000	0.00000	0.00000	0.00000	0
rotoutside		0.14150	0.13766	0.00383	0.04289	0.09861	608
rotinside		0.00000	0.00000	0.00000	0.00000	0.00000	47
rotall		0.13134	0.12610	0.00524	0.00805	0.12329	655
res		0.00444	0.00453	-0.00008	0.09684	-0.09240	

1 refers to the angles ($^{\circ}$) (compared with 90° and 120°).

Peakref> go3

- Give the crystal-detector distance free and redo the refinement:

Peakref> free zerodist

Peakref> go3

- Switch to expert mode, give the “detrot” free and redo the refinement:

Peakref> expert on

Peakref> free detrot

Peakref> go3

- Give the “crystal” free and redo the refinement:

Peakref> free xtal

Peakref> go3

- Give the “gonio” free and redo the refinement:

Peakref> free gonio*

Peakref> go3

- Reindex the peaks and redo the refinement:

Peakref> reind

Peakref> go3

- Save the results:

Peakref> save save *detalign.vic* for detector alignment

Peakref> savegonio save *goniostat.vic* for goniometer alignment

Peakref> savextal save *xtalshift.pic* for crystal shift

Peakref> savermat save *ir.rmat* for orientation matrix

- Quit the peak refinement program PEAKREF :

Peakref> exit

The status of the refinement are given in Table 4.5 and Table 4.6. The refined

Table 4.7: Result of second run of DIRAX , Acl is the number of the solution, and H is the number of vector fitted to the solution. Parameters of the unit cell: a, b , c , alpha, beta, gamma and volume are given. Solution number 452 with same unit cell parameter as the first run of DIRAX is selected.

Acl	H	a	b	c	alpha	beta	gamma	Volume
819	590	7.205	12.567	27.471	90.02	90.03	90.03	2487
817	590	7.205	12.566	27.471	90.02	90.03	90.03	2487
791	606	7.204	12.565	27.473	89.99	89.98	90.05	2487
766	592	7.205	12.567	27.471	90.02	90.03	90.03	2487
677	502	7.204	9.156	12.566	89.98	90.04	89.98	829
674	599	7.202	12.565	27.473	90.01	90.00	90.05	2486
638	502	7.202	9.157	12.565	90.02	90.06	90.01	829
626	502	7.203	9.157	12.565	89.98	90.05	89.99	829
553	504	7.207	9.156	12.567	90.03	89.99	89.97	829
542	498	7.199	9.153	12.569	90.03	89.99	90.07	828
452	512	7.204	9.156	12.566	90.03	89.97	89.99	829
265	241	7.208	12.568	9.464	90.03	104.72	90.00	829
253	241	7.210	12.568	9.464	90.03	104.66	90.01	830
246	490	7.204	9.155	12.567	90.03	90.02	90.01	829
135	165	3.603	12.566	15.209	114.38	96.76	90.01	622
126	500	7.201	9.157	12.564	89.98	90.07	90.00	828
104	75	4.779	4.914	5.614	93.94	111.33	102.40	118
94	17	4.400	5.189	5.404	88.82	72.32	83.98	117
65	3	2.228	2.613	2.857	114.82	92.95	97.35	15

lattice parameters together with the experimental parameters give a much smaller residual value of 0.00444 as compared to the initial value of 0.09684 (Table 4.4).

4.3.3 Finding the \mathbf{q} -vector

The experimental parameters have been refined against the main reflections in the last run of PEAKREF, the PEAKSEARCH will start again with the refined parameters, so that the position of reflections are more accurate and the \mathbf{q} -vector is expect to be found.

- Build the script:
`~/rbzncl> buildsearch`

Table 4.8: \mathbf{q} -vector found by DIRAX, qv is the number of solution, $nhit$ is the number fitted to the solution, and the components of the \mathbf{q} -vector are given, solution number 1 is selected.

qv	nhit	qvector			fom
1	123	0.0011	0.3170	-0.0007	0.2746
3	112	-0.0184	-0.0082	0.0085	0.2500
27	88	0.0054	-0.3128	-0.0037	0.1964
2	44	0.0146	0.0073	-0.0072	0.0982
14	14	0.0136	0.3257	-0.0096	0.0313
54	6	0.0214	0.0259	-0.0305	0.0134
12	4	0.0354	0.0102	-0.0086	0.0089
20	2	0.0165	0.3664	0.0022	0.0045
57	2	0.0173	-0.2975	-0.0231	0.0045

Prefix name: b , the parameters are saved in the file $bsearch.vic$. Select search type 3, Search five peaks per frame.

- Do the peak search:
~/rbzncl> view
- Read-in one frame:
View> read s04f0001
- Do the peak search:
View> @bsearch
- Quit the program VIEW :
View> exit

The results of the peak search are written into the files $b1.pk$ and $b1.drx$.

The indexing is done again to find the \mathbf{q} -vector with the program DIRAX.

- Launch the DIRAX program:
~/rbzncl> dirax
- Read-in the .drx file:
Dirax> read b1.drx

Table 4.9: Starting status of PEAKREF, 909 of 960 reflections fitting with the orientation matrix.

	ref	current	previous	change	initial	change	shift
a	No	7.20446			7.20446		0.03602
b	No	9.15600			9.15600		0.04578
c	No	12.56652			12.56652		0.06283
alpha	Fix	90.00000			90.02519		1.00000
beta	Fix	90.00000			89.97156		1.00000
gamma	Fix	90.00000			89.99110		1.00000
orx	No	0.85011			0.85011		0.00202
ory	No	-0.48650			-0.48650		0.00202
ora	No	-145.16870			-145.16870		1.00000
zerodist	No	0.00000			0.00000		0.10000
zerohor	Yes	0.00000	0.00000	0.00000	0.00000	0.00000	0.10000
zerover	Yes	0.00000	0.00000	0.00000	0.00000	0.00000	0.10000
xtalx	No	0.00000			0.00000		0.10000
xtaly	No	0.00000			0.00000		0.10000
xtalz	Fix	0.00000			0.00000		0.10000
qvx1	No	0.00000			0.00000		0.01000
qvy1	No	0.31600			0.31600		0.01000
qvz1	No	0.00000			0.00000		0.01000
Vol		828.94	828.94	0.00	828.94	0.00	909
mm		0.06237	0.02096	0.04141	0.02096	0.04141	909
mmAng	+	0.01584	0.00532	0.01052	0.00532	0.01052	909
rotpartial	+	0.00000	0.00000	0.00000	0.00000	0.00000	0
rotoutside		0.02526	0.02443	0.00083	0.02443	0.00083	95
rotinside		0.00000	0.00000	0.00000	0.00000	0.00000	814
rotall		0.00264	0.00207	0.00057	0.00207	0.00057	909
res		0.01584	0.00532	0.01052	0.00532	0.01052	

- Start the indexing:

```
Dirax> go
```

The index result is given in Table 4.7.

- Check for the \mathbf{q} -vector:

```
Dirax> qvtest
```

The result is given in Table 4.8

In case, that the values are not satisfying and that the \mathbf{q} -vector components are already known, one might set them with the command `qvector` .

- Use \mathbf{q} -vector solution number 1 to index the satellite reflections

```
Dirax> sethklm
```

- Save the found orientation matrix and \mathbf{q} -vector:

```
Dirax> ccd b
```

The matrix is saved to the file `b.rmat` .

- Quit the indexing program DIRAX :

```
Dirax> exit
```

Start PEAKREF again, use the `b1.pk` to refine against orientation matrix and the experimental parameters. Repeat all the procedures as last refinement, the start and end status are given in Table 4.9, Table 4.10 and Table 4.11. 909 of 960 found reflections are indexed by `b.rmat` with \mathbf{q} -vector, comparing with the previous index of 679 of 960 reflections without \mathbf{q} -vector.

4.3.4 Integration

- Build a script for data integration:

```
~/rbzncl> bulddatcol
```

Select the synchrotron radiation type, `3mm` for box size and `5` for maximum duration. This generates the files `datcolsetup.vic` , `datcol.vic` , and `datcols04f.vic` , as well as the sub-directory `br` (file name of the `br.rmat`) in which the `.shoe` box files are saved.

Table 4.10: Final status of PEAKREF, 909 of 960 reflections fitting with the orientation matrix (Part 1).

	ref	current	previous	change	initial	change	shift
a	Yes	7.20736	7.20708	0.00028	7.20446	0.00290	0.03602
b	Yes	9.15406	9.15409	-0.00002	9.15600	-0.00194	0.04578
c	Yes	12.56934	12.56899	0.00034	12.56652	0.00282	0.06283
alpha	Fix	90.00000			90.02519		1.00000
beta	Fix	90.00000			89.97156		1.00000
gamma	Fix	90.00000			89.99110		1.00000
orx	Yes	0.84941	0.84948	-0.00007	0.85011	-0.00070	0.00202
ory	Yes	-0.48760	-0.48745	-0.00015	-0.48650	-0.00110	0.00202
ora	Yes	-145.23541	-145.22401	-0.01139	-145.16870	-0.06672	1.00000
zerodist	Yes	0.00817	0.00603	0.00214	0.00000	0.00817	0.10000
zerohor	Yes	0.01645	0.00183	0.01463	0.00000	0.01645	0.10000
zerover	Yes	-0.03737	-0.02178	-0.01559	0.00000	-0.03737	0.10000
detrotx	Yes	0.00936	0.00238	0.00698	0.00000	0.00936	0.20000
detroty	Yes	-0.00843	-0.00311	-0.00532	0.00000	-0.00843	0.20000
detrotz	Yes	-0.00355	-0.00092	-0.00264	0.00000	-0.00355	0.20000
swing	Fix	0.00000			0.00000		0.10000
xtalx	Yes	-0.05056	-0.03852	-0.01204	0.00000	-0.05056	0.10000
xtaly	Yes	-0.04440	-0.04284	-0.00156	0.00000	-0.04440	0.10000
xtalz	Fix	0.00000			0.00000		0.10000
gonio1	Yes	0.05883	0.03109	0.02773	0.00988	0.04895	0.10000
gonio2	Yes	-0.04655	-0.04008	-0.00646	-0.01245	-0.03410	0.10000
gonio3	Fix	0.00000			0.00000		0.10000
focusdist	Fix	1000.00000			1000.00000		10.00000

Table 4.11: Final status of PEAKREF, 909 of 960 reflections fitting with the orientation matrix (Part 2).

	ref	current	previous	change	initial	change	shift
focushor	No	0.00000			0.00000		0.10000
focusver	No	0.00000			0.00000		0.10000
rotax1	Fix	0.00000			0.00000		0.10000
rotax2	Fix	1.00000			1.00000		0.10000
rotax3	Fix	0.00000			0.00000		0.10000
kch1	Fix	1.00000			1.00000		0.10000
kch2	Fix	0.00000			0.00000		0.10000
kch3	Fix	0.00000			0.00000		0.10000
swing1	Fix	0.00000			0.00000		0.10000
swing2	Fix	1.00000			1.00000		0.10000
swing3	Fix	0.00000			0.00000		0.10000
lambda	Fix	0.49999			0.49999		0.01000
qvx1	No	0.00000			0.00000		0.01000
qvy1	Yes	0.31640	0.31600	0.00040	0.31600	0.00040	0.01000
qvz1	No	0.00000			0.00000		0.01000
Vol		829.28	829.23	0.05	828.94	0.34	909
mm		0.01895	0.01904	-0.00009	0.02096	-0.00202	909
mmAng	+	0.00481	0.00484	-0.00002	0.00532	-0.00051	909
rotpartial	+	0.00000	0.00000	0.00000	0.00000	0.00000	0
rotoutside		0.04817	0.05061	-0.00243	0.02443	0.02374	253
rotinside		0.00000	0.00000	0.00000	0.00000	0.00000	656
rotall		0.01341	0.01614	-0.00274	0.00207	0.01134	909
res		0.00481	0.00484	-0.00002	0.00532	-0.00051	

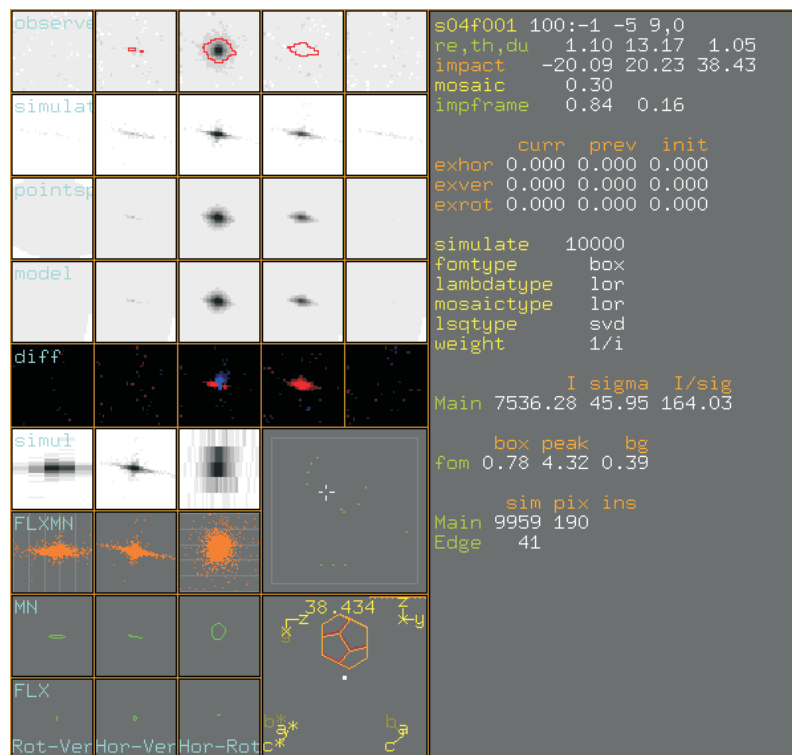


Figure 4.3: The EVAL15 program window of reflection $(-1, -5, 9, 0)$ with the initial parameters (mosaicity = 0.3, pointsreadgamma = 0.8).

- Start to create the boxes:

```
~/rbzncl> view @datcol
```

- Create a sub-directory for EVAL15:

```
~/rbzncl> mkdir e15
```

- Create soft links to the .shoe files:

```
~/e15> ln -s ../br/* .
```

- Build the initscript-files:

```
~/e15> buldeval15
```

Choose `synchrotron` for the `focustype`. Accept all other proposed default values. The following files are created:

- `eval15.init` initialization file
- `spectrum.pic` defines the wavelength parameters, i.e., the X-ray spectrum
- `focus.pic` defines the X-ray focus
- `detector.pic` defines the detector parameters, i.e., pointspread and noise
- `crystal.pic` defines the crystal model
- `simulation.pic` builds the reflection model
- `refine.pic` to save changed value after refinement
- `mosaic.pic` defines mosaicity and lattice distortion of the crystal

- Copy the file `xtalshift.pic` generated by `PEAKREF` to the present folder:

```
~/rbzncl/e15> cp ../xtalshift.pic .
```

- These default parameters have to be adapted now to the actual measurement with the program `EVAL15`. `EVAL15` is launched by the command:

```
~/e15> eval15
```

- Read in reflection:

```
~/e15> file 1 100
```

- Refine the profile of this reflection

```
~/e15> refine
```

- Examine the mosaicity of the crystal:

One uses a peak which appear on several continuous frames, that indicates a large duration value.

- Skip reflections with small duration (i.e., duration $< 1^\circ$):
Refl nr [100] dur
- Refine this peak with larger duration:
Refl nr [100] refine
Refl nr [100] distribution type onescan
Refl nr [100] delay 0
Refl nr [100] fomtype peak
Refl nr [100] onescan mosaic 0.02 0.02 0.54
Write down reflex number, $\frac{I}{\sigma(I)}$, and the found mosaicity.

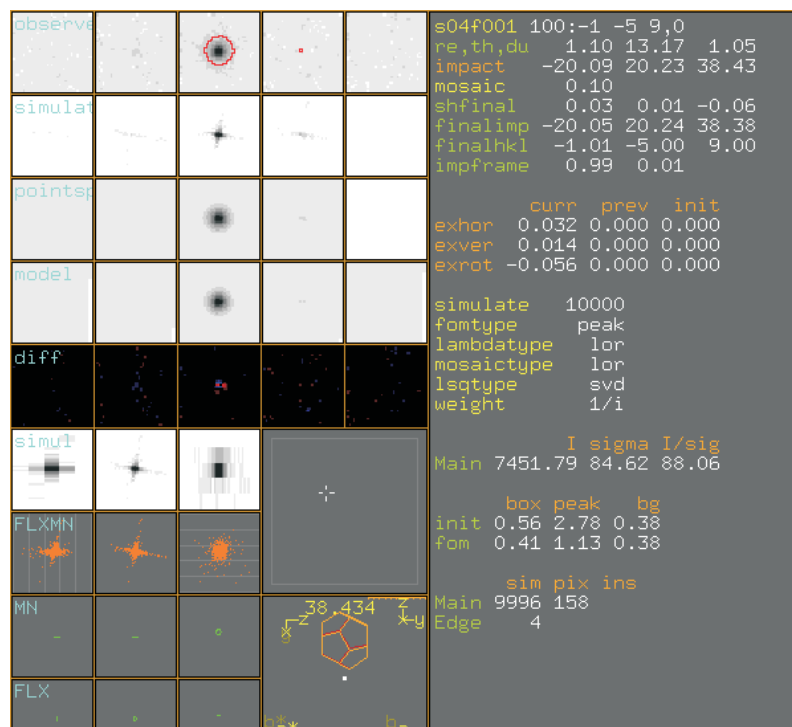


Figure 4.4: The EVAL15 program window of reflection (-1, -5, 9, 0) with the refined parameters (mosaicity = 0.1, pointspreadgamma = 1.2).

- Reset the fomtype :
Refl nr [100] fomtype box

- Set the mosaicity:
Refl nr [100] mosaic 0.1
- Analysis the pointspread of the detector:
- Skip reflections with $\frac{I}{\sigma(I)}$ smaller than 75:
Refl nr [100] pq75
- Refine this strong peak:
Refl nr [108] refine
- Get the pointspread:
Refl nr [108] distribution type onescan
Refl nr [108] delay 0
Refl nr [108] fomtype peak
Refl nr [108] onescan pntspr 0.05 0.05 2.00
Write down reflex number, $\frac{I}{\sigma(I)}$, and the found pointspread.
- Reset the fomtype :
Refl nr [108] fomtype box
- Set the pointspread:
Refl nr [108] pointspreadgamma 1.2

Comparing the EVAL15 predicted profile of reflection (-1, -5, 9, 0) before refinement (Figure 4.3) to the predicted profile after refinement (Figure 4.4), the refinement improve the fit of predicted profile to the observed reflection profile. Now, start the integration of all these box files with the tuned parameters by EVAL15ALL .

- Launch the program:
~/e15> eval15all
This will generate the output files s04fxxx.y , as well as s04fxxx.log , s04fxxx.evc , pixel15.summary , and the final.y .

4.3.5 Data analysis and data reduction

With the program `ANY` the `final.y` files can be analysed and a standard reflection file in *hkl*-format can be generated for further work.

- Create a subdirectory `any` in the directory `~/e15/` and launch the program:

```
~/e15/> mkdir any
```

```
~/e15/> cd any
```

```
~/any> any
```

Read in the `final.y` file:

```
~/any> read ../final.y
```

- Check the shift of the peak positions:

```
Any> plot shiftver (Figure 4.5)
```

```
Any> plot shifthor (Figure 4.6)
```

```
Any> plot shiftrot (Figure 4.7)
```

- Define limit for the shift of reflections:

```
Any> limit shiftrestfrac 0.1 = yes
```

```
Any> pkfile final1.pk
```

```
Any> pk
```

The reflections within the shift range of $0.1mm$ are saved to *final1.pk*

After this data integration, more reflections are found with accurate position, then these reflections are used again to refine the `.rmat` file.

Repeat the `PEAKREF` again, use this *final1.pk* file and the *br.rmat* file. After the refinement save the orientation matrix to file *c.rmat*. In *c.rmat*, change the vector order from 1 to 5. So the higher order satellite reflections can be integrated with *c.rmat*.

- Build a script for data integration:

```
~/rbzncl> bulddatcol
```

Select the synchrotron radiation type, $3mm$ for box size and 5 for maximum duration. This generates the files `datcol2setup.vic`, `datcol2.vic`, and `datcol2s04f.vic`, as well as the sub-directory `c` (filename of the *c.rmat* -file) in which the `.shoe` box files are saved.

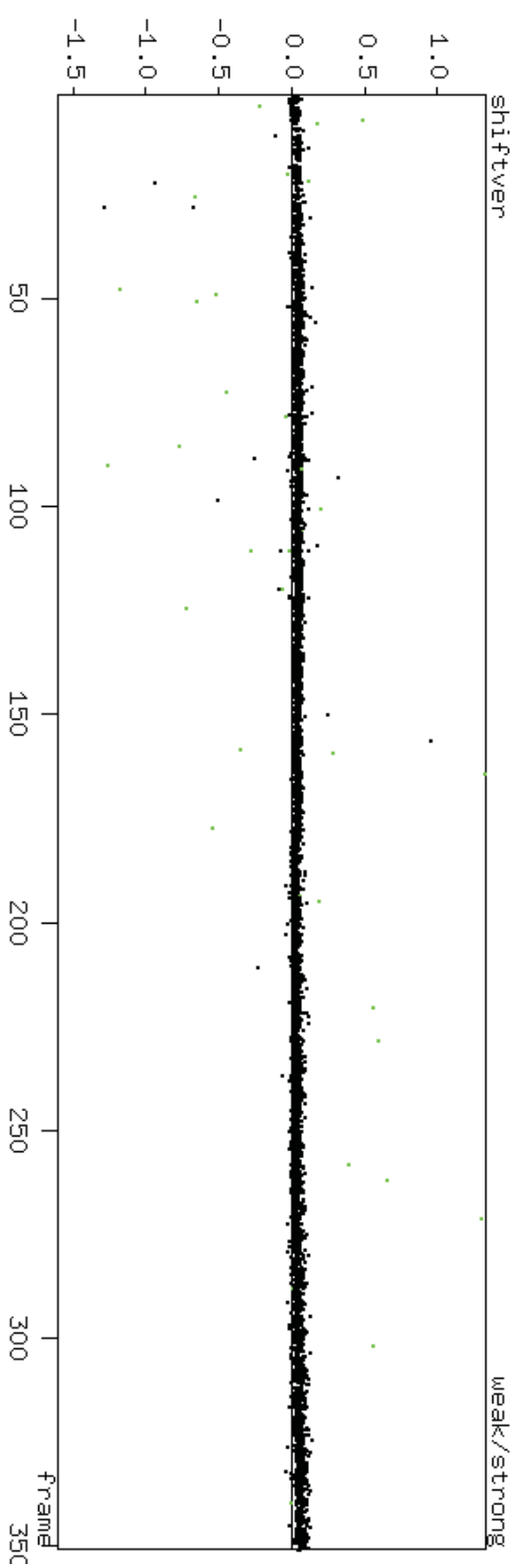


Figure 4.5: The ANY program window of vertical shift of all the reflections via frame number, the shift is given in *mm*. Black dots stand for strong reflections ($I/\sigma \geq 2.5$) and green dots for weak reflection ($I/\sigma < 2.5$).

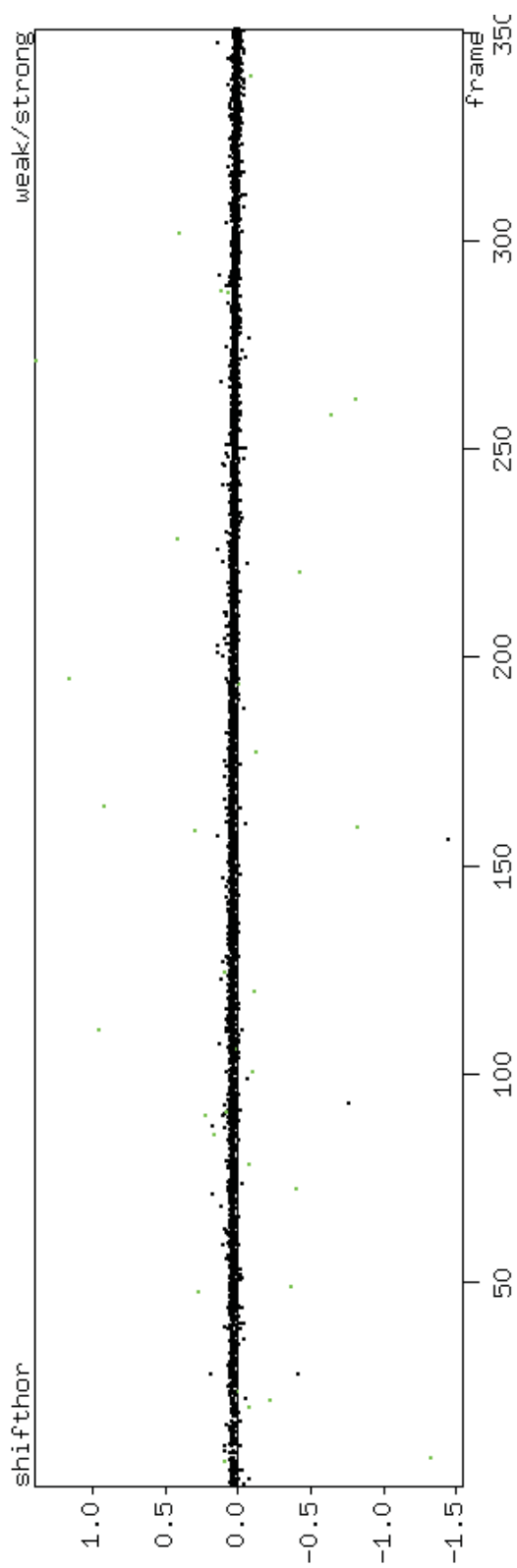


Figure 4.6: The ANY program window of horizontal shift of all the reflections via frame number, the shift is given in mm . Black dots stand for strong reflections ($I/\sigma \geq 2.5$) and green dots for weak reflection ($I/\sigma < 2.5$).

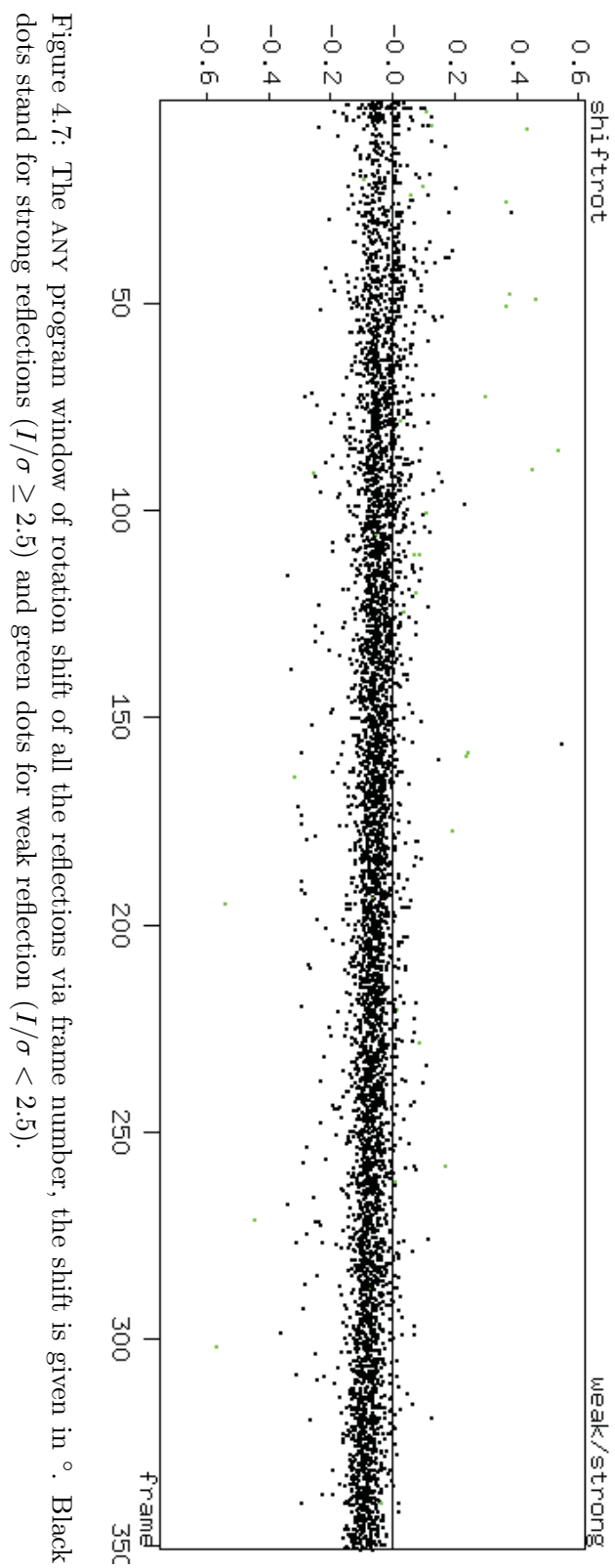


Figure 4.7: The ANY program window of rotation shift of all the reflections via frame number, the shift is given in $^{\circ}$. Black dots stand for strong reflections ($I/\sigma \geq 2.5$) and green dots for weak reflection ($I/\sigma < 2.5$).

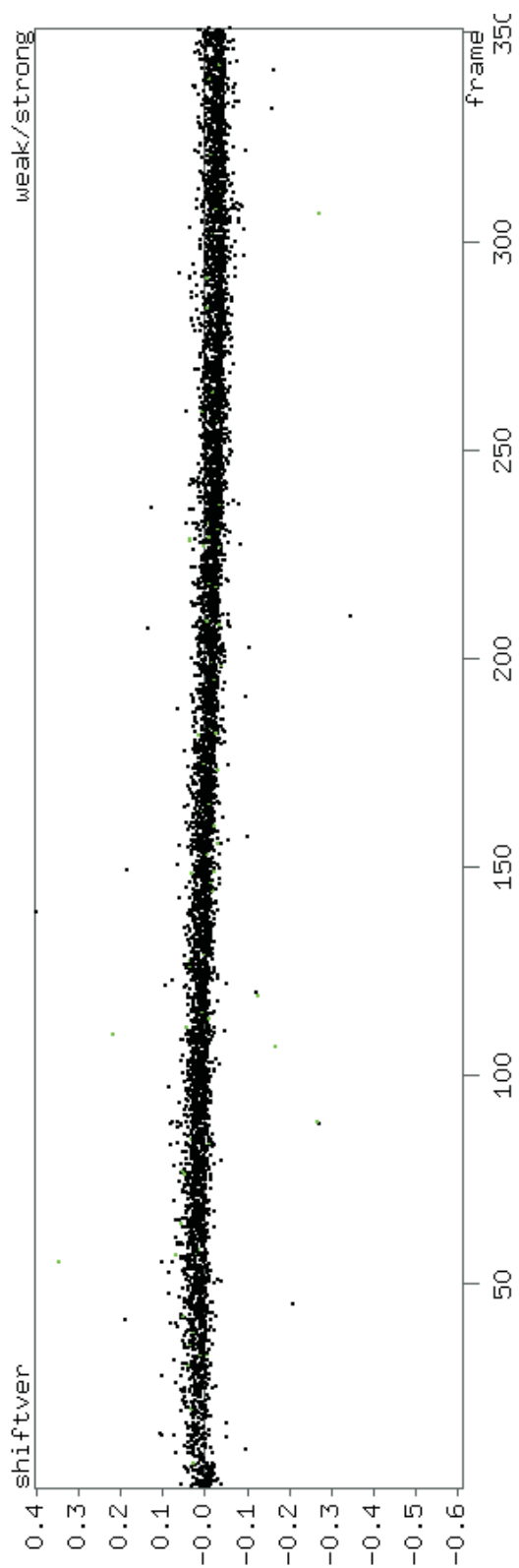


Figure 4.8: The ANY program window of vertical shift of all the reflections via frame number, the shift is given in mm . Black dots stand for strong reflections ($I/\sigma \geq 2.5$) and green dots for weak reflection ($I/\sigma < 2.5$).

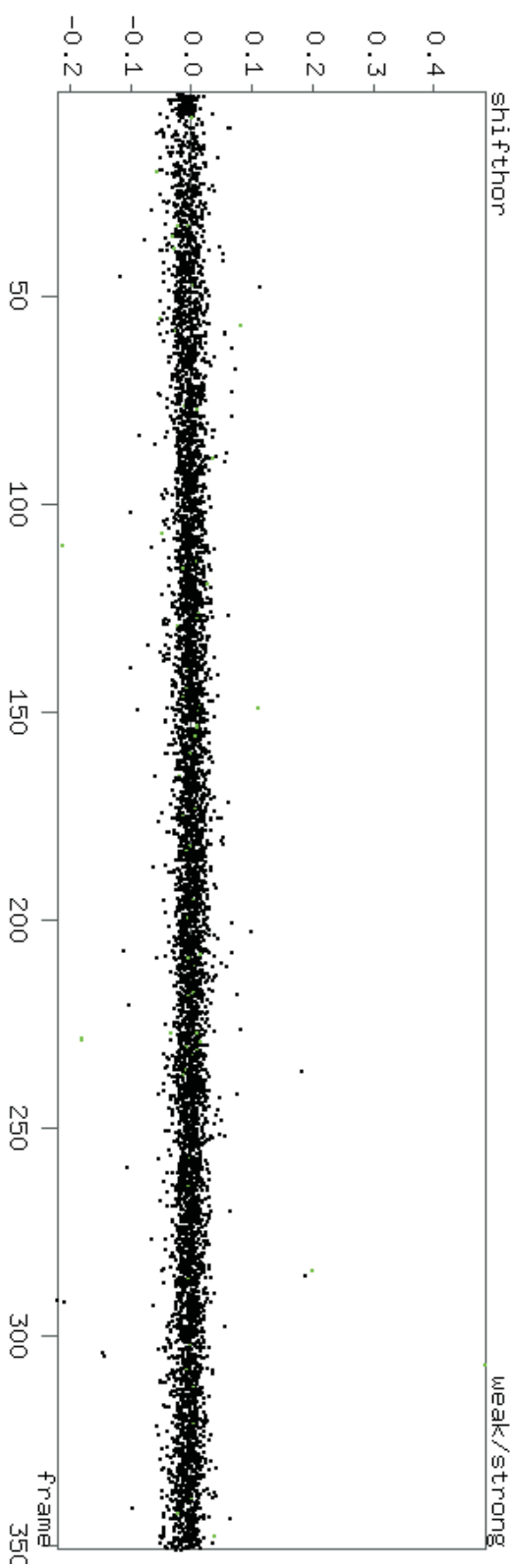


Figure 4.9: The ANY program window of horizontal shift of all the reflections via frame number, the shift is given in *mm*. Black dots stand for strong reflections ($I/\sigma \geq 2.5$) and green dots for weak reflection ($I/\sigma < 2.5$).

- Start to create the boxes:

```
~/rbzncl> view @datcol2
```

The .shoe boxes are saved in the directory *c*.

The EVAL15 runs in the new directory *e15a*.

- Create soft links to the .shoe files:

```
~/e15a> ln -s ../c/* .
```

- Copy these EVAL15 files from directory *e15*: *eval15.init*, *spectrum.pic*, *focus.pic*, *detector.pic*, *crystal.pic*, *simulation.pic*, *refine.pic*, *mosaic.pic* and the *xtalshift.pic* file which is generated by the last refinement.

- Launch the program:

```
~/e15a> eval15all
```

- Create a sub-directory *any* in the directory *~/e15a/* and launch the program:

```
~/e15a/> mkdir any
```

```
~/e15a/> cd any
```

```
~/any> any
```

Read in the *final.y* file:

```
~/any> read ../final.y
```

- Check the shift of the peak positions:

```
Any> plot shiftver (Figure 4.8)
```

```
Any> plot shifthor (Figure 4.9)
```

```
Any> plot shiftrot (Figure 4.10)
```

```
Any> pkfile final2.pk
```

```
Any> pk
```

In the data integration with *c.rmat*, except the main reflections and the first order satellite reflections, satellite reflections with order higher than one are integrated, and they have smaller shift in vertical, horizontal and rotation directions (Figure 4.8, Figure 4.9 and Figure 4.10), comparing with the shift plot of integration done with orientation matrix file *br.rmat* (Figure 4.5, Figure 4.6 and Figure 4.7). The shift plots of integration done

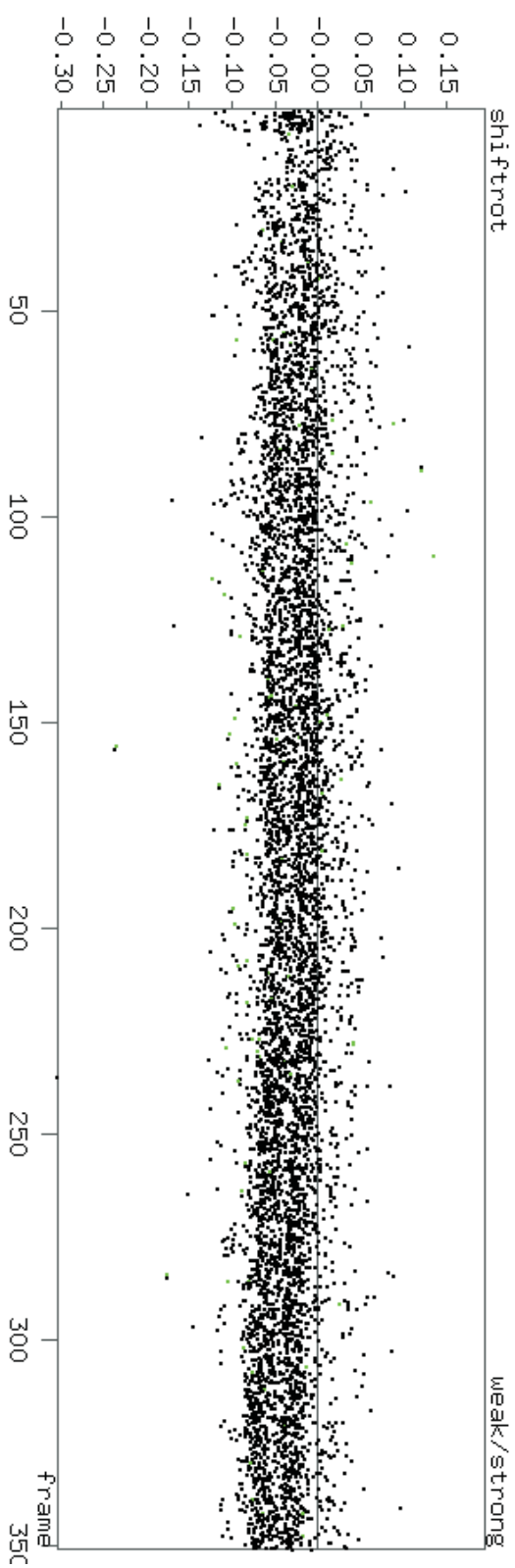


Figure 4.10: The ANY program window of rotation shift of all the reflections via frame number, the shift is given in $^{\circ}$. Black dots stand for strong reflections ($I/\sigma \geq 2.5$) and green dots for weak reflection ($I/\sigma < 2.5$).

Table 4.12: Content of the `badmask.vic`. Poistion of points are given in unit of pixel number

badmaskarea	1708	1645	1718	1655
badmaskarea	679	757	689	767
badmaskarea	1156	841	1166	851
badmaskarea	1414	760	1424	770
badmaskarea	889	1813	899	1823
badmaskarea	1237	1882	1247	1892
badmaskarea	1042	1507	1052	1517
badmaskarea	961	1552	971	1562
badmaskarea	1516	1798	1526	1808
badmaskarea	1669	1435	1679	1445
badmaskarea	1069	127	1079	137
badmaskarea	832	112	842	122
badmaskarea	808	274	818	284
badmaskarea	688	238	698	248
badmaskarea	1012	118	1022	128
badmaskarea	1306	169	1316	179
badmaskarea	1384	970	1394	980
badmaskarea	1660	433	1670	443
badmaskarea	1561	196	1571	206
badmaskarea	1348	163	1358	173
badmaskarea	529	229	539	239

with orientation matrix file `c.rmat`, is more successfully done with accurate determined orientation matrix and experimental parameters. The new created `final2.pk` will be read in JANA2006 and used for further studies.

4.4 Special problem in CCD detector data integration.

Area detector has many advantages in the data collection procedure, but the disadvantages always come together with it. During our data collection performed at beamline F1 Hasylab at Hamburg, the cooling system can not cool all pixels down to the same range, even worse, some pixels are too hot to record the reflection density. These over heated pixels have high intensities on the frames, but they are not real

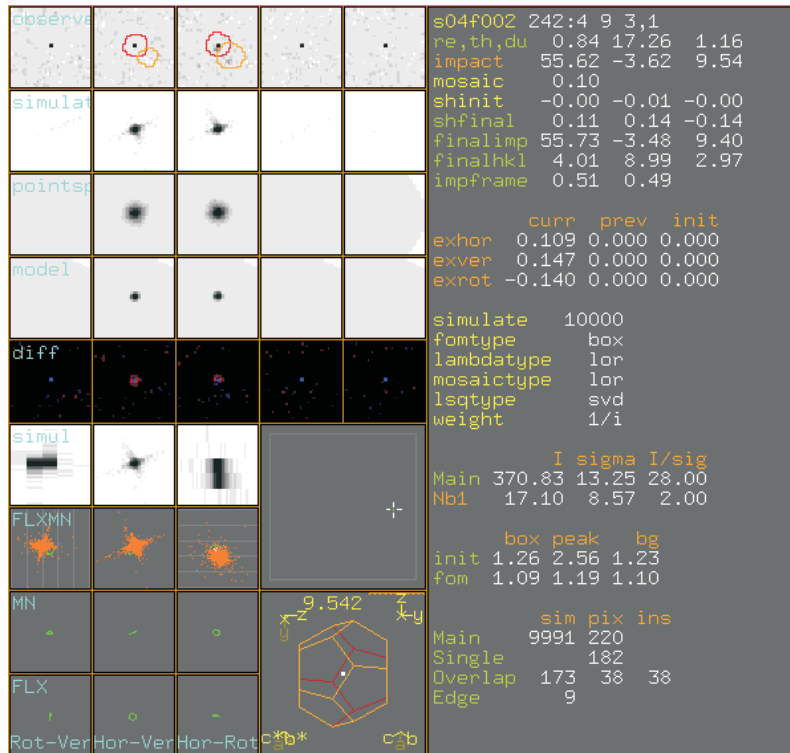


Figure 4.11: The EVAL15 program window of reflection (4, 9, 3, 1). The intensity from bad pixels are integrated as reflection intensity.

reflections and are called bad pixels.

These bad pixels will be interpreted as reflection intensity which leads to wrong structure factors. One example reflection which is incorrectly integrated is given in Figure 4.11. To eliminate this effect, one can exclude these bad region by create a file `badmask.vic` (Table 4.12), in which bad region is defined by two points: the left down and upper right points of a rectangular which can cover the bad pixels region. The coordinates of wanted pixels can be found in `VIEW`. The bad pixels region defined in `badmask.vic` will not be integrated by `EVAL15ALL` (Figure 4.12).

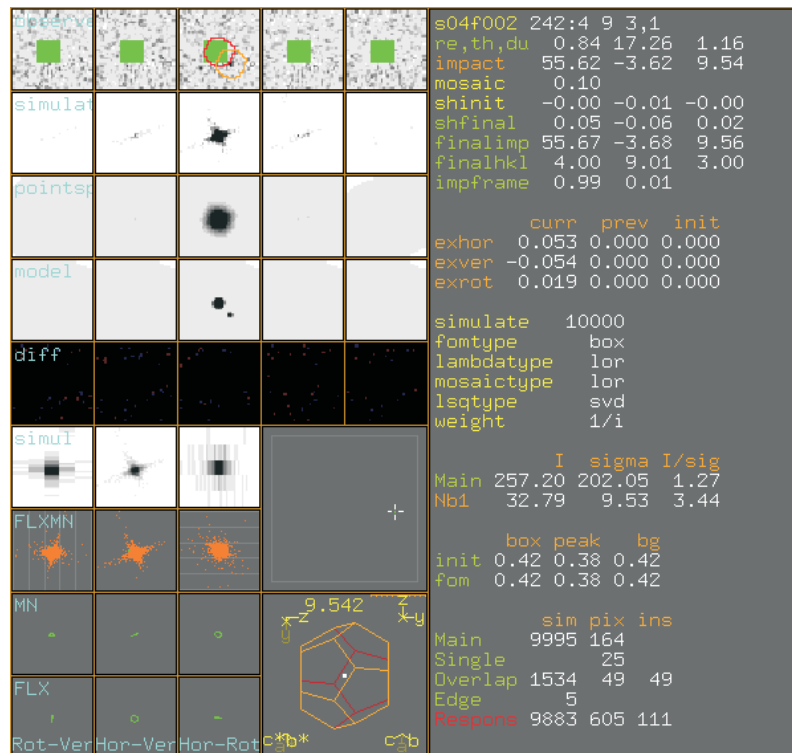


Figure 4.12: The EVAL15 program window of reflection (4, 9, 3, 1). The region contain bad pixels is excluded from integration.

Chapter 5

Incommensurately modulated Rb_2ZnCl_4

5.1 Abstract

A combination of structure refinements, interpretation of difference-Fourier maps and the analysis of the superspace MEM-density has been used to characterize the incommensurate modulation of rubidium tetrachlorozincate, Rb_2ZnCl_4 , at a temperature of $T = 196$ K, close to the lock-in transition at $T_{lock-in} = 192$ K. The modulation is found to consist of a combination of displacement modulation functions, modulated atomic displacement parameters (ADPs) and modulated third-order anharmonic ADPs. Up to fifth-order Fourier coefficients could be refined against diffraction data containing up to fifth-order satellite reflections. The center-of-charge of the atomic basins of the MEM-density and the displacive modulation functions of the structure model provide equivalent descriptions of the displacive modulation. Modulations of the ADPs and anharmonic ADPs are visible in the MEM density, but extracting quantitative information about these modulations appears to be difficult. In the structure refinements, the modulation parameters of the ADPs form a dependent set, and *ad hoc* restrictions had to be introduced in the structure refinements. It is suggested that modulated harmonic ADPs and modulated third-order anharmonic ADPs form an intrinsic part—however small—of

incommensurately modulated structures in general. Refinements of alternate models with and without parameters for modulated ADPs lead to significant differences between the parameters of the displacement modulation in these two models, thus showing the modulation of ADPs to be important for a correct description of the displacive modulation. The resulting functions are not in agreement with an interpretation as a soliton wave, contrary to a previous proposal by Aramburu et al. (2006) [Phys. Rev. B **73**, 014112.]

5.2 Introduction

The construction of a model-independent electron density map from phased structure factors is an important application of the Maximum Entropy Method (MEM) in crystallography (Takata, 2008; van Smaalen and Netzel, 2009). The analysis of the electron density after such a reconstruction provides the locations of the atoms in the unit cell. As such, the MEM has been used to determine the locations of the metal atoms in endohedral fullerenes (Nishibori et al., 2006), to obtain information about disorder (multiple positions) in crystal structures (Dinnebier et al., 1999; Wang et al., 2001; Samy et al., 2010) and about anharmonic atomic displacements (Kumazawa et al., 1995; Bagautdinov et al., 1998).

The MEM has been generalized towards the determination of the generalized electron density in $(3 + d)$ -dimensional superspace ($d = 1, 2, 3, \dots$) of aperiodic crystals (van Smaalen et al., 2003). Again, the MEM provides information about the locations of the atoms. The latter then result in a description of the modulation functions of incommensurately modulated crystals or incommensurate composite crystals (Palatinus and van Smaalen, 2004; van Smaalen and Li, 2009). Alternatively, the MEM in superspace has been used to determine the occupation domains of the atoms in quasicrystals (Yamamoto et al., 1996). Here we will use the MEM to obtain information about the modulation functions of incommensurately modulated Rb_2ZnCl_4 . Many isostructural compounds of the β - K_2SO_4 structure type undergo phase transitions on cooling. Several compounds exhibit at least two phase transitions, first forming an incommensurately modulated structure which then becomes commensurate at lower temperatures (lock-in transition) (Cummins, 1990).

Table 5.1: Experimental and crystallographic data

Chemical formula	Rb ₂ ZnCl ₄
Crystal system	Orthorhombic
Superspace group	<i>Pmcn</i> (00 σ_3) <i>ss</i> $\bar{1}$
<i>a</i> (Å)	7.2272 (3)
<i>b</i> (Å)	12.6134 (8)
<i>c</i> (Å)	9.1858 (8)
Unit cell volume (Å ³)	837.378 (78)
<i>Z</i>	4
Modulation wavevector	[0, 0, 0.316(2)]
Crystal dimensions (mm ³)	0.1 × 0.1 × 0.12
Temperature (K)	196
Radiation type	Synchrotron (HASYLAB, Hamburg, Germany)
Wavelength (Å)	0.5000
Diffractometer	Huber four-circle diffractometer (Kappa geometry)
Detector	marCCD 165
($\sin(\theta)/\lambda$) _{max} (Å ⁻¹)	0.86
$\Delta\phi$ (°)	0.3
$\Delta\omega$ (°)	0.3
Exposure time (s)	2, 8, 64
Absorption Correction	SADABS
Linear Absorption coefficient (mm ⁻¹)	6.08
Transmission (min/max)	0.5143 / 0.7506
Criterion of observability	$I > 3\sigma(I)$
R_{int} (obs/all)	0.029/0.032
No. of measured reflections	75610
No. of unique reflections (obs/all)	6245/19956
No. of main reflections (obs/all)	1825/1956
No. of first-order satellites (obs/all)	2617/3517
No. of second-order satellites (obs/all)	1088/3803
No. of third-order satellites (obs/all)	392/3261
No. of fourth-order satellites (obs/all)	86/3870
No. of fifth-order satellites (obs/all)	237/3549
Average redundancy	3.789
Refinement (model D _r)	
R_F	0.0563
wR_{F^2}	0.0705
GoF	3.28
MEM	
Number of pixels	72 × 128 × 96 × 48
Pixel size (Å ³)	0.100 × 0.099 × 0.096
R_F	0.0112
wR_{F^2}	0.0225

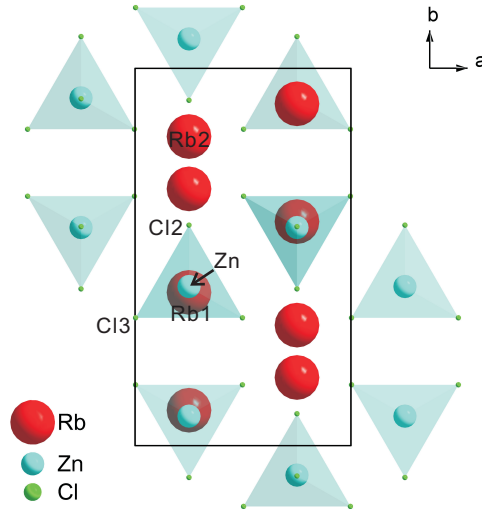


Figure 5.1: Basic structure of Rb_2ZnCl_4 . Atoms Rb1, Zn and Cl1 are nearly superimposed in this projection.

Table 5.2: Number of parameters for the different models. C_{ijk} and D_{ijkl} stand for the third- and fourth-order anharmonic ADPs. The models are defined in the text.

	Model A	Model B	Model C_r	Model C	Model D_r
x^0, y^0, z^0	13	13	13	13	13
ADP U_{ij}	26	26	26	26	26
C_{ijk}	–	–	0	0	0
D_{ijkl}	–	–	–	–	33
Modulation of x, y, z	100	100	100	100	100
Modulation of ADP	–	84	84	84	84
Modulation of C_{ijk}	–	–	132	244	132
Scale	1	1	1	1	1
Total	140	224	356	468	389

Rubidium tetrachlorozincate, Rb_2ZnCl_4 , is one of these compounds (Figure 5.1). Rb_2ZnCl_4 undergoes a phase transition from a periodic to an incommensurately modulated phase at $T_{inc} = 303$ K. The incommensurate modulation wavevector is $\mathbf{q} = (0, 0, 1/3 - \delta)$ ($\delta \approx 0.02$). The lock-in transition towards a threefold superstructure ($\delta = 0$) takes place at $T_{lock-in} = 192$ K (Sawada et al., 1977). The modulation of Rb_2ZnCl_4 increasingly deviates from a sinusoidal shape on approaching the lock-in transition, as it has been evidenced by the growth of the intensities of higher-order satellite reflections in the X-ray diffraction of this compound on cooling toward $T_{lock-in}$ (Aramburu et al., 1997). The results of structure refinements of a model of displacive modulation functions with up to fifth-order Fourier coefficients have been reported by Aramburu et al. (2006). The latter authors interpreted this structure model as providing evidence for a soliton shape of the incommensurate modulation wave.

Here we present a re-analysis of the incommensurate structure of Rb_2ZnCl_4 close to the lock-in transition, employing a more extensive data set of Bragg reflections than has been used by Aramburu et al. (2006). The purpose of this work is twofold. The first aim is to investigate the nature of modulations by means of the maximum entropy method (MEM). As we will show, modulations of atomic displacement parameters (ADPs) and modulations of anharmonic ADPs form an intrinsic and important part of the modulation. Secondly—based on a more accurate description of the displacive modulation of Rb_2ZnCl_4 —we show that a simple soliton wave does not form an appropriate characterization of the modulation in this compound.

5.3 Experimental

5.3.1 Crystal growth and the diffraction experiment

Single crystals of Rb_2ZnCl_4 have been grown from aqueous solution (Sawada et al., 1977). 2.73 g RbCl (Aldrich, 99.99%) and 1.54 g of ZnCl_2 (Aldrich, 99.999%) have been dissolved in 4.5 g ultra pure water (from a Simplicity UV system by Millipore) at $T = 323$ K. Crystals were grown by slow evaporation at $T = 313$ K.

A suitable single crystal was glued to a thin glass fibre mounted on a copper pin.

Table 5.3: Amplitudes of the displacement modulation functions of model A (relative coordinates multiplied by 10^5).

Atom	n	A_x^n	A_y^n	A_z^n	B_x^n	B_y^n	B_z^n
Rb1	1	1224(1)	0	0	-1215(1)	0	0
	2	0	-43(9)	82(10)	0	-242(8)	39(10)
	3	-291(14)	0	0	35(15)	0	0
	4	0	-380(30)	140(40)	0	200(30)	-90(40)
	5	68(18)	0	0	-38(18)	0	0
Rb2	1	1713(9)	0	0	-140(7)	0	0
	2	0	27(6)	-55(8)	0	33(6)	-15(8)
	3	-103(13)	0	0	-97(13)	0	0
	4	0	70(20)	-160(40)	0	-40(20)	230(40)
	5	161(14)	0	0	70(19)	0	0
Zn	1	998(8)	0	0	329(7)	0	0
	2	0	-30(7)	-9(9)	0	-22(7)	85(9)
	3	-25(13)	0	0	-99(13)	0	0
	4	0	-50(30)	-20(40)	0	-20(30)	110(50)
	5	-108(16)	0	0	11(17)	0	0
Cl1	1	4250(40)	0	0	660(30)	0	0
	2	0	-43(18)	-80(20)	0	-209(19)	-10(20)
	3	400(50)	0	0	240(50)	0	0
	4	0	300(60)	-260(80)	0	-210(60)	-110(70)
	5	110(70)	0	0	-140(70)	0	0
Cl2	1	760(30)	0	0	5480(40)	0	0
	2	0	27(17)	-90(20)	0	-98(16)	60(30)
	3	-380(50)	0	0	-1240(50)	0	0
	4	0	-10(50)	150(60)	0	110(50)	-150(70)
	5	100(70)	0	0	330(80)	0	0
Cl3	1	554(16)	2(13)	-1094(15)	-1939(17)	2635(15)	1334(15)
	2	65(18)	-26(15)	125(17)	126(18)	-57(16)	35(17)
	3	-230(20)	80(20)	30(30)	330(20)	-535(19)	-320(30)
	4	10(40)	20(40)	-140(50)	-300(40)	60(30)	250(50)
	5	-140(30)	0(30)	90(40)	-100(30)	250(30)	10(40)

Table 5.4: Quality of the fit to the diffraction data after refinements of models of increasing complexity. Given are R_F values of each order ($|m|$) of reflections, the number of parameters, $(\Delta\rho)_{max}$, $(\Delta\rho)_{min}$, the number of observed reflections $N(\text{obs})$ and the number of reflections N^* with $I > 5\sigma(I)$. Column D_r^* gives R values of model D_r calculated for the N^* reflections.

Present data	Model A	Model B	Model C _r	Model C	Model D _r	Model D _r [*]	N [*]
All	0.1047	0.0698	0.0634	0.0633	0.0563	0.0525	5145
$m = 0$	0.0776	0.0606	0.0561	0.0560	0.0493	0.0487	1773
$ m = 1$	0.1227	0.0703	0.0651	0.0650	0.0561	0.0537	2358
$ m = 2$	0.2388	0.1218	0.0988	0.0963	0.0969	0.0787	683
$ m = 3$	0.4807	0.2565	0.2045	0.2030	0.2003	0.1708	215
$ m = 4$	0.6203	0.3149	0.2890	0.3046	0.2987	0.2023	12
$ m = 5$	0.3434	0.2137	0.1757	0.1771	0.1619	0.1278	104
No. of parameters	140	224	356	468	389		
$(\Delta\rho)_{max}$ (e Å ⁻³)	4.85	2.11	2.17	2.18	1.71	1.74	
$(\Delta\rho)_{min}$ (e Å ⁻³)	-3.74	-2.61	-2.09	-2.09	-1.78	-1.71	

X-ray diffraction experiments were performed at beamline F1 of HASYLAB, DESY, Hamburg, employing radiation of a wavelength of 0.5000 \AA and a MAR-CCD area detector. The temperature of the sample was maintained at $T = 196 \text{ K}$, employing a nitrogen-flow cryostat. A large crystal-to-detector distance of 225 mm was chosen, in order to be able to resolve closely-spaced reflections. With aid of the four-circle kappa diffractometer at beamline F1, diffraction data were collected by ϕ and ω scans with a scan step of 0.3 degree per image. Several values were chosen for the off-set of the detector and for the orientation of the crystal, thus allowing the measurement of a nearly complete data set up to a high resolution of $[\sin(\theta)/\lambda]_{max} = 0.86 \text{ \AA}^{-1}$. With the purpose of increasing the effective dynamic range of the experiment, runs with zero detector off-set were repeated with exposure times of 2 and 8 seconds, and runs at higher scattering angles were repeated with 8 and 64 seconds exposure. The long exposure times resulted in overexposed strong (main) reflections, while they allowed weak reflections (mostly higher-order satellite reflections) to be measured.

Integrated intensities of Bragg reflections were extracted from the measured images by the software EVAL15 (Schreurs et al., 2010). Absorption correction was performed with SADABS (Sheldrick, 1996). A fraction of the area of the CCD detector was not properly cooled during parts of the experiment. This is a technical problem that occurred for experiments of long durations (Paulmann, 2009). As a result, several pixels of the detector always gave a large intensity, which could negatively affect data quality. Therefore, the coordinates of these pixels have been determined by inspection of the images, and they were excluded from the integration. Experimental data and crystallographic information are summarized in Table 5.1.

The resulting data set of intensities of Bragg reflections, including satellite reflections up to fifth order, was used for structure determination, structure refinements and maximum entropy calculations. Aramburu et al. (2006) have kindly supplied the diffraction data from their publication. These data will be denoted as the Aramburu-data. Various models have also been tested by calculation of the values of R indices on these data.

Peculiar property of Aramburu-data is that a selection of the satellite reflections has been measured, which included main reflections and only the strongest satellite

Table 5.5: R_F values on the Aramburu data of models of increasing complexity, after refinement of the scale parameter, the extinction coefficient, the ADP parameters and the atomic coordinates. Modulation parameters were kept fixed at their values obtained by refinements against the present data.

Pulished data	Model A	Model B	Model C _r	Model C	Model D _r	$N(\text{obs})$
All	0.0834	0.0917	0.0912	0.0912	0.0912	1695
$m = 0$	0.0784	0.0837	0.0828	0.0827	0.0826	778
$ m = 1$	0.0733	0.0855	0.0892	0.0900	0.0896	473
$ m = 2$	0.2281	0.3820	0.3564	0.3605	0.3569	251
$ m = 3$	0.4636	0.3049	0.2989	0.2859	0.2976	53
$ m = 4$	–	–	–	–	–	–
$ m = 5$	0.3647	0.2623	0.2807	0.2667	0.2867	140

reflections as expected on the basis of a soliton model. Satellite reflections up to order five, except fourth order have been measured in this way by Aramburu et al. (2006). The result is a data set that consists of much fewer reflections than available in the present data. On the other hand, CCD detectors have a limited dynamic range, so that the lower bound on measurable intensities is relatively high, resulting in a number of high-order satellite reflections of the type 'observed' that is comparable in both data sets.

5.3.2 Structure refinements

Structure models of different complexity have been refined against the diffraction data. They involve the basic-structure coordinates (x^0, y^0, z^0) and the harmonic atomic displacement parameters (ADPs) U_{ij} for each of the six crystallographically independent atoms (Figure 5.1). Depending on the complexity of the model, they may include Fourier coefficients for displacement modulation (A_i^n and B_i^n for the sine and cosine Fourier coefficients of order n along the direction $i = x, y, z$); anharmonic ADPs of third (C_{ijk}) and fourth (D_{ijkl}) order; Fourier coefficients for the modulation of the ADPs (U_{ij}^{sn}, U_{ij}^{cn} for the sine and cosine Fourier coefficients of order n) as well as C_{ijk}^{sn} and C_{ijk}^{cn} (Table 5.2).

Structure refinements were performed with the computer program JANA2006 (Petricek et al., 2006). The model published by Aramburu et al. (2006) involves

displacement modulation parameters of orders 1, 2, 3 and 5. Refinement of these parameters against the Aramburu-data reproduced the published model within one standard uncertainty (σ) of all parameters.

Model A was created to resemble the published structure model as much as possible. It includes all Fourier coefficients up to fifth order for the displacement modulation, because the availability of fourth-order satellite reflections in the present data allows the refinement of the fourth-order Fourier coefficients of the displacement modulations. Refinements were initiated with the values of the published structure model as starting parameters. Values of the refined parameters are similar to those of the published structure model, with 12 out of 140 parameters having differences larger than 3σ and with a maximum difference of 5.2σ for A_x^3 of atom Rb1 (Table 5.3).

Model B is an extension of model A, where the first- and second-order Fourier coefficients of the modulation of the harmonic ADPs have been incorporated. Refinements with model A as starting values for the parameters gave a smooth convergence and lead to a considerable improvement of the fit to all orders of reflections (Table 5.4).

Refinement of model B was used to create the phased observed diffraction data for the MEM calculations (see Section 5.3.3). Analysis of the MEM-derived electron density map suggested that the next important feature is the modulation of the third-order anharmonic ADPs, while their average-structure values remain zero. Model C includes—in addition to the parameters of model B—the Fourier coefficients up to $n = 5$ for the modulation of the third-order anharmonic ADPs, C_{ijk}^n . This refinement suffered from large correlations between parameters. Therefore, a reduced model, model C_r , was defined, in which those Fourier coefficients C_{ijk}^n were set to zero that had values less than σ in the refinement of model C. This reduced the number of coefficients C_{ijk}^n from 244 to 132 (Table 5.2), while models C and C_r fit the data almost equally well (Table 5.4).

Difference-Fourier maps based on the observed structure factors and those calculated for a model indicate the improvement of the fit to the data for increasing complexity of the model (Figure 5.2 and Table 5.4). The difference Fourier map of model B compared to that of model C_r confirms the importance of modulated third-

order anharmonic ADPs, as it was derived on the basis of MEM-density maps. The difference-Fourier map of model C_r displays a structure around atom Rb2, which is independent of the phase of the modulation in first approximation. It has the signature of unmodulated fourth-order anharmonic ADPs, as they are missing in model C_r . The inclusion of fourth-order anharmonic ADPs for all atoms lead to highly nonphysical values of these parameters, that is, large negative values of the joint probability distribution function for the resulting model. Model D_r was then constructed to include fourth-order anharmonic ADPs for the atoms Rb1, Rb2 and Cl3 only. The improvement, as compared to model C_r , of the fit to the data, in particular to the main reflections, is apparent (Table 5.4). Refinements of the extinction coefficient lead to a negative value for this parameter, so it was fixed to zero.

The remaining discrepancies between calculated and observed structure factors can be attributed in part to the incompleteness of the model. As indicated above, introduction of more parameters leads to nonphysical values and high correlations between them, while these additional parameters would have been required for a full characterization of the modulation. A second reason for rather high final R values of the higher-order satellite reflections lies in the less than optimal accuracy of the present data due to a limited counting statistics. This interpretation becomes apparent, when the R values are considered for model D_r on the stronger reflections of the present data (reflections with $I > 5\sigma(I)$; column N^* in Table 5.4). In particular the partial R values of the higher-order satellite reflections are considerably lower than on the full data set (compare columns D_r^* and D_r in Table 5.4).

The fit of the models A, B, C, C_r and D_r to the Aramburu-data has been tested by refinement of the basic-structure parameters of each model against these data, while the modulation parameters and anharmonic ADPs were kept fixed to the values determined from the present data. The fit to the main reflections and first-order satellite reflections is reasonable, but it becomes worse on introduction of modulation parameters for the (an)harmonic ADPs (models B– D_r ; Table 5.5). On the other hand, the latter models lead to an improvement of the fit to the third- and fifth-order satellites of the Aramburu-data, but with R values that are considerably higher than those on the present data. These discrepancies can be attributed to

different qualities of the sample and—especially—different temperatures, which both will affect the shapes of the modulation functions and the contributions of modulated and anharmonic ADPs to it.

Therefore, independent refinements were performed against the Aramburu data, now varying all parameters, and resulting in models A' , B' , C' , C'_r and D'_r , which differ from the corresponding models A , B , C , C_r and D_r in the values of the parameters. The fit to the Aramburu data is dramatically improved in this way (see Supplementary Material), resulting in R values comparable to R values on the present data. Exception are the main reflections, which are much better fitted for the present data, indicating the higher accuracy of these data than the Aramburu data. Despite convergence of the refinements against the Aramburu data and the resulting low R values, the primed models suffer from high correlations between parameters and large standard uncertainties of them. For example, none of the modulation parameters for ADPs in model B' exceeds 6σ , which prevents a meaningful analysis of the modulation on the basis of model B' , as it has already been noticed by Aramburu et al. (2006). Standard uncertainties of modulation parameters and anharmonic ADPs are a multiple of the standard uncertainties of these parameters in the corresponding unprimed models (refinements against the present data). Therefore, we refrain from a further consideration of the primed models.

5.3.3 MEM calculations

Phased observed structure factors corrected for anomalous scattering and scaled to the scattering power of one unit cell were obtained according published procedures from the observed data and model B (Bagautdinov et al., 1998). These data were used for the calculation of a maximum-entropy-optimized generalized electron density in $(3 + 1)$ -dimensional superspace [MEM-density or $\rho_s^{MEM}(\mathbf{x}_s)$] with the computer program BAYMEM (van Smaalen et al., 2003). A uniform prior, the Cambridge algorithm and the weights of type F2 have been used (Li et al., 2010). The MEM calculation converged in 69 iterations (Table 5.1).

The $(3 + 1)$ -dimensional electron-density map has been analyzed with the computer program EDMA (van Smaalen et al., 2003). Physical-space sections of $\rho_s^{MEM}(\mathbf{x}_s)$

Table 5.6: Amplitudes of the displacement modulation functions of model D_r (relative coordinates multiplied by 10^5).

Atom	n	A_x^n	A_y^n	A_z^n	B_x^n	B_y^n	B_z^n
Rb1	1	1111(8)	0	0	-1100(9)	0	0
	2	0	-21(9)	94(6)	0	-171(8)	10(10)
	3	-175(16)	0	0	191(16)	0	0
	4	0	-81(16)	0(20)	0	103(15)	-120(20)
	5	101(9)	0	0	-94(9)	0	0
Rb2	1	1574(8)	0	0	-149(6)	0	0
	2	0	23(3)	-58(4)	0	10(3)	16(5)
	3	-148(15)	0	0	-49(8)	0	0
	4	0	-8(12)	40(18)	0	27(11)	-59(18)
	5	85(15)	0	0	29(10)	0	0
Zn	1	958(7)	0	0	308(6)	0	0
	2	0	-29(3)	-11(5)	0	-26(6)	82(5)
	3	-21(16)	0	0	-130(8)	0	0
	4	0	-42(13)	30(20)	0	21(16)	-40(20)
	5	-89(8)	0	0	12(8)	0	0
Cl1	1	3770(30)	0	0	580(30)	0	0
	2	0	-15(10)	-60(15)	0	-143(19)	10(20)
	3	-80(50)	0	0	-160(50)	0	0
	4	0	80(40)	-70(40)	0	-20(30)	20(40)
	5	170(70)	0	0	-60(70)	0	0
Cl2	1	770(30)	0	0	5100(40)	0	0
	2	0	-4(11)	-77(12)	0	-68(9)	40(19)
	3	-110(40)	0	0	-560(50)	0	0
	4	0	0(30)	20(30)	0	70(30)	10(40)
	5	90(80)	0	0	-70(80)	0	0
Cl3	1	501(15)	67(12)	-1022(10)	-1811(15)	2427(14)	1227(12)
	2	5(18)	-31(14)	100(15)	81(17)	-28(13)	12(17)
	3	-40(30)	-40(30)	-180(30)	184(14)	-335(18)	-10(30)
	4	20(20)	-60(20)	-50(30)	-120(20)	79(19)	100(30)
	5	-100(30)	40(40)	100(40)	-80(30)	190(30)	10(30)

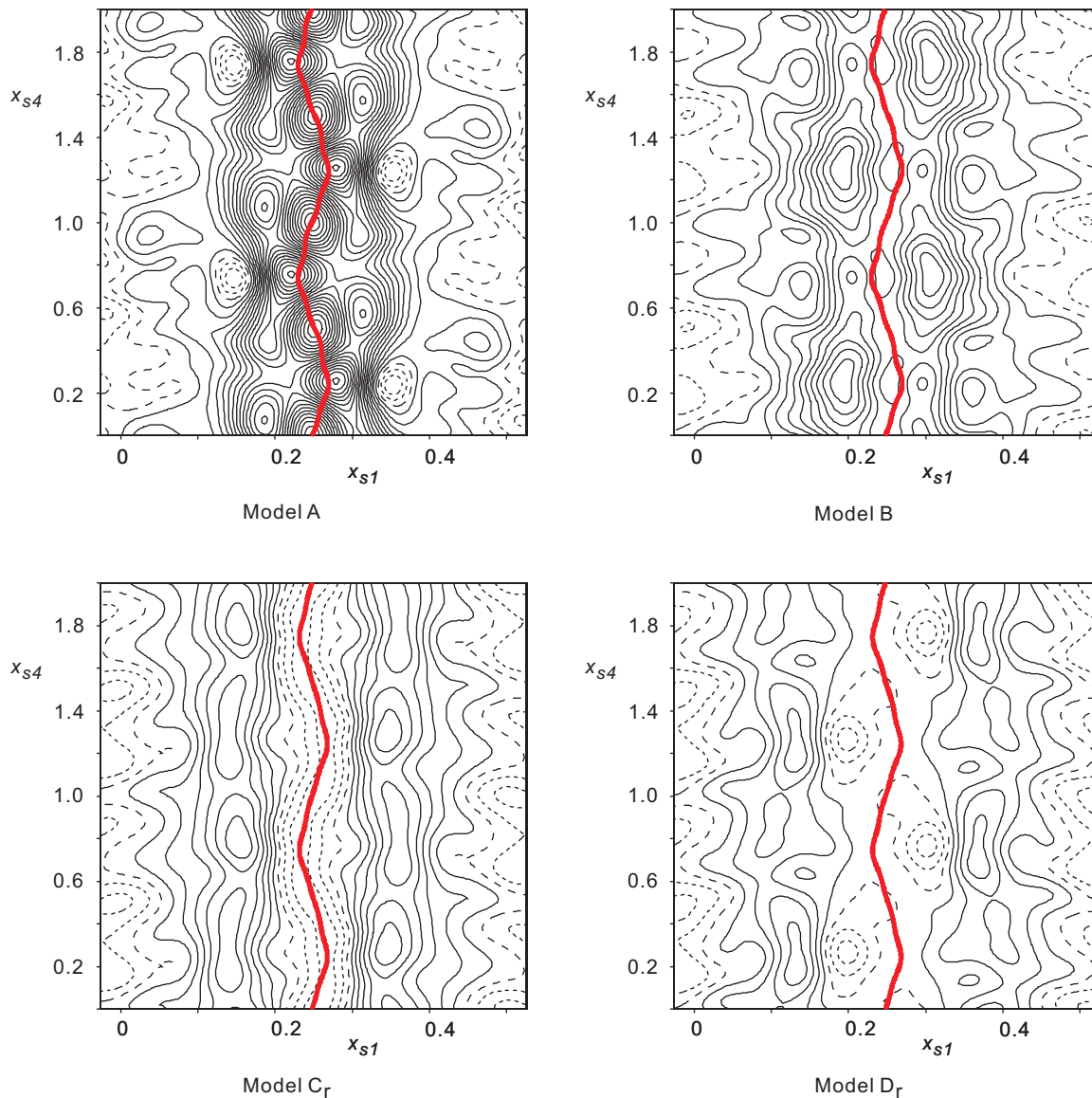


Figure 5.2: (x_{s1}, x_{s4}) -sections of difference-Fourier maps centered on atom Rb2 ($x_1 = 0.25$, $x_2 = 0.819$ and $x_3 = 0.487$) from different models. Solid lines stand for positive values, dashed lines for negative values, and long-dashed lines for the zero contour. The contour interval is $0.2 \text{ electrons } \text{\AA}^{-3}$. Maximum and minimum values over the map are $3.63/-0.57 \text{ electrons } \text{\AA}^{-3}$ for model A, $2.12/-0.41 \text{ electrons } \text{\AA}^{-3}$ for model B, $1.35/-0.52 \text{ electrons } \text{\AA}^{-3}$ for model C_r, $0.93/-0.51 \text{ electrons } \text{\AA}^{-3}$ for model D_r. The Thick red lines denote the modulated position of atom Rb2.

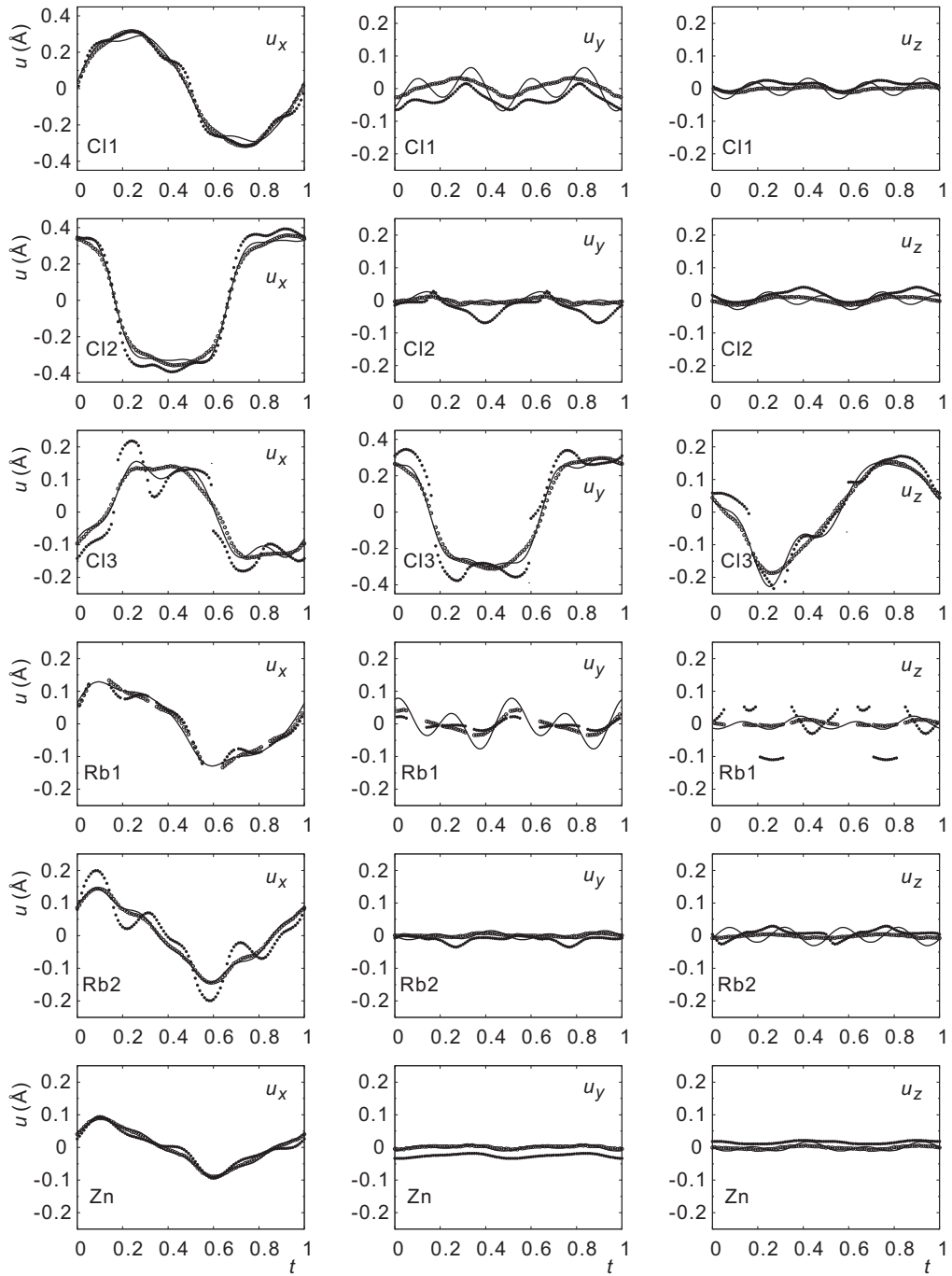


Figure 5.3: Modulation functions of the crystallographically independent atoms of Rb_2ZnCl_4 . Displacements along x , y and z are given in Å. Open circles are the center of charge and filled circles are the maxima of the MEM-electron density. Lines represent the modulation functions of model A.

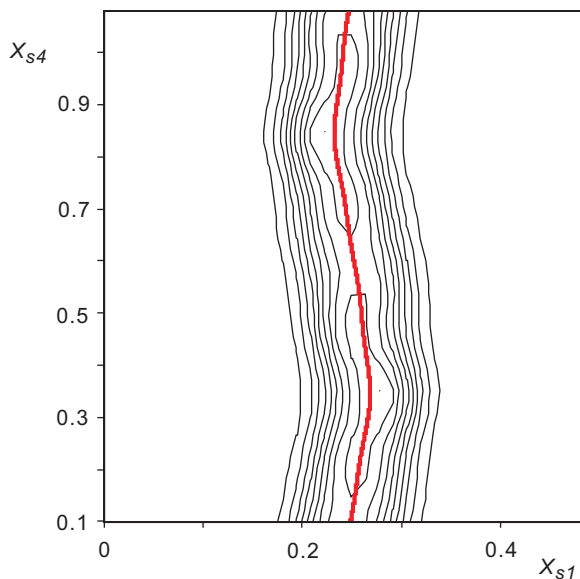


Figure 5.4: (x_{s1}, x_{s4}) -Section of the generalized electron density $\rho_s^{MEM}(\mathbf{x}_s)$ at the position of Rb2 ($x_1 = 0.25$, $x_2 = 0.819$ and $x_3 = 0.487$). The contour interval is 10% of the maximum of electron density of $175.1 \text{ electrons } \text{\AA}^{-3}$. The thick (red) line is the modulated position of atom Rb2 from model D_r .

have been obtained for one hundred equally-spaced t values within one period along the fourth axis, *i.e.* for $0 \leq t < 1$. Atoms in the crystal correspond to local maxima in the physical-space sections of the generalized electron density. The positions of the local maxima in each t -section can be identified with atomic positions. The position of each local maximum as a function of t then provides the modulated position of an atom. Alternatively, the center-of-charge has been determined for the atomic basins surrounding each local maximum. The dependence on t of the positions of the center-of-charge provide an alternative measure for the atomic positions. Modulation functions have been extracted from $\rho_s^{MEM}(\mathbf{x}_s)$ by taking the difference between the modulated atomic position and the basic-structure position as obtained from model B (Figure 5.3).

Two-dimensional sections of $\rho_s^{MEM}(\mathbf{x}_s)$ have been visualized by the plotting option of the computer program JANA2006 (Petricek et al., 2006). The (x_{s1}, x_{s4}) -section centered on atom Rb2 clearly shows the modulated position of this atom (Figure 5.4).

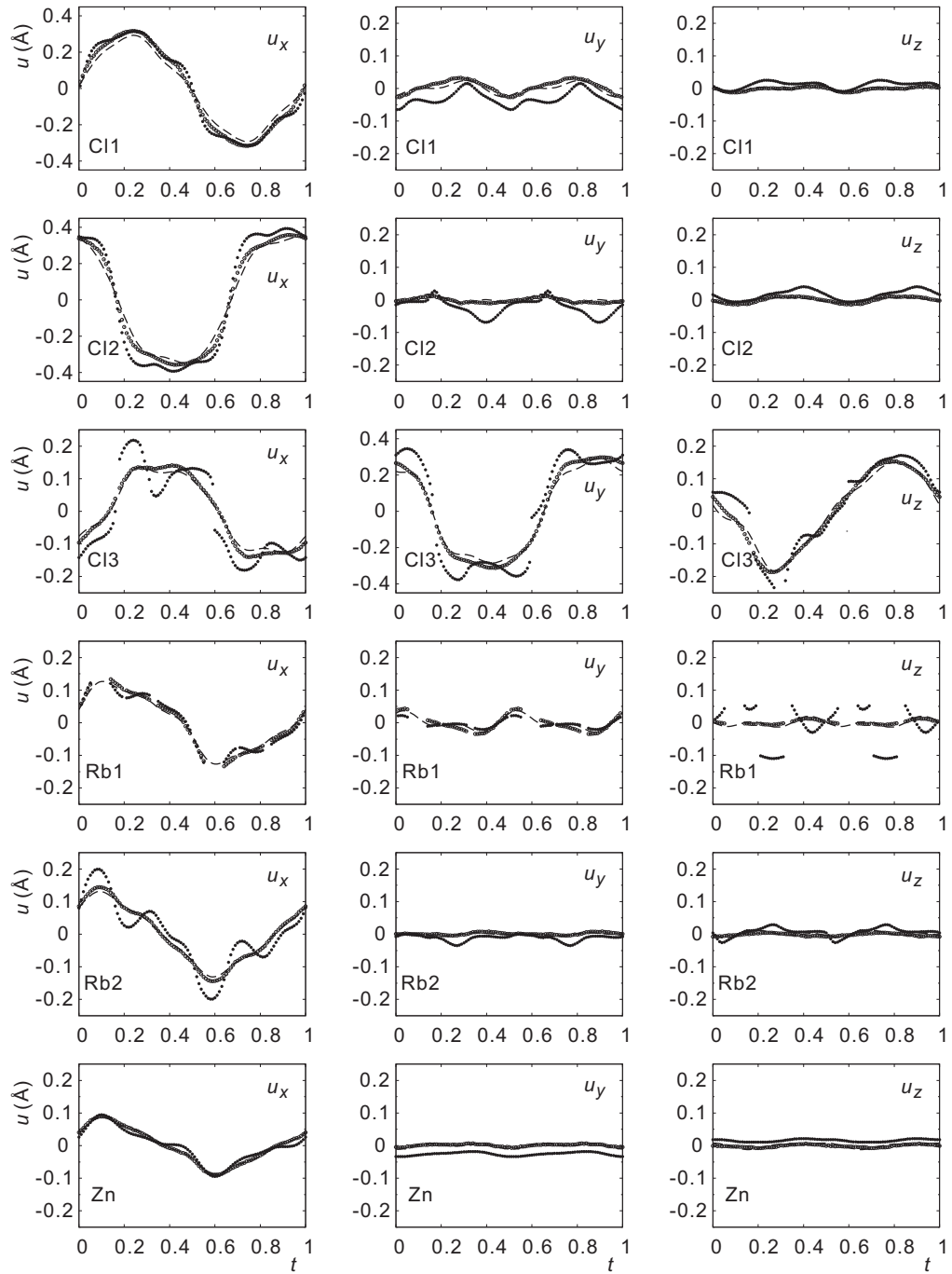


Figure 5.5: Modulation functions of the crystallographically independent atoms of Rb_2ZnCl_4 . Displacements along x , y and z are given in Å. Open circles are the center of charge and filled circles are the maxima of the MEM-electron density. Dashed lines represent the modulation functions of model D_r .

5.4 Discussion

5.4.1 Nature of the modulation

The incommensurate modulation of Rb_2ZnCl_4 at a temperature of $T = 196$ K, close to the lock-in transition at $T_{\text{lock-in}} = 192$ K, has been determined to comprise of atomic displacement modulation functions that contain contributions of Fourier coefficients up to fifth order. This finding is in agreement with previous studies on this compound (Aramburu et al., 2006). Modulations of the ADPs are found to be an intrinsic part of the incommensurate crystal structure. That is, the harmonic ADPs are modulated with up to second-order Fourier coefficients and the third-order anharmonic ADPs are modulated with Fourier coefficients up to fifth order, while the basic-structure components of the third-order anharmonic ADPs are zero.

The finding of modulated atomic displacement parameters agrees well with previous studies, like on incommensurately modulated Na_2CO_3 (Dusek et al., 2003), and the composite crystals $[\text{LaS}]_{1.14}[\text{NbS}_2]$ and $[\text{SrO}]_2[\text{CrO}_2]_{1.85}$ (Jobst and van Smaalen, 2002; Castillo-Martínez et al., 2008). Modulated ADPs have also been found necessary in cases where only first-order satellite reflections were available, like $\text{La}_2\text{C}_{1.7}$, $\text{Na}_2\text{Si}_3\text{O}_7$ and Pb_2NiVO_6 (Dusek et al., 2000; Kruger et al., 2006; Roussel et al., 2009).

The necessity of modulation functions for third-order anharmonic ADPs has been revealed by our previous studies by the MEM on NH_4BeF_4 (Palatinus et al., 2004) and $\text{Cr}_2\text{P}_2\text{O}_7$ (Li et al., 2010). Many incommensurate crystal structures have been published, where R values are higher than they should have been for the perfect structure model. It can thus be speculated that the fit to diffraction data might be improved for many compounds by the inclusion of modulated ADPs and modulated third-order anharmonic ADPs. On the other hand, correlations between modulation parameters—as shown here for Rb_2ZnCl_4 —might prevent their determination by structure refinements. This problem especially exists for high-order Fourier coefficients of modulation functions. Meaningful values are almost always limited to coefficients of orders equal and less than the maximum order of observed satellite reflections.

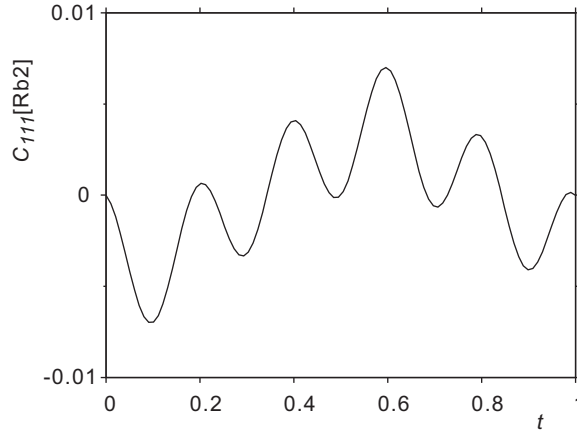


Figure 5.6: Value in model D_r of the component C_{111} of third-order anharmonic ADPs of atom Rb2 as a function of t . Minimum and maximum values are located at $t = \sim 0.1$ and ~ 0.6 , respectively.

It is suggested that modulations of ADPs are an intrinsic part of modulations in incommensurate crystals in general. Their presence can be rationalized by the fact that any displacive modulation defines a modulation of the environments of the atoms. Different environments require different ADPs, which can be achieved by a modulation of the ADPs. It is important to include at least up to second order Fourier coefficients (Perez-Mato et al., 1991).

A displacement modulation of an atom creates a tightening of its environment in the direction in which this atom is displaced. Because the modulation always involves displacements out of the average position into both the positive and negative directions, this general feature of modulations explains the presence of modulated third-order anharmonic ADPs, while their average values are zero. The correlation between displacement modulation and modulated C_{ijk} is apparent from the values found for model D_r of Rb_2ZnCl_4 . Both the displacement modulation and the modulated C_{ijk} have their most important nonzero components along the \mathbf{a} axis for all five independent atoms on the mirror plane (Table 5.6 and supplementary material). Atom Cl3—not on the mirror plane—has contributions to its modulation for the other directions too, which again affects both the displacement modulation and modulated third-order anharmonic ADPs. Although not perfectly matched, positive displacements along \mathbf{a} (Figure 5.5) of atom Rb2 match negative values of C_{111}

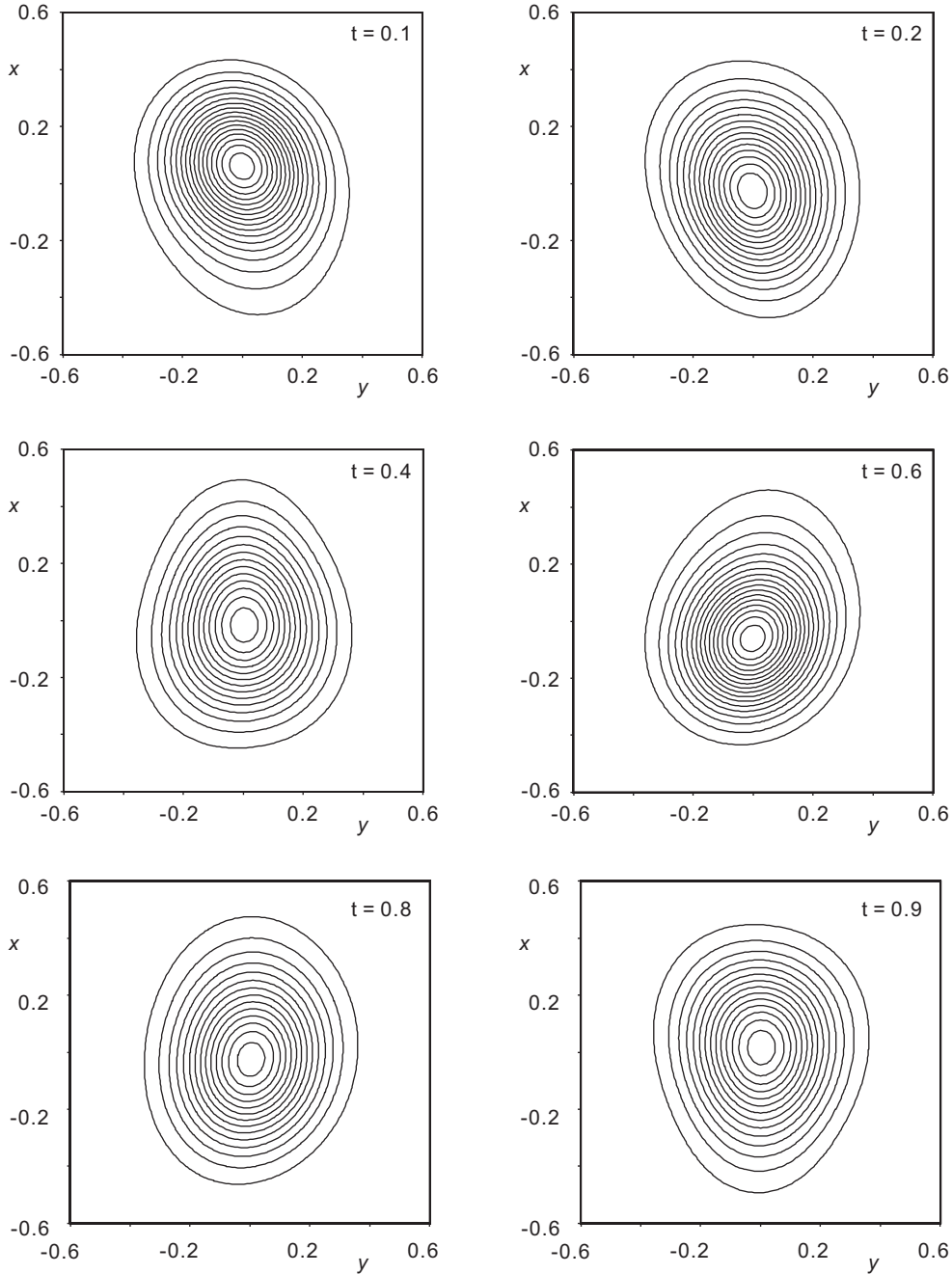


Figure 5.7: The joint probability distribution function at the site of Rb2 for selected t values for model D_r , but obtained with U_{ij} and C_{ijk} only. Contour interval is 1 electron \AA^{-3} with a maximum density of 17.7 electron \AA^{-3} .

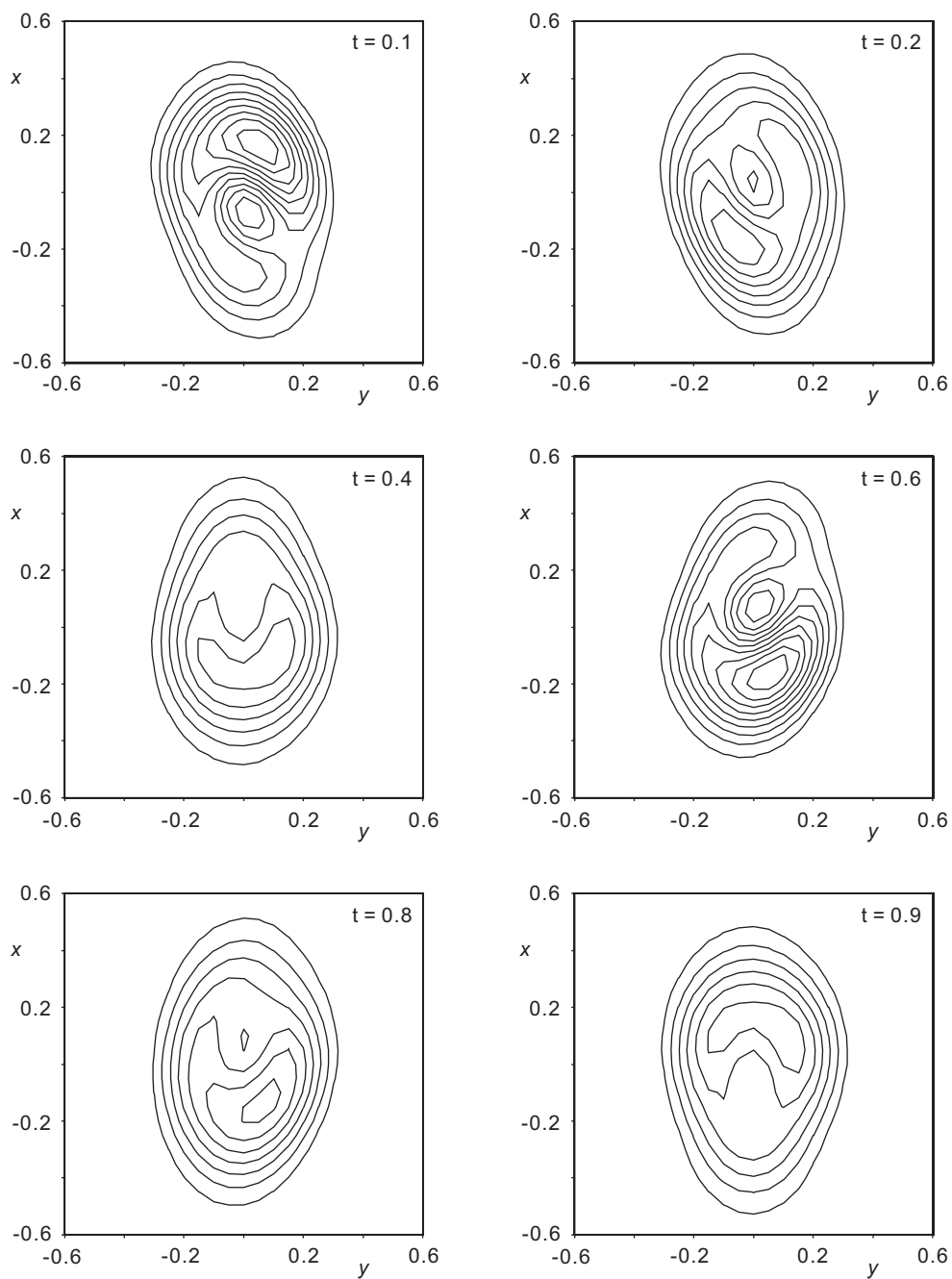


Figure 5.8: The joint probability distribution function at the site of Rb2 for selected t values for model D_r . Contour interval is 1 electron \AA^{-3} . Over the selected map region the minimum density is -0.66 electron \AA^{-3} and the maximum density is 9.8 electron \AA^{-3} .

(Figure 5.6), which implies a decreased probability (Figures. 5.7 and 5.8) for the presence of an atom in the direction of the tighter environment.

The trace of the center-of-charge for each atom in the MEM density indicates smooth modulations, whereas the trace of the local maximum of the density varies around the position defined by the center-of-charge for each atom (Figure 5.3). We take this variation as evidence for the presence of modulated third-order anharmonic ADPs. Similarly, several of the components of the modulation functions in model A exhibit variations (ripples) according to higher-order Fourier coefficients, while the same functions appear smooth in model D_r (Figure 5.5). (The largest effect is visible for the components $u_y[Cl_1]$, $u_z[Cl_3]$ and $u_y[Rb_1]$.) These smoother functions seem more plausible and they match the trace of the center-of-charge very well. Both refinements (model D_r vs model A) and the MEM thus provide evidence for modulated third-order anharmonic ADPs. Least of all, the reduction of R values on increasing complexity of the structure model provides strong evidence for modulated harmonic ADPs and modulated third-order anharmonic ADPs (Table 5.4).

As mentioned above, structure refinements without (model A) and with modulation functions for ADPs (models B– D_r) result in significantly different functions for the displacive modulation. The inclusion of modulated functions for ADPs thus appears necessary for achieving an accurate description of the displacive modulation, with concomitant implications for the interpretation of the modulation (Section 5.4.2). Alternatively, the center-of-charge of each atom in the MEM density also provides a good description of the displacement modulation functions.

Comparison of the two approaches—MEM analysis and structure refinements—shows the different limitations of either method. The MEM-density gives evidence for the modulations of the ADPs as well as the presence of anharmonic ADPs. However, the finite size of the pixels in the MEM density (here: 0.1 Å) limits the accuracy of the atomic positions to about 0.01 Å (van Smaalen et al., 2003), while atoms on special positions might sometimes lead to more accurate values of the positions. An error of up to 0.01 Å is not small, if modulations are considered with amplitudes significantly below 0.1 Å. On the other hand, structure refinements readily lead to large dependencies between parameters, such that Fourier components of orders $n > 5$ cannot be determined. Furthermore, a full *ab-initio* determination appeared

impossible for the third-order and fourth-order anharmonic ADPs, and we had to resort to a method of selecting relevant parameters (compare models C, C_r and D_r and the discussion in Section 5.3.2).

5.4.2 Relation to the soliton model

Aramburu et al. (2006) have shown that a soliton model for the modulation leads to displacement modulation functions with Fourier components of first and fifth (and higher) order. They introduced a measure, n_s , for the soliton density, which actually describes the shape of the modulation functions with $n_s = 1$ for a sinusoidal shape and $n_s = 0$ for a block wave. The phase of the fifth-order Fourier coefficient depends on the phase of the first-order Fourier coefficient by a simple relation and it is independent from the soliton density. The ratio between amplitudes of fifth- and first-order Fourier coefficients should be the same for all atoms, while its value is a measure for the soliton density. Aramburu et al. (2006) have found these relations to be approximately valid for their structure model for Rb_2ZnCl_4 , and they proposed that the modulation of Rb_2ZnCl_4 at the temperature of their experiment has a soliton density of $n_s = 0.4$.

Here we have shown that significant differences exist for the displacement modulation functions in cases of a pure displacive modulation model (model A) and a model including modulated (an)harmonic ADPs (model D_r). Both models appear to be at variance with the soliton model, as follows from the ratio of amplitudes of fifth- and first-order Fourier coefficients and from the phases of the fifth-order Fourier coefficients (Figures. 5.9 and 5.10). A critical analysis of the present structure models and the structure model by Aramburu et al. (2006) shows that standard uncertainties on the fifth-order Fourier coefficients are so large, that the agreement with the soliton model as observed by Aramburu et al. (2006) should be considered fortuitous. In view of the values of the standard uncertainties, consideration of the first- and fifth-order Fourier coefficients of the displacement modulation functions by themselves does not make a clear case against or in favor of the soliton model.

Another feature of the modulation pleading against the soliton model is the presence of third-order Fourier coefficients of larger magnitude than the fifth-order

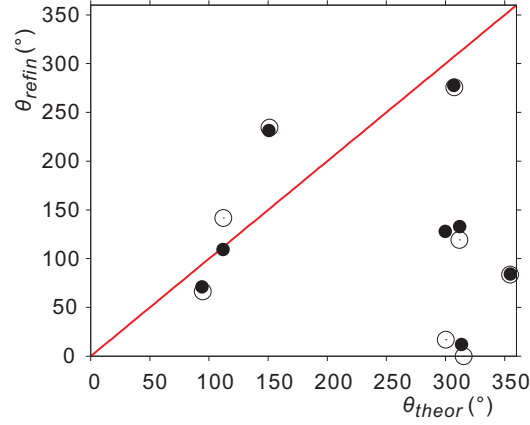


Figure 5.9: Comparison of experimental and calculated values of the phases of the fifth-order Fourier coefficients of the displacive modulation functions. θ_{refin} is obtained from the refined fifth-order coefficients of model A (open circles) and model D (full circles). θ_{theor} is calculated from the phases of the refined first-order Fourier coefficients of the same models according to the soliton model Aramburu et al. (2006). The soliton model would require all points to lie on the straight line of slope one.

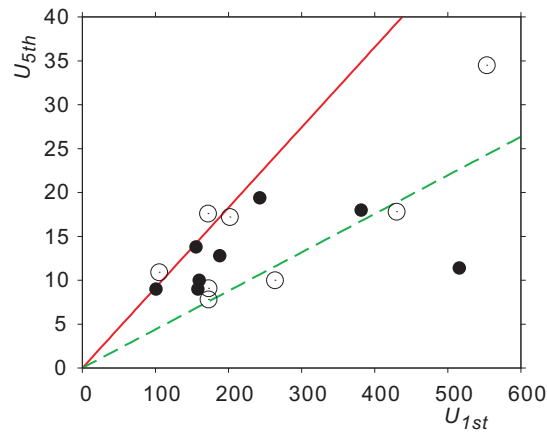


Figure 5.10: Comparison of the amplitudes (multiplied by 10^4) of the fifth-order (U_{5th}) and first-order (U_{1st}) Fourier coefficients of the modulation functions of model A (open circles) and model D_r (full circles). The soliton model requires all points to lie on a straight line with a slope that defines the soliton density. The solid line is calculated for a soliton density of 0.4 Aramburu et al. (2006); the dashed line has been obtained by a least-squares fit to the values of model D_r and it represents a soliton density of 0.63.

coefficients, and the presence of second- and fourth-order Fourier coefficients of similar magnitudes as the fifth-order coefficient (Table 5.6). Aramburu et al. (2006) interpreted the third-order Fourier coefficient as a secondary mode. However, the distortion towards the supposed soliton-shaped wave would be smaller than these secondary modes, a situation which seems unlikely.

An important part of the modulation is modulated harmonic ADPs and modulated third-order anharmonic ADPs. These modulations have not been incorporated into the soliton model considered by Aramburu et al. (2006). The relation of these modulation functions to a possible soliton property of the modulation wave will require further theoretical analysis that is beyond the scope of the present work.

5.4.3 Origin of the modulation

The origin of the modulations in Rb_2ZnCl_4 and in A_2BX_4 -type compounds in general lies in the incompatibility between the observed orthorhombic packing of ZnCl_4 and Rb ions and the nearly tetrahedral symmetry of the ZnCl_4 complex ions. This incompatibility results in one short distance between the 11-coordinated A atom (Rb1 in the present models) and an X atom (Cl1 in the present models) in the same mirror plane. The bond strength of this short bond in the unmodulated high-temperature structure has been taken as measure for the propensity of the compound to form modulated structures at low temperatures (Fabry and Perez-Mato, 1994).

Analysis of the interatomic distances of model D_r shows that they are in agreement with previous studies on similar compounds (Frieze et al., 2000), and that they support the interpretation given by Fabry and Perez-Mato (1994) (See t -plots of distances and bond angles in the Supplementary Material). The present model gives displacement modulations of Rb1 and Cl1 that are in-phase with each other (Figure 5.5). Consequently, the very short Rb1–Cl1 distance hardly varies with the phase t of the modulation. Instead, the strain of this contact is resolved by the modulated third-order anharmonic ADPs.

5.5 Conclusions

A combination of structure refinements, interpretation of difference-Fourier maps and the analysis of the superspace MEM-density has been used to characterize the incommensurate modulation of Rb_2ZnCl_4 at a temperature of $T = 196$ K, close to the lock-in transition at $T_{\text{lock-in}} = 192$ K. Basic characteristics of the modulation are a displacement modulation that contains contributions of Fourier coefficients up to fifth order. A modulation of the ADPs is found to be an intrinsic part of the modulation. That is, the harmonic ADPs are modulated with up to second-order Fourier coefficients and the third-order anharmonic ADPs are modulated with Fourier coefficients up to fifth order, while the basic-structure or average components of the third-order anharmonic ADPs are zero.

Model D_r , which includes modulated ADPs and modulated third-order anharmonic ADPs, provides different values for the parameters of the displacement modulation than model A, which lacks any modulation of ADPs. Modulations of ADPs thus is essential for the correct description of the displacement modulation functions.

The MEM density gives an excellent description of the displacement modulations of the atoms by means of the t -dependencies of the traces of the centers-of-charge of the atoms. These traces coincide with the displacement modulation functions of the atoms in model D_r , providing further support for the necessity of modulated ADPs. Modulations of the ADPs and anharmonic ADPs are visible in the MEM density as variations of the distributions of the density about their average value, as it is exemplified by the traces of the local maxima of the MEM density around the positions of the atoms. A quantitative interpretation of the MEM density is made difficult by the finite resolution of this map, which limits the accuracy of positions to about 0.01 \AA .

Structure refinements may lead to a quantitative description of the modulation, but the introduction of the required model parameters readily leads to correlated parameters. Nevertheless, with the extensive data set available in the present study, we have been able to obtain significant values for higher-order Fourier coefficients of the displacive modulation functions and for modulated parameters of the harmonic ADPs and the third-order anharmonic ADPs.

The results suggest that modulated harmonic ADPs and modulated third-order anharmonic ADPs form an intrinsic part—however small—of incommensurately modulated structures.

For Rb_2ZnCl_4 we could show that the modulation cannot be interpreted as a soliton wave, thus contradicting previous proposals (Aramburu et al., 2006).

Acknowledgements

The single crystal was grown by Alfred Suttner at the Laboratory of Crystallography in Bayreuth. We thank Vaclav Petricek, Michal Dusek and Lukas Palatinus (Praha) for help with JANA2006. We are grateful to I. Aramburu for providing a copy of their diffraction data of Rb_2ZnCl_4 . Financial support was obtained from the German Science Foundation (DFG).

Chapter 6

Incommensurately modulated $\text{Cr}_2\text{P}_2\text{O}_7$

6.1 Abstract

The Maximum Entropy Method (MEM) has been used to determine the electron density in superspace of incommensurately modulated chromium pyrophosphate from X-ray diffraction data measured by Palatinus et al. (2006). Chromium pyrophosphate, $\text{Cr}_2\text{P}_2\text{O}_7$ contains ordered regions (83% of the volume) and regions with disorder. Analysis of the MEM density has allowed to determine the displacive modulation functions within the ordered regions. The disordered regions can be described as the alternate occupation of two conformations of the pyrophosphate group and two positions of the chromium atom, with occupational probabilities that depend continuously on the phase of the modulation t . A structure model based on the interpretation of the MEM density provides a fit to the diffraction data of the same quality as the model given by Palatinus et al. (2006). The failure of finding a model that better fits the data is attributed to the intrinsic inaccuracy of ~ 0.01 Å for positions derived from the MEM and to the difficulties in constructing an appropriate model for the anharmonic ADPs and their modulation functions from electron densities.

6.2 Introduction

One of the applications of the Maximum Entropy Method (MEM) in crystallography is the reconstruction of the electron density from phased structure factors (Gilmore, 1996). Analysis of the MEM electron density can provide a lot of information about disorder (Dinnebier et al., 1999; Wang et al., 2001), anharmonic thermal motion (Kumazawa et al., 1995; Bagautdinov et al., 1998), and chemical bonding (Sakata and Sato, 1990; Takata, 2008; van Smaalen and Netzel, 2009). For aperiodic crystals the MEM has been used for the determination of the shapes of modulation functions of modulated crystals or for the determination of the occupational domains of quasicrystals (Yamamoto et al., 1996; Palatinus and van Smaalen, 2004; van Smaalen and Li, 2009).

The structures of incommensurately modulated crystals and composite crystals can be described by a periodic basic structure¹ combined with modulation functions for each of the independent atoms in the unit cell of the basic structure (van Smaalen, 2007; Janssen et al., 2007). Structure models then incorporate for each independent atom three basic-structure coordinates, atomic displacement parameters (ADP) and—in principle—an infinite number of parameters defining the modulation functions. Since structure refinements can determine a finite number of parameters at best, modulation functions are usually described by truncated Fourier series. Often only the first harmonic or up to second harmonics can be determined, while a larger number of parameters cannot be refined due to interdependencies among them. Sometimes it appears appropriate to employ block waves or sawtooth-shaped functions as modulation functions. However, in all cases the outcome of structure refinements is restricted by the choice of parameters for the modulation functions. The result may differ from the true functions and it may not reflect the information content of the diffraction data.

The MEM has been proposed as a model-independent tool to obtain the most probable generalized electron density in the unit cell of superspace of aperiodic crystals. Analysis of the superspace density then provides a model-independent estimate of the modulation functions (van Smaalen et al., 2003; van Smaalen, 2007). Several

¹Composite crystals require two or more basic periods

Table 6.1: Basic structural information as obtained The criterion for observed reflections is $I > 3\sigma(I)$.

Chemical formula	$\text{Cr}_2\text{P}_2\text{O}_7$
Superspace group	$C2/m(\sigma_1 0 \sigma_3)\bar{1}s$
Lattice parameters, a (Å)	7.0192 (5)
b (Å)	8.4063 (6)
c (Å)	4.6264 (3)
β (deg)	108.6111 (64)
Modulation wavevector	$(-0.361(1), 0, 0.471(1))$
$(\sin(\theta)/\lambda)_{max}$ (Å ⁻¹)	0.62
No of reflections (obs/all)	1433/2409
No of main reflections (obs/all)	278/283
No of first-order satellites (obs/all)	455/495
No of second-order satellites (obs/all)	421/569
No of third-order satellites (obs/all)	183/495
No of fourth-order satellites (obs/all)	96/567

successful applications of this principle have been published (Palatinus and van Smaalen, 2004; McMahon et al., 2007).

Chromium pyrophosphate $\text{Cr}_2\text{P}_2\text{O}_7$ is a member of the thortveitite family of compounds (Glaum et al., 1991). The thortveitite structure type is stable at high temperatures, while it defines the basic structure of the incommensurately modulated phase at room temperature (Table 6.1). The modulation becomes commensurate below $T_c = 285$ K. Structure refinements of $\text{Cr}_2\text{P}_2\text{O}_7$ have been performed by Palatinus et al. (2006), employing combination of harmonic, block-wave and saw-tooth functions for the modulation functions. The analysis by Palatinus et al. (2006) showed small regions of large variations of the modulation functions that could not properly be described by a model. Here, we present the results of an analysis by the MEM of the modulations in $\text{Cr}_2\text{P}_2\text{O}_7$ based on the X-ray diffraction data published by Palatinus et al. (2006). Although the structure model based on the MEM gives only a slightly better fit to the diffraction data, a direct analysis of the MEM-density clearly reveals the way the structure resolves internal strain in the transition regions.

The basic structure of $\text{Cr}_2\text{P}_2\text{O}_7$ is formed by layers of edge-sharing, distorted CrO_6 octahedra. Gaps in these layers are bridged by P_2O_7 pyrophosphate groups that share three of their oxygen atoms with a layer below and three other oxygen

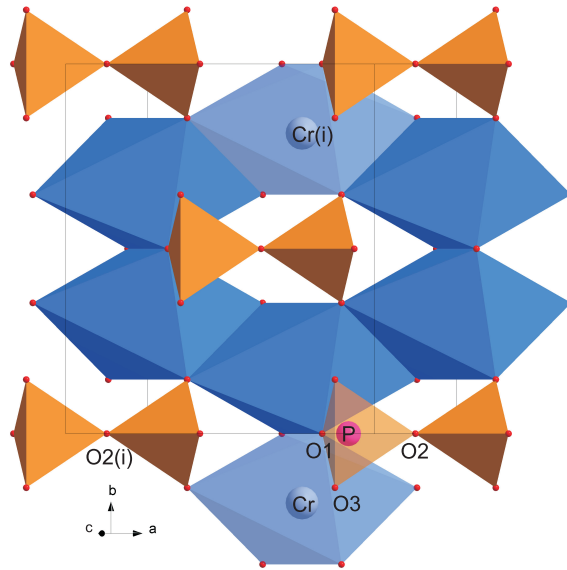


Figure 6.1: Basic structure of $\text{Cr}_2\text{P}_2\text{O}_7$. $\text{Cr}(i)$ and $\text{O2}(i)$ are related by lattice translations to Cr and O2 , respectively.

atoms with a layer above; the bridging oxygen atom is confined to the P_2O_7 group (Figure 6.1). The most probable origin for the incommensurability is that a fully relaxed (stretched) pyrophosphate group is larger than the gaps in the Chromium oxide layers. The room-temperature crystal structure with the periodicity of the CrO_3 layers must thus contain the pyrophosphate group in some unfavorable conformation, which is relieved at low temperatures by forming an incommensurately modulated structure. Other contributions to the incommensurability could come from Jahn–Teller distortions of the CrO_6 octahedral groups (Palatinus et al., 2006).

6.3 The maximum entropy method

The generalized electron density $\rho_s(\mathbf{x}_s)$ in $(3 + 1)$ -dimensional superspace is discretized on a grid of $N_{pix} = N_1 \times N_2 \times N_3 \times N_4$ pixels over the superspace unit cell.

Then the entropy is defined as (van Smaalen et al., 2003)

$$S = - \sum_{k=1}^{N_{pix}} (\rho_k \log[\rho_k/\rho_k^{prior}] - \rho_k + \rho_k^{prior}) \quad (6.1)$$

where $\rho_k = \rho_s(\mathbf{x}_{sk})$ is the electron density at the k^{th} grid point and ρ_k^{prior} is the corresponding value of the reference density or PRIOR. The MEM defines the optimal electron density as the electron density $\{\rho_k\}$ which maximizes the entropy S (Equation 6.1) subject to several constraints. The first constraint is the normalization of $\{\rho_k\}$ and $\{\rho_k^{prior}\}$,

$$\frac{V}{N_{pix}} \sum_{k=1}^{N_{pix}} \rho_k = N_e \quad (6.2)$$

where N_e is the number of electrons in the unit cell and V is its volume. Diffraction data are incorporated in the form of the so-called F constraint, $C_{F^2} = 0$, with Sakata and Sato (1990)

$$C_{F^2} = -1 + \frac{1}{N_F} \sum_{i=1}^{N_F} w_i \left(\frac{|F_{obs}(\mathbf{H}_i) - F_{MEM}(\mathbf{H}_i)|}{\sigma_i} \right)^2. \quad (6.3)$$

The sum runs over all independent structure factors N_F in the data set. $F_{obs}(\mathbf{H}_i)$ is the phased observed structure factor of the reflection with scattering vector \mathbf{H}_i , and σ_i is the standard uncertainty of $|F_{obs}(\mathbf{H}_i)|$. $F_{MEM}(\mathbf{H}_i)$ is obtained by (3+1)-dimensional Fourier transform of the trial density $\{\rho_k\}$. The standard version of the MEM employs weights $w_i = 1$. The F -constraint then represents χ^2 of the data with an expectation value of one. This value is achieved at convergence where $C_{F^2} = 0$.

For uncorrelated standard uncertainties σ_i one expects at convergence a normalized Gaussian distribution of the residuals,

$$\frac{\Delta F(\mathbf{H}_i)}{\sigma_i} = \frac{F_{obs}(\mathbf{H}_i) - F_{MEM}(\mathbf{H}_i)}{\sigma_i}. \quad (6.4)$$

It has been shown that the MEM with $w_i = 1$ leads to distributions far from Gaussian in most cases. This feature is responsible for a converged density $\{\rho_k\}$ that is far from the optimum density $\{\rho_k^{MEM}\}$ (de Vries et al., 1994; Palatinus and van Smaalen,

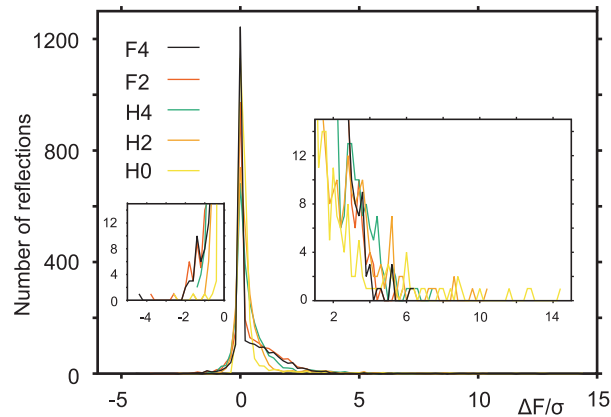


Figure 6.2: Distribution of residuals (Equation 6.4) at convergence of the MEM for weights H0, H2, H4, F2 and F4. The inset shows an expanded view.

2002).

Several weighting schemes have been proposed, which should guide the iterative MEM procedure towards the optimum density with a Gaussian distribution of residuals (Equation 6.4). A good choice for periodic crystals is weights that vary according to an inverse power of the length of the scattering vector,

$$w_i = \frac{1}{|\mathbf{H}_i|^n} \left(\frac{1}{N_F} \sum_{i=1}^{N_F} \frac{1}{|\mathbf{H}_i|^n} \right)^{-1} \quad (6.5)$$

with n a positive integer. These static weights are denoted by Hn . Optimal results have been obtained for weights H4 (de Vries et al., 1994; Hofmann et al., 2007).

An empirical justification for weights Hn is provided by the observation that a few low-order strong reflections attain large residuals. In this case $C_{F^2} = 0$ then implies that the other reflections will have too small values for their residuals (de Vries et al., 1994). Strong reflections of periodic crystals have short scattering vectors and weights Hn define larger weights for exactly these reflections. In case of incommensurately modulated crystals problematic reflections are again the strong reflections with short scattering vectors. However, reflections with short scattering vectors include both main reflections and satellite reflections.

The latter are generally weak and they inadvertently obtain large weights, if

Table 6.2: Comparison of MEM calculations with different weights. Given are the R values (%) at convergence as well as the number of reflections with $\Delta F/\sigma \geq 6$ and the value of $(\Delta F/\sigma)_{max}$.

	H0	H2	H4	F2	F4
$R_F(\text{all})$	3.92	4.69	4.50	2.74	2.45
$wR_{F^2}(\text{all})$	3.71	3.72	3.71	3.73	3.73
$\Delta F/\sigma \geq 6$	17	9	6	0	2
$(\Delta F/\sigma)_{max}$	14.48	10.48	7.36	5.80	6.37

weights of the type Hn are employed. Presently, we have found that weights H2 and H4 do not lead to optimal MEM densities, as it is indicated by the distributions of residuals (Table 6.2 and Figure 6.2) and by the mismatch between modulation functions derived from the MEM densities and those of the model (Figure 6.3).

Weights that emphasize the strong reflections can alternatively be chosen as weights proportional to some power of the structure factor amplitude (de Vries et al., 1994)

$$w_i = |F_{obs}(\mathbf{H}_i)|^n \left(\frac{1}{N_F} \sum_{i=1}^{N_F} |F_{obs}(\mathbf{H}_i)|^n \right)^{-1} \quad (6.6)$$

These weights are denoted by F_n . Here we have found that an optimal result is obtained for weights F2. Although the distribution of residuals is not Gaussian for F2, this choice of weights gave the best performance for removal of the problem of very large residuals for a few reflections (Table 6.2). Another indication for the better performance of weights F2 is that they lead to a lower R_F value than weights Hn (Table 6.2).

Weights F2 are not necessarily the optimal choice for incommensurate crystals. One can envisage that other weighting schemes might work better or that different weighting schemes will appear optimal for different compounds. Nevertheless, weights F2 appear to give excellent results for $\text{Cr}_2\text{P}_2\text{O}_7$ (Figure 6.3). Therefore they have been used for the present analysis.

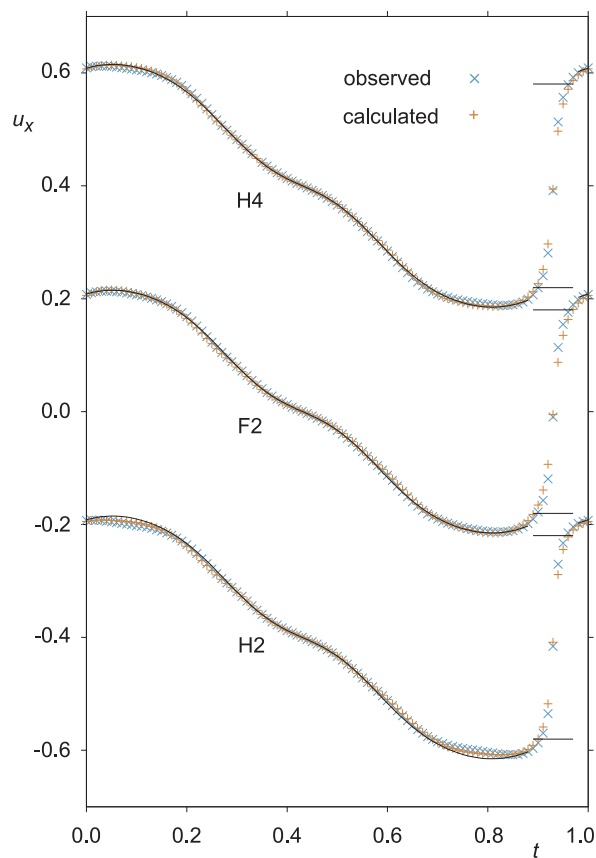


Figure 6.3: Modulation function u_x of Cr as obtained from MEM densities computed against observed data (\times) and against F_{cal} as "data" ($+$). Values obtained with weights H2, F2 and H4 are plotted with offsets of -0.4 , 0 and 0.4 \AA , respectively. The modulation function of refined model B is given as a solid line and reproduced at each offset value.

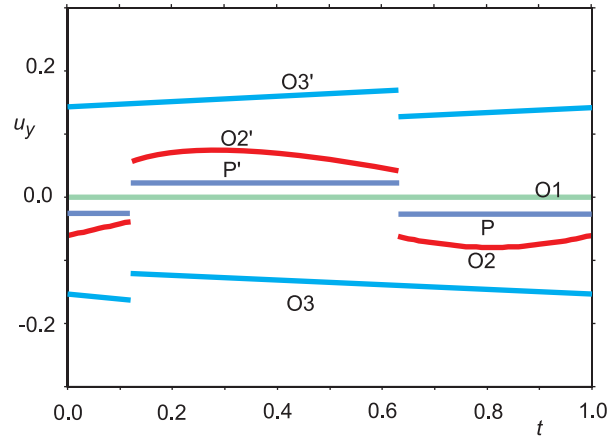


Figure 6.4: Schematic representation of the modulation functions in model A. The component u_y is shown as a function of t . Discontinuities are present at $t = 0.13$ and at $t = 0.63$. Primed atoms are related to unprimed atoms by the symmetry operator $(x_1, -x_2, x_3, \frac{1}{2} + x_4)$.

6.4 Experimental

6.4.1 Structure refinements

The present work is based on the X-ray diffraction data by Palatinus et al. (2006). Properties of the data of particular relevance for the MEM are summarized in Table 6.1. Palatinus et al. (2006) present several models for the structure of incommensurately modulated $\text{Cr}_2\text{P}_2\text{O}_7$. Their model A is based on displacive modulation functions that are combinations of saw-tooth, block-wave and harmonic functions. The atomic displacement parameters (ADPs) are modulated by harmonic functions in this model. Model A is characterized by discontinuities in the modulation functions at two values of t (Figure 6.4). Model B is proposed as their best model by Palatinus et al. (2006). It differs from model A as it contains regions of disordered structure around the t values which indicated discontinuities in model A. As a consequence, the modulation functions of the ADP could be removed from model B, resulting in fewer parameters and lower R values than in model A.

We have reproduced the refinement of model B employing the software JANA2006 (Petricek et al., 2006). The disorder in model B is described by a split atom model

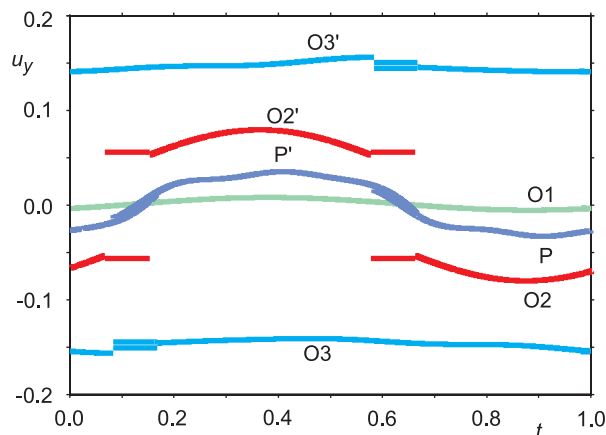


Figure 6.5: Schematic representation of the modulation functions in model M. The component u_y is shown as a function of t . Regions of disorder occur around $t = 0.12$ and $t = 0.62$.

of width of 0.084 in t . The technical realization involves the introduction of atoms Cr(a), P(a), P(b), O2(a), O3(a) and O3(b), each with an occupancy of one half and a width of 0.084 in t , while reducing the widths of the parent atoms by the same amount. The half-occupied atomic sites are not modulated in model B, because it is impossible to refine any occupational and displacive modulation parameters of these atoms due to high correlations caused by their small occupational domains in t . On the other hand, large structural variations exactly in the regions of disorder strongly suggest that these half-occupied sites will be modulated. Uncovering the crystal structure in the regions of disorder was one of the main motivations for the use of the MEM for this system.

Based on the analysis of the MEM density a new model has been developed, which provides an improved description of the structure although it gives only a marginally better fit to the data. This model, called model M, has been obtained by a real-space fit of the parameters of the modulation functions to the t -dependent positions of the atoms as they have been determined by interpretation of the MEM electron density (Figure 6.5). Because these modulation functions are determined at one hundred t -values, many more parameters can be fitted than is possible in structure refinements against diffraction data, thus obtaining a nearly perfect description of the t -dependent atomic positions as derived from the MEM density. As

Table 6.3: Number of parameters used for each atom in models B and M. The number in brackets is the number of refined parameters.

	Model B			Model M			
	Occupancy	Position	2nd ADP	Occupancy	Position	2nd ADP	3rd ADP
P	2(0)	15(15)	18(18)	2(0)	24(3)	11(11)	16(16)
P(a)	2(0)	3(3)	6(6)	6(0)	24(0)	6(6)	0
P(b)	2(0)	3(3)	6(6)	6(0)	24(0)	6(6)	0
O2	2(0)	4(4)	4(4)	2(0)	4(4)	4(4)	0
O2(a)	2(1)	3(3)	6(6)	2(1)	3(3)	6(6)	0
O1	0	8(8)	4(4)	0	8(8)	4(4)	0
O3	2(0)	24(21)	18(18)	2(0)	24(21)	18(18)	0
O3(a)	2(0)	3(3)	6(6)	2(0)	3(3)	6(6)	0
O3(b)	2(0)	3(3)	6(6)	2(0)	3(3)	6(6)	0
Cr	2(0)	16(13)	16(16)	2(0)	16(13)	16(16)	0
Cr(a)	2(1)	3(3)	6(6)	2(1)	3(3)	6(6)	0

Table 6.4: R values and partial R values (%) for model B and model M.

Reflection group	Model B		Model M		Number of reflections	
	R_F (obs)	wR_{F^2} (all)	R_F (obs)	wR_{F^2} (all)	observed	all
All	2.27	5.77	2.17	5.68	1433	2409
Main	1.65	4.08	1.57	3.97	278	283
Satellites $ m = 1$	1.77	3.08	1.70	2.94	455	495
Satellites $ m = 2$	3.30	4.98	3.17	4.91	421	569
Satellites $ m = 3$	9.06	18.22	8.77	17.79	183	495
Satellites $ m = 4$	19.62	36.88	18.46	37.04	96	567
Number of parameters	179		170			

a consequence, only a selection of the structural parameters of model M could be refined against the diffraction data, while others have been kept fixed to their values determined from the MEM density. As discussed below, an improvement of the fit to the diffraction data was only obtained by replacing the displacive modulation of the phosphorus atom by MEM-derived functions. The modulation functions of the other atoms were kept as in model B. A summary of features of models M and B is given in Table 6.3 and Table 6.4. Full details of models M and B are given as CIF files in the supplementary material.

6.4.2 MEM calculations

The electron density has been defined on a grid of $72 \times 96 \times 48 \times 48$ pixels, which corresponds to a voxel size of $0.097 \times 0.088 \times 0.096 \text{ \AA}^3$ in real space. Calculations according to the MEM have been performed with the software BAYMEM on a Compaq–DEC ES40 Workstation (van Smaalen et al., 2003). A uniform prior and the Cambridge algorithm have been used in all the calculations.

Observed, phased structure factors corrected for anomalous scattering have been generated from the diffraction data, employing model B according to the procedure described in Bagautdinov et al. (1998). They were used in one MEM calculation with weights F2 (Equation 6.6), resulting in an optimized electron density $\rho^{MEM}(\mathbf{x}_s) = \{\rho_k^{MEM}\}$. Additional MEM calculations have been performed with weights H0, H2, H4 and F4 (section 6.3). Experimental values of phases are not available. Instead the MEM employs values for phases that are those of the best structure model. Therefore, they might differ from the true phases. For a centrosymmetric structure, like $\text{Cr}_2\text{P}_2\text{O}_7$, with two values, 0 or π , for the phase of each reflection, each phase can be correct or wrong. It is at the basis of the use of Fourier and difference Fourier maps as aid in structure solution, that a reasonable structure model already produces accurate phases for the reflections. For glycine we have counted 20 wrong phases out of 3822 reflections, of which only two possessed intensities slightly larger than 3σ (Netzel et al., 2008). True phases were assumed to be the values obtained from the multipole model. For $\text{Cr}_2\text{P}_2\text{O}_7$ we do not have an independent source of true phases, so that we cannot make such an analysis in the present case.

Other MEM calculations have been performed with the combination of calculated structure factors of model B and experimental standard uncertainties as "data." Employing weight F2, the resulting density is denoted by $\rho_{cal}^{MEM}(\mathbf{x}_s) = \{\rho_{cal,k}^{MEM}\}$. Obviously, the latter calculation aims at reproducing the model, but differences with the model can occur due to intrinsic behavior of the MEM, the choice of standard uncertainties and the limited number of reflections, which are restricted to those reflections for which experimental data are available.

The computer program JANA2006 (Petricek et al., 2006) has been used for the visualization of 2-dimensional sections of the electron densities. As an example,

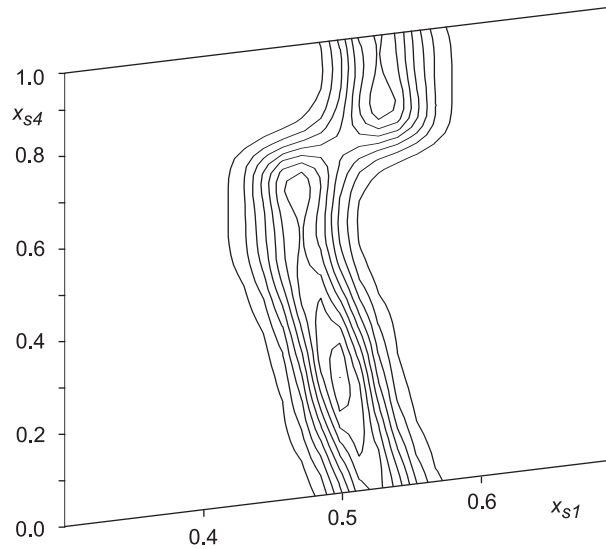


Figure 6.6: (x_{s1}, x_{s4}) -Section of the generalized electron density $\rho_s^{MEM}(\mathbf{x}_s)$ at the position of Cr ($x_1 = 0.5$, $x_2 = 0.8121$ and $x_3 = 0.0$). The contour interval is 10 % of the maximum of electron density of $267.9 \text{ electron}/\text{\AA}^3$.

Figure 6.6 gives the (x_{s1}, x_{s4}) section of $\rho^{MEM}(\mathbf{x}_s)$ centered at the position of the Cr atom. It clearly shows the modulated position of this atom.

Electron density maps have been quantitatively analyzed by the computer program EDMA (van Smaalen et al., 2003). Three-dimensional sections representing physical space have been calculated from (3+1)-dimensional superspace densities for one hundred, equally-spaced values of t with $0 \leq t < 1$. In each t -section, positions of the atoms are identified as local maxima of the density. Combining the information from all sections provides the positions of the atoms as functions of the phase of the modulation t . The three components (u_x, u_y, u_z) of the modulation function of an atom then follow as the difference between its t -dependent position in the MEM density and its basic-structure position obtained from model B. This procedure has been used, for example, to extract the modulation function of Cr from the MEM densities calculated with different weights (Figure 6.3). The consideration of especially the modulations derived from $\rho_{cal}^{MEM}(\mathbf{x}_s)$ obtained with various weights, shows that weights F2 provide the best convergence of the MEM (section 6.3).

Figure 6.7 gives the modulation functions of all atoms: modulation functions

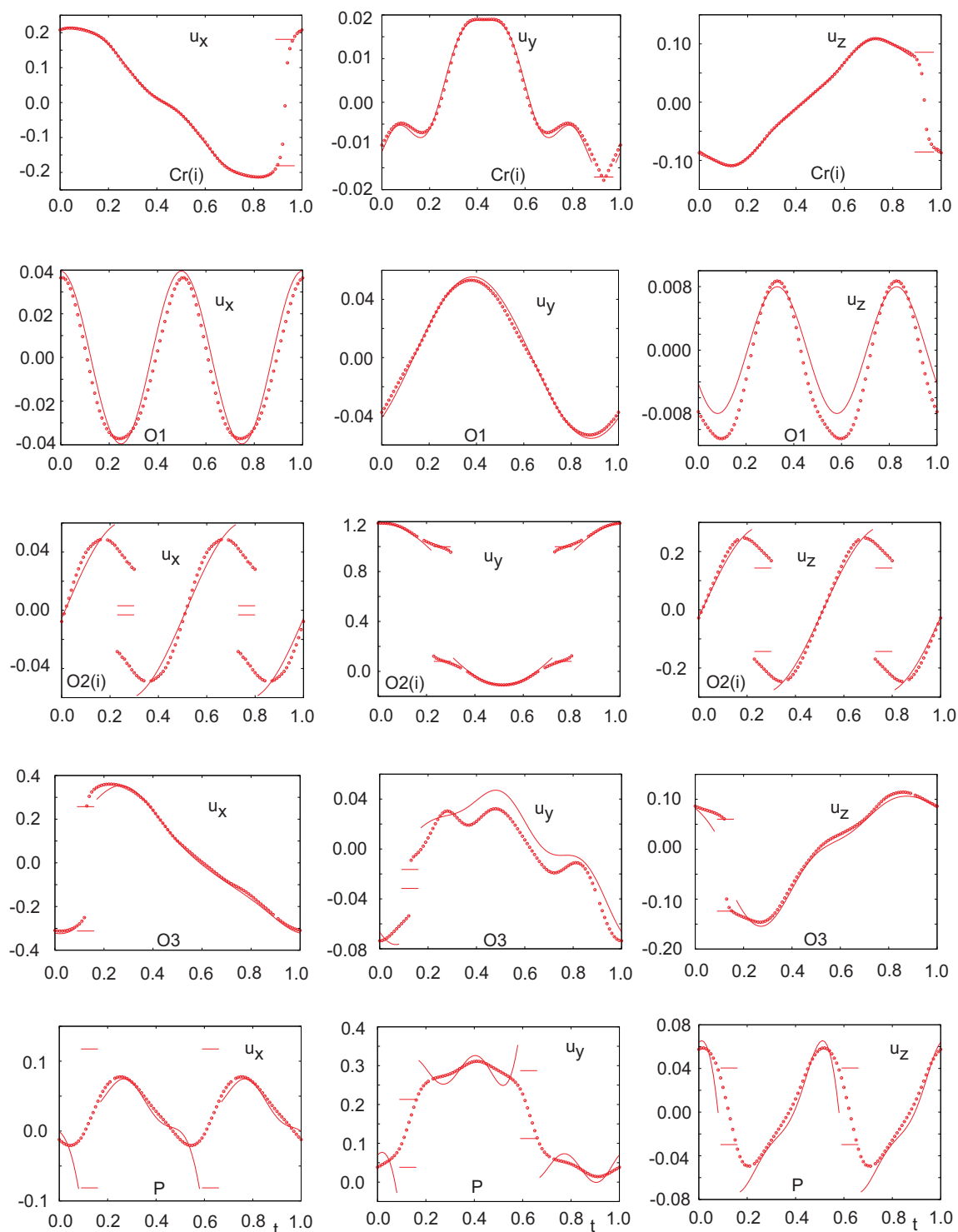


Figure 6.7: Modulation functions of the crystallographically independent atoms of $\text{Cr}_2\text{P}_2\text{O}_7$. Displacements along x , y and z are given in Å. Points are obtained from the MEM density; solid lines are the modulation functions of model B. Atoms are not necessarily bonded to each other as they are indicated in Figure 6.1.

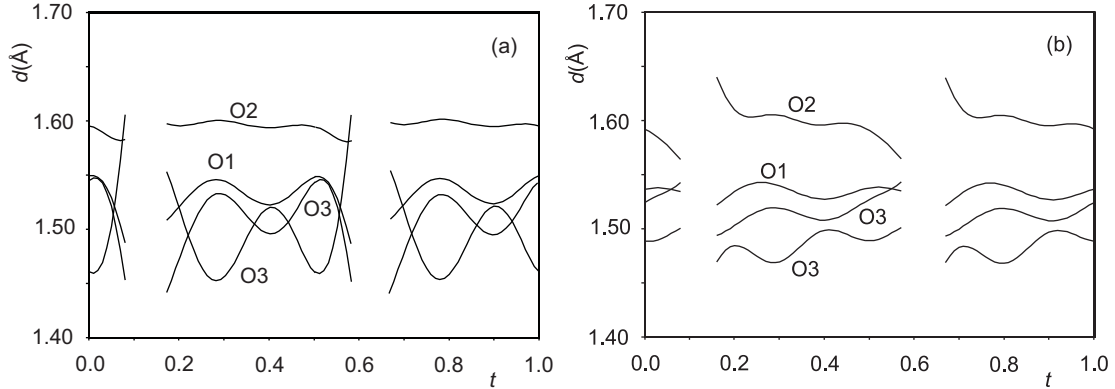


Figure 6.8: The coordination polyhedron of phosphorus in dependence on t . The disordered region is omitted. (a) P–O distances for model B. (b) P–O distances for model M.

from model B are compared to modulation functions as they have been determined from $\rho^{MEM}(\mathbf{x}_s)$. It is noticed that the true position of an atom may deviate from the MEM-derived position by an amount of up to 0.01 \AA , for the grid-size used in the present work (van Smaalen et al., 2003). However, in case of atoms on special positions this discrepancy may be zero.

6.5 Discussion

An excellent agreement is obtained between the modulated position of chromium in model B and the position determined from $\rho^{MEM}(\mathbf{x}_s)$ in the ordered region ($-0.027 < t < 0.888$) (Figure 6.7). Small discrepancies are visible for $u_y[\text{Cr}]$, but their magnitudes of up to $\Delta u_y[\text{Cr}] = 0.0012 \text{ \AA}$ are well below the accuracy with which positions of local maxima can be determined for discrete density maps with a mesh of $\sim 0.1 \text{ \AA}$ (van Smaalen et al., 2003). This excellent agreement suggests that the MEM can reliably construct the modulation functions of $\text{Cr}_2\text{P}_2\text{O}_7$. Good agreements between model B and the MEM-based modulation functions are also obtained for the atoms O1, O2 and, to a slightly smaller extent, for atom O3.

The modulated position of the phosphorus atom does not agree well between $\rho^{MEM}(\mathbf{x}_s)$ and model B (Figure 6.7). In particular, the diverging nature of the

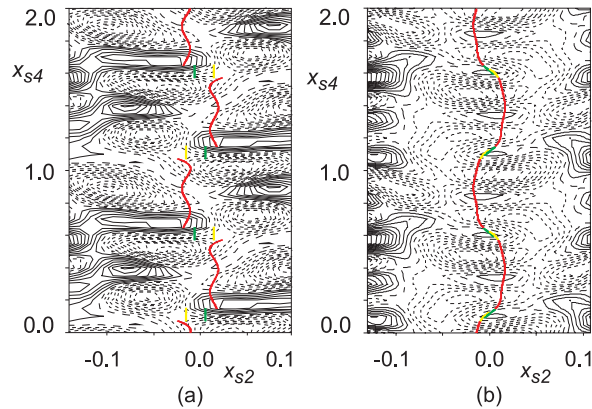


Figure 6.9: (x_{s2}, x_{s4}) -Section of the difference Fourier map centered at atom P, and obtained after refinement of (a) model B, and (b) model M. Solid lines indicate positive, dashed lines negative values. The contour interval is $0.02 \text{ electron}/\text{\AA}^3$. Minimum and maximum values over the unit cell are $-0.49/0.54 \text{ electron}/\text{\AA}^3$ for model B, and $-0.47/0.48 \text{ electron}/\text{\AA}^3$ for model M.

modulation functions in model B on approaching the disordered regions is unlikely to be a realistic feature of modulations. This interpretation is compounded by the analysis of interatomic distances between phosphorous and its four neighboring oxygen atoms, which exhibit very short P–O distances close to the disordered region [Figure 6.8(a)]. Model M is defined such that the modulated atomic positions of phosphorous closely follow the trace of maximum density in $\rho^{MEM}(\mathbf{x}_s)$. The better description of the P atom in model M is reflected by the difference Fourier maps, which exhibit much less structure around the position of P for model M than for model B, although model M retains the larger values of its difference Fourier map at positions farther away from the atoms (Figure 6.9). Furthermore, model M leads to a shortest P–O distance of 1.46 \AA that is longer than the shortest P–O distance of 1.44 \AA in model B, and compares better to P–O distances of other compounds (Fuess, 2006).

Disorder over two sites has already been proposed for the atoms Cr, P, O2 and O3 by (Palatinus et al., 2006), who gave for each of these atoms two positions of half occupancy (Model B). $\rho^{MEM}(\mathbf{x}_s)$ exhibits features that support a split-atom model and allow a refined picture to be developed for the structure within the disordered regions. The MEM densities around the atoms Cr, P and O3 appear to be smeared

into the directions of the expected split at those t -values for which disorder of two sites has been proposed (Figure 6.12 and Figure 6.13). We take this smearing as evidence for the disorder over two sites. It is not a "smoothing" effect of the MEM, because at most t values the maxima of these atoms appear as normal (Figure 6.12 and Figure 6.13). The absence of a double maximum in $\rho^{MEM}(\mathbf{x}_s)$ at the disordered positions is explained by the relatively small distance between the two positions, thus leading to a single broad maximum instead of two peaks, as observed.

The clearest description of the structure in the disordered regions has been obtained for atom O2 ($0.223 < t < 0.306$ for atom O2(i) in Figure 6.7). The MEM-density exhibits two closely-spaced local maxima near the position of O2 in the t -sections of the disordered region (Figure 6.10). Since both positions are too close to each other for simultaneous occupation, this indicates disorder of the O2 atom over two sites, as they are displayed in Figure 6.7, in agreement with model B (Palatinus et al., 2006). Unlike model B, the positions of O2 within the disordered region depend on t .

Analysis of the MEM density allows the unit cell to be dissected in atomic basins (Bader, 1994). The volume of an atomic basin provides a measure for the volume of this atom, while the integrated number of electrons should be equal to the number of electrons carried by this atom in the crystal structure under investigation. For ionic crystals, the integrated number of electrons will deviate from the atomic number, but ionic charges (differences between the atomic numbers and the integrated numbers of electrons) usually cannot be identified with formal valencies. This is especially true, if bonding involves a considerable amount of covalency, like it is the case for $\text{Cr}_2\text{P}_2\text{O}_7$. For crystals with disorder the integrated atomic charge can thus be taken as a measure for the relative occupancy of each site.

Figure 6.11 shows the normalized integrated charge of O2 as a function of the internal coordinate t . The number of electrons of O2 is 9.51 within the ordered regions. This number thus corresponds to full occupancy of the O2 site. For the disordered regions it is found that the occupancy of one position gradually increases at the expense of the occupancy of the other position at the same t value. The two modulated positions are found to be continuations of the positions in the ordered regions (Figure 6.7), whereby—going from the ordered to the disordered regions—

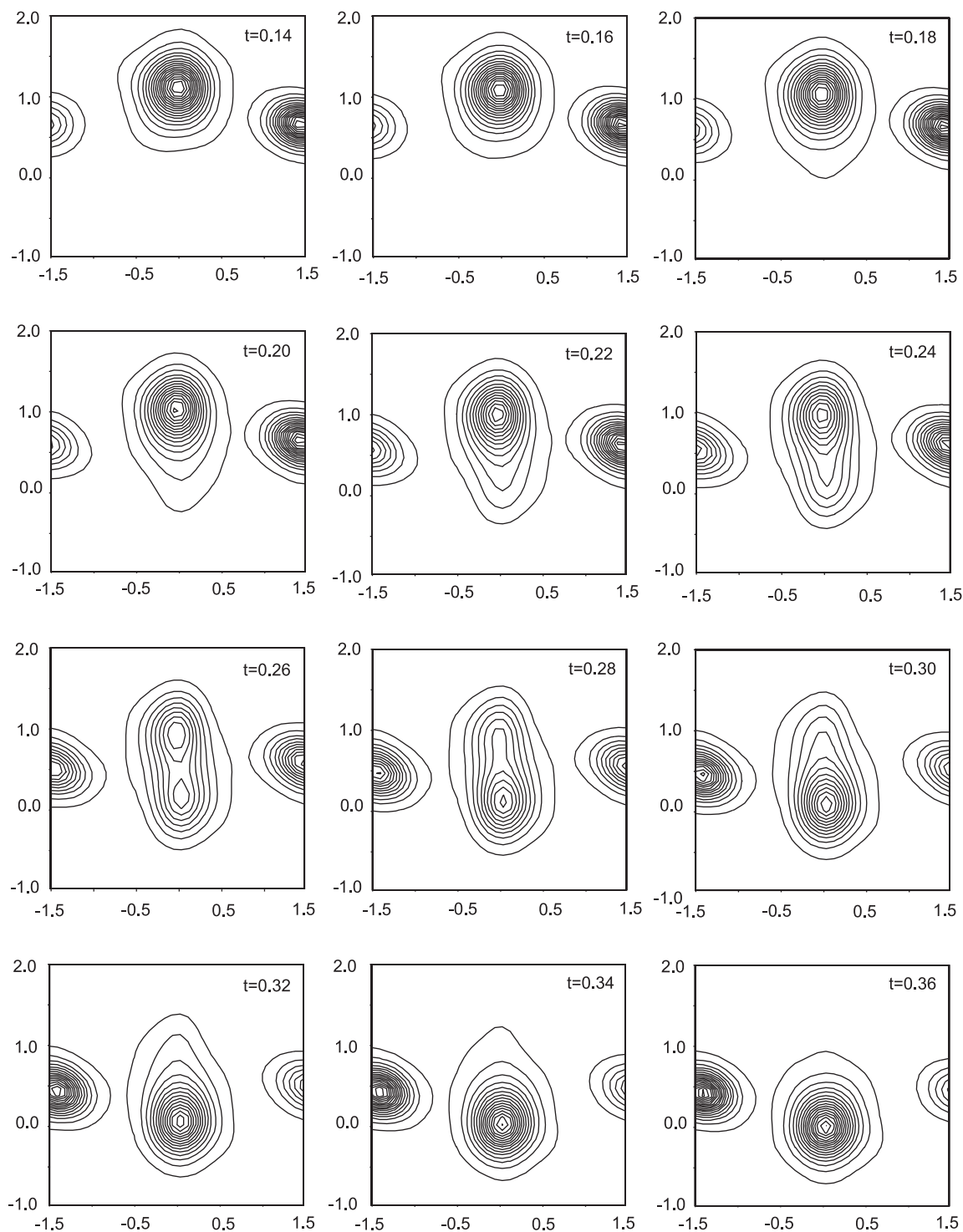


Figure 6.10: Physical-space sections of the MEM electron density centered at atom O2. The value of t is indicated for each section. Axes are labeled in Ångstrom. The contour interval is $1 \text{ electron}/\text{Å}^3$; Maximum density is $29.7 \text{ electron}/\text{Å}^3$. The two, partially visible local maxima at the borders of each pane are due to phosphorus atoms.

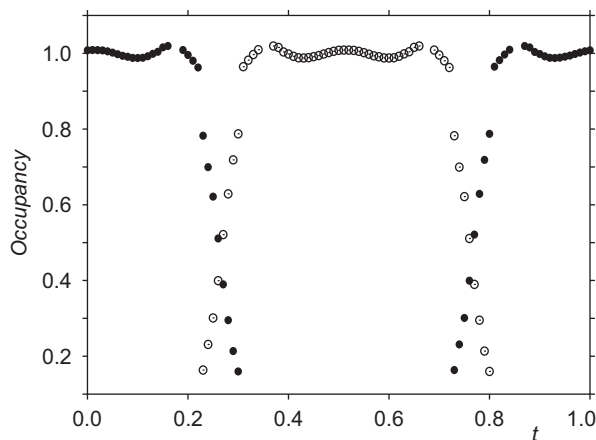


Figure 6.11: Occupancy of the split-site of atom O2 as a function of t . The occupancy is given for O2(i) (open circles; see Figure 6.1) and O2(i)* [full circles; symmetry code $(x_1, -x_2, x_3, \frac{1}{2} + x_4)$]. The integrated charge has been normalized against the average integrated charge of 9.51 electrons in the ordered region ($0.32 < t < 0.71$).

the occupancy gradually diminishes (compare Figure 6.7 and Figure 6.11).

These observations lead to the following description of the structure of $\text{Cr}_2\text{P}_2\text{O}_7$. Positions of all atoms are modulated, such that the CrO_6 and P_2O_7 units attain different positions and orientations, while deformations of these units lead to internal strain. Strain is released by the existence of disordered positions, which are characterized by the alternate occupancy of one of two conformations/orientations of the CrO_6 and P_2O_7 units. The occupational probability of each site depends on amount of strain generated by the conformations of these units.

The structure model M was developed, which should capture the various features of the modulation as derived from $\rho^{MEM}(\mathbf{x}_s)$. The observed traces of maximum density provide modulated atomic positions (Figure 6.7), while the other density features described above provide information about the structure in the disordered regions. The modulation functions of P were replaced by modulation functions fitted to the traces of maximum density in $\rho^{MEM}(\mathbf{x}_s)$. Furthermore, the distribution of electron density at the site of P suggests anharmonic displacements of this atom (Figure 6.14). Accordingly, third-order anharmonic ADPs were introduced for the P atom, and their refinement improved the fit to the diffraction data. For atoms Cr, O1, O2 and O3 the modulation functions of model B were kept, because all attempts

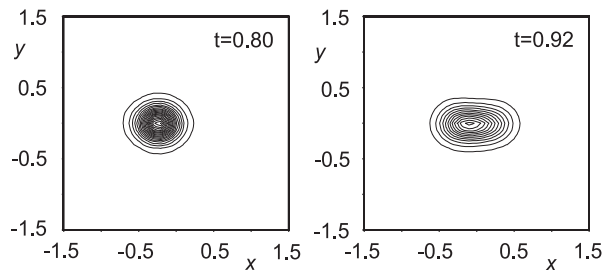


Figure 6.12: Physical-space sections of the MEM electron density centered at atom Cr for two values of t . The contour interval is 10 electron/ \AA^3 ; maximum density is 264.82 electron/ \AA^3 .

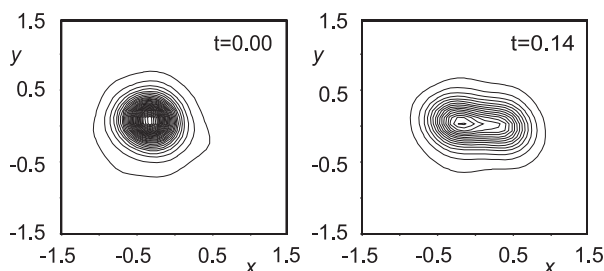


Figure 6.13: Physical-space sections of the MEM electron density centered at atom O3 for two values of t . Contour interval is 1 electron/ \AA^3 ; Maximum density is 38.2 electron/ \AA^3 .

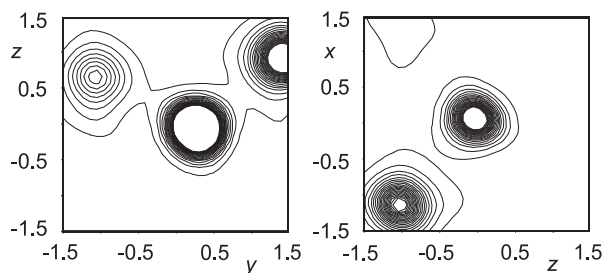


Figure 6.14: Sections of the MEM electron density parallel to physical space at $t = 0.24$ centered at the atom P. Contours of constant electron density are drawn at intervals of 1 electron/ \AA^3 up to 20 electron/ \AA^3 .

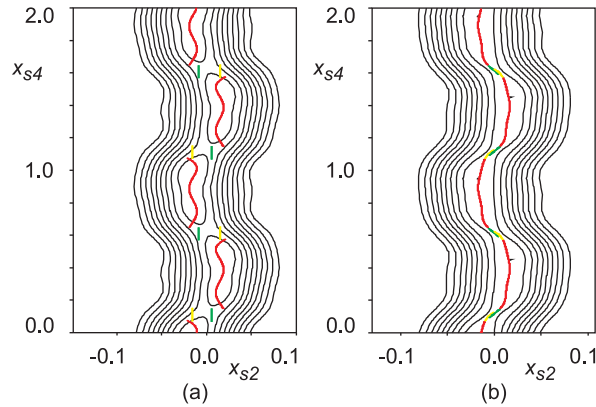


Figure 6.15: (x_{s2}, x_{s4}) -Section of the observed Fourier map of (a) model B, and (b) model M. Contours at the intervals of 10 percent of the maximum density. The modulated position is shown for atoms P (red line), P(a) (green line) and P(b) (yellow line).

to introduce MEM-based modulation functions for these atoms lead to a fit to the diffraction data that is comparable to model B, but worse than model M. One explanation for this feature is that $\rho^{MEM}(\mathbf{x}_s)$ and model B match very well in the ordered regions, so that model B already gives a good description the ordered regions of atoms Cr, O1, O2 and O3. However, the positions derived from the discrete MEM density have an intrinsic uncertainty of $\sim 0.01 \text{ \AA}$, which difference might be sufficiently large to provide a less than optimal fit to the diffraction data, while refinement of the many parameters of the MEM-based modulation functions is not possible due to inter-dependencies between them. Modeling the disordered regions is difficult, because we do not have a method to derive split-atom positions from the smeared maxima in $\rho^{MEM}(\mathbf{x}_s)$ in the disordered regions. For the phosphorus atom with MEM-based modulation functions, only basic structure parameters and modulated ADPs have been refined.

Model M gives a slightly better fit ($R_F = 2.17 \%$) to the diffraction data than model B does ($R_F = 2.27 \%$). Other indicators—*e.g.* the difference Fourier and Fourier maps around phosphorus (Figure 6.9 and Figure 6.15)—also suggest model M to be the better model. Despite the construction of a complete picture of the modulations in $\text{Cr}_2\text{P}_2\text{O}_7$, it is rather disappointing that this picture could not be translated into a model. This indicates that it is extremely difficult to derive a model

for all features of the crystal structure of this compound, which include modulated split-atom disorder but probably also modulated anharmonic ADPs in the disordered regions. Furthermore, the MEM-derived positions cannot be refined due to correlations between parameters, while the accuracy of the MEM-derived positions (~ 0.01 Å) is insufficient to give the best possible fit to the diffraction data without further refinement.

6.6 Conclusions

The Maximum Entropy Method (MEM) in superspace has been applied to X-ray diffraction data of incommensurately modulated $\text{Cr}_2\text{P}_2\text{O}_7$. The interpretation of $\rho^{MEM}(\mathbf{x}_s)$ according to Bader's atoms-in-molecules theory has provided the modulated atomic positions, and thus the modulation functions. The modulation functions in the ordered regions of Cr, O1, O2 and O3 have been found to agree well between $\rho^{MEM}(\mathbf{x}_s)$ and model B from Palatinus et al. (2006).

The MEM has led to a modulation function of phosphorus that is different from model B within the ordered regions (Figure 6.7). Both the difference Fourier maps (Figure 6.9) and an analysis of P–O interatomic distances (Figure 6.8) indicate that the MEM-derived modulation function is closer to the true modulation of phosphorus than the modulation function from model B.

The MEM-density has provided direct evidence for a split-atom model (Figure 6.10), which is interpreted as positions in the structure where the P_2O_7 and CrO_6 groups occur in one of two orientations/conformations with complementary probabilities. Other features derived from $\rho^{MEM}(\mathbf{x}_s)$ are that these probabilities are not equal, but depend on t , as well as that the conformations depend on t . Furthermore, $\rho^{MEM}(\mathbf{x}_s)$ gives smeared densities of complex shapes around the atoms in the disordered regions, which indicate a structure in the disordered regions that is a combination of modulated positions, modulated occupancies and modulated anharmonic ADPs. We did not succeed constructing a fully satisfactory structure model that captures all these features.

Reasons for the failure to find a model that would give a much better fit to the diffraction data—especially to the higher-order satellite reflections— than model B

(Table 6.4) include the complex nature of the structure, but also the limited accuracy of ~ 0.01 Å of MEM-derived positions together with the impossibility to refine all the parameters that were necessary to construct a model based on $\rho^{MEM}(\mathbf{x}_s)$, due to interdependencies between these parameters. Nevertheless, we believe that the MEM has established the true nature of the modulations in $\text{Cr}_2\text{P}_2\text{O}_7$.

Acknowledgements

We thank Lukas Palatinus for providing electronic files for the diffraction data and for model B, and we thank Vaclav Petricek, Michal Dusek for help with Jana2006. Financial support was obtained from the German Science Foundation (DFG).

Chapter 7

Summary

In this thesis, modulated properties of incommensurately modulated crystals are studied by the Maximum Entropy Method (MEM). This was done exemplarily on the compounds Rb_2ZnCl_4 and $\text{Cr}_2\text{P}_2\text{O}_7$. To do so, the MEM derived (3+1)-dimensional superspace electron density was analysed to receive information on atomic positions and their modulation, and structure refinement by the method of least-squares and interpretation of the difference-Fourier maps were performed to better describe the atomic displacement parameters (ADPs) and to improve the applied structural models. All the MEM calculations are done by the computer program BAYMEM (van Smaalen et al., 2003). The analysis of this MEM reconstructed density map is done by the computer program EDMA (van Smaalen et al., 2003).

The atom position in the electron density map can be defined in two different ways, as position of the local maximum of electron density or as the center-of-charge of the electron density belonging to the particular atom. The first definition, position of the maximum, has been used in previous studies (Palatinus and van Smaalen, 2002). It is appropriate for structures which do not contain atoms with anharmonic ADPs. For atoms defined by anharmonic ADPs the second definition is suitable, as for those atoms the maximum of the electron density and the center-of-charge of the electron density do not superpose anymore. For atoms described by (only) harmonic ADPs both definitions will give almost the same results. The data set of intensities of Bragg reflections of Rb_2ZnCl_4 , including main reflections and satellite reflections up to fifth-order, was used for structure refinement and maximum entropy calculations.

The MEM derived traces of center-of-charge of individual atoms coincide with the displacement modulation functions of atoms in the final model. Modulations of ADPs and anharmonic ADPs are visible in the MEM derived electron density as variations of the distributions of the density around the average position. The large number of reflections in the data set makes the structure refinement of this complex model with modulated terms of ADPs and anharmonic ADPs possible. The analysis of the accurately determined high-order Fourier coefficients shows that the modulation cannot be interpreted as a soliton wave proposed by Aramburu et al. (2006).

All the structure refinements are performed with the computer program JANA2006 (Petricek et al., 2006). A first model (model A) was established in analogy with the published structure (Aramburu et al., 2006), which includes all Fourier coefficients up to fifth-order for the positional modulation. By incorporation of the first- and second-order Fourier coefficients to the harmonic ADPs, it was extended to model B. With this model B the phased observed diffraction data for the MEM calculations was created. The analysis of the MEM derived electron density showed that modulated anharmonic ADPs of third order are necessary. Therefore third order anharmonic ADPs with up to fifth-order Fourier coefficients were added the model B, by which the model C was created. Due to large correlations, the refinement of this model can not converge. To overcome this problem, the third order anharmonic ADPs with values less than σ have been set to zero (model C_r). Both models, C and C_r , fit the diffraction data equally well. The improvement of the fit to the data for increasing complexity of the models from A to C_r is verified by the difference-Fourier maps. Those maps also reveal that unmodulated fourth-order anharmonic ADPs are necessary to properly describe the structure. In the final model D_r , fourth-order anharmonic ADPs are added to atoms Rb1, Rb2 and Cl3. Calculation of the R values against only the strong reflections with $I > 5\sigma(I)$ showed that these R values of the higher-order satellite reflections are lower than the ones for the full data set. This indicates that the limited accuracy of the present data due to limited counting statistics of the detector is a reason for the high R values of the higher-order satellite reflections.

The MEM in (3+1)-dimensional superspace has been applied to X-ray diffraction

data of incommensurately modulated $\text{Cr}_2\text{P}_2\text{O}_7$. The interpretation of the MEM derived electron density according to Bader's atoms-in-molecules theory has provided the modulated atomic positions as function of the phase of the modulation t , and thus the modulation functions. The modulation functions which have been derived from the MEM reconstructed electron density map in the ordered regions of Cr, O1, O2 and O3 have been found to agree well with the structure model proposed by Palatinus et al. (2006).

The MEM derived electron density has provided direct evidence for a splitting of atomic positions, which is interpreted in such way that the P_2O_7 and CrO_6 groups occur in one of two orientations/conformations with complementary occupational probabilities. Other features obtained from MEM derived electron density are that these probabilities are not constant, but depend on the phase of the modulation t , and also, that the conformations are a function of t . Furthermore, the MEM derived electron density gives smeared densities of complex shapes around the atoms in the disordered regions. This indicates that the structure in the disordered regions has to be described as a combination of modulated atomic positions, modulated occupancies and modulated anharmonic ADPs.

The structure model from Palatinus et al. (2006) was reproduced (model B). Fourier coefficients of up to fourth- and second-order are used to describe the positional modulation and harmonic ADPs modulation respectively. The phased observed diffraction data for the MEM calculations was created with model B. The parameters of the displacive modulation function of atom P were obtained by a real-space fit to the MEM derived modulation functions. Then the structure model M was created from model B by replacing the displacive modulation function of the atom P by the MEM-based fitted parameters. All atoms are positional modulated and all except O1 are occupational modulated. Up to second-order Fourier coefficients are used to define the modulation of the harmonic ADPs of all atoms. The third order anharmonic ADPs are included only for atom P in the disordered region. Both the difference Fourier maps and the analysis of P–O interatomic distances indicate that the MEM derived modulation function is closer to the true modulation of phosphorus than the published modulation function from Palatinus et al. (2006).

For the standard description of modulated structures, basic positions of atoms,

harmonic ADPs and modulation functions are included in the structure model. The modulation functions can be a combination of positional modulation, occupational modulation and/or modulation of harmonic ADPs.

In the present thesis, structure refinements, interpretation of difference-Fourier maps and the analysis of the MEM derived electron density have been combined to better characterize the incommensurately modulated structures. Our results suggest that the modulation of harmonic ADPs, anharmonic ADPs and its modulation form an intrinsic part of incommensurately modulated structures. We have shown that with a data set of certain resolution and satellite reflections of higher order, the inclusion of modulation of harmonic ADPs, the anharmonic ADPs and the modulation of anharmonic ADPs can significantly improve the fit of the structure model to the diffraction data. Such model then better represents the true nature of the structure under investigation.

Chapter 8

Zusammenfassung

Im Rahmen der vorliegenden Arbeit wurden unter Anwendung der Maximum-Entropie-Methode (MEM) modulierte Eigenschaften inkommensurabel modulierter Kristalle untersucht. Dies wurde exemplarisch an den beiden Verbindungen Rb_2ZnCl_4 und $\text{Cr}_2\text{P}_2\text{O}_7$ durchgeführt. Unter Anwendung der MEM wurden die Elektronendichten im (3+1)-dimensionalen Superraum hergeleitet und analysiert, um Informationen über Atompositionen und deren Modulation zu bekommen, sowie Strukturverfeinerungen mittels der Methode der kleinsten Quadrate und Interpretationen von Differenz-Fourier-Karten durchgeführt, um die atomaren Verschiebungsparameter (ADPs) besser beschreiben zu können und um die angewandten Strukturmodelle zu optimieren. Die Berechnungen zur MEM wurden mit dem Computer-Programm BAYMEM (van Smaalen et al., 2003) gerechnet, die Analyse der so gewonnenen Elektronendichten mit dem Computer-Programm EDMA (van Smaalen et al., 2003).

Die Lage der Atome in der Elektronendichte kann auf zwei unterschiedliche Weisen definiert werden, zum einen als Lage des Maximums der Elektronendichte, zum anderen als Ladungszentrum der Elektronendichte des entsprechenden Atoms. In vorangehenden Studien (Palatinus and van Smaalen, 2002) wurde die Lage des Maximums der Elektronendichte als Lage des Atoms definiert. Diese Definition eignet sich gut für Strukturen, die keine Atome mit anharmonischen ADPs beinhalten. Für Atome, die mit anharmonischen ADPs beschrieben werden, ist die zweite Definition passender, da für solche Atome die Lage des Maximums der Elektronendichte und das Ladungszentrum der Elektronendichte nicht mehr deckungsgleich

sind. Für Atome, die (nur) mit harmonischen ADPs beschrieben werden, liefern beide Definitionen annähernd gleiche Ergebnisse.

Strukturverfeinerungen und die Berechnungen mittels MEM für Rb_2ZnCl_4 wurden an einem Datensatz mit Hauptreflexen und Satellitenreflexen bis einschließlich fünfter Ordnung gerechnet. Ein Vergleich der displaziven Modulationsfunktionen der einzelnen Atome im Endmodell als Funktion der Phase der Modulation t mit den Lagen der Ladungszentren der Atome, die aus den MEM berechneten (3+1)-dimensionalen Elektronendichten abgeleitet wurden, zeigt, dass beide übereinstimmen. Auch die Modulationen der harmonischen und anharmonischen ADPs sind in den MEM berechneten Elektronendichten sichtbar, und zwar als Schwankungen in der Verteilung der Elektronendichte um die Ausgleichslagen der einzelnen Atome. Die große Anzahl an gemessenen Reflexen (Hauptreflexe und Satellitenreflexe bis einschließlich fünfter Ordnung) ermöglicht die Verfeinerung des relativ komplexen Endmodells mit Modulationsfunktionen für die harmonischen und anharmonischen ADPs. Die Analyse der genau bestimmten Fourier-Koeffizienten der höheren Ordnung zeigt, dass die Modulation der atomaren Struktur nicht als Soliton-Welle gedeutet werden kann, wie von Aramburu et al. (2006) vorgeschlagen.

Die Strukturverfeinerungen wurden alle mit dem Computer-Programm JANA2006 (Petricek et al., 2006) durchgeführt. Ein erstes Strukturmodell wurde aufgestellt, um die bereits veröffentlichte Struktur (Aramburu et al., 2006) zu reproduzieren. Dieses Modell (Modell A) beinhaltet alle Fourier-Koeffizienten bis fünfter Ordnung für die displazive Modulation der einzelnen Atome. Darauf aufbauend wurde das Modell B aufgestellt, indem Fourier-Koeffizienten der ersten und zweiten Ordnung für die harmonischen ADPs hinzugefügt wurden. Mit diesem Modell B wurden die Phasen für die gemessenen Beugungsdaten erzeugt, die für die MEM-Berechnungen notwendig sind. Die Analyse der MEM berechneten (3+1)-dimensionalen Elektronendichte ergab, dass zusätzliche modulierte, anharmonischen ADPs der dritten Ordnung für die einzelnen Atome notwendig sind. Diese wurden dem Modell B hinzugefügt, was dann Modell C ergab. Aufgrund großer Korrelationen kann die Verfeinerung dieses Modells C aber nicht konvergieren. Zur Lösung dieses Problems wurden alle Fourier-Koeffizienten der anharmonischen ADPs der dritten Ordnung mit Werten kleiner als σ gleich Null gesetzt (Modell C_r). Beide Modelle, C und C_r ,

entsprechen den Beugungsdaten gleich gut. Die immer bessere Übereinstimmung von Strukturmodell und Beugungsdaten mit steigender Komplexität von Modell A bis Modell C_r kann mittels Differenz-Fourier-Karten überprüft und nachvollzogen werden. Die Differenz-Fourier-Karten zeigen auch deutlich auf, dass nicht-modulierte anharmonische ADPs der vierten Ordnung notwendig sind, um die Struktur richtig zu beschreiben. Im Endmodell (Modell D_r) wurden zusätzlich nicht-modulierte anharmonische ADPs der vierten Ordnung verwendet, um die Atome Rb1, Rb2 und Cl3 zu beschreiben. Die Berechnung von R -Werten mit diesem Endmodell D_r nur gegen starke Reflexe mit $I > 5\sigma(I)$ zeigt, dass diese R -Werte für die Satellitenreflexe höherer Ordnung kleiner sind, als die R -Werte gegen den kompletten Datensatz. Dies ist ein Hinweis auf die begrenzte Genauigkeit des verwendeten Datensatzes aufgrund der begrenzten Zählstatistik des Detektors und erklärt auch die höheren R -Werte der Satellitenreflexe höherer Ordnung.

Die MEM im (3+1)-dimensionalen Superraum wurde auf Röntgenstrahl-Beugungsdaten des inkommensurabel modulierten $\text{Cr}_2\text{P}_2\text{O}_7$ angewandt. Die Interpretation der mittels MEM berechneten (3+1)-dimensionalen Elektronendichte gemäß Baders "atoms-in-molecules"-Theorie lieferte modulierte Atompositionen als Funktion der Phase der Modulation t , und somit die atomaren Modulationsfunktionen. Die atomaren Modulationsfunktionen in den geordneten Regionen, die aus der MEM berechneten (3+1)-dimensionalen Elektronendichte für die Atome Cr, O1, O2 und O3 abgeleitet wurden, stimmen gut mit dem von Palatinus et al. (2006) vorgeschlagenem Strukturmodell überein.

Die mittels MEM berechnete (3+1)-dimensionale Elektronendichte zeigt deutlich eine Aufspaltung von Atompositionen, die derart interpretiert wurde, dass die P_2O_7 - und die CrO_6 -Gruppen in jeweils einer von zwei Orientierungen/Konformationen vorliegen, die gegenseitig komplementäre Besetzungswahrscheinlichkeit aufweisen. Weiter konnte aus der MEM berechneten (3+1)-dimensionalen Elektronendichte herausgelesen werden, dass diese Besetzungswahrscheinlichkeiten nicht konstant sind, sondern sich als Funktion der Phase der Modulation t ändern. Auch die Konformationen stellen Funktionen von t dar. Für die Atome in den ungeordneten Regionen ergab die MEM verschmierte Dichten mit komplexer Form. Dies weist auf eine atomare Struktur in den ungeordneten Regionen hin, die als Kombination von

modulierten Atompositionen mit modulierten Besetzungswahrscheinlichkeiten und modulierten anharmonischen ADPs beschrieben werden muss.

In einem ersten Schritt wurde das Strukturmodell von Palatinus et al. (2006) reproduziert (Modell B). Für alle Atome wurden Fourier-Koeffizienten bis zur vierten Ordnung für die displazive Modulation und bis zur zweiten Ordnung für die atomaren Modulationsfunktionen der harmonischen ADPs verwendet. Modell B diente zur Generierung der Phasen für die gemessenen Beugungsdaten, die für die MEM-Berechnungen notwendig sind. Aus der MEM berechneten (3+1)-dimensionalen Elektronendichte wurden dann mittels eines “real space fits” die Parameter der atomaren Modulationsfunktionen des Atoms P bestimmt. Dann wurde das Strukturmodell M erstellt, indem die Parameter der displaziven atomaren Modulationsfunktion für das Atom P aus dem Modell B entfernt und durch die MEM-basierten gefitteten Parameter ersetzt wurden. Alle Atome sind displaziv moduliert und alle ausser O1 besetzungsmoduliert. Fourier-Koeffizienten bis zur zweiten Ordnung wurden für die atomaren Modulationsfunktionen der harmonischen ADPs für alle Atome verwendet. Zusätzlich wurden für das Atom P in der ungeordneten Region auch anharmonische ADPs der dritten Ordnung hinzugefügt. Sowohl Differenz-Fourier-Karten, als auch die Analyse der P–O interatomaren Abstände weisen darauf hin, dass die MEM-basierte atomare Modulationsfunktion näher an der wahren Modulation von Phosphor liegt, als die veröffentlichte atomare Modulationsfunktion von Modell B (Palatinus et al., 2006).

Zur Beschreibung modulierter Strukturen werden im Allgemeinen als Strukturmodell die Basispositionen der Atome, harmonische ADPs und atomare Modulationsfunktionen verwendet. Die atomaren Modulationsfunktionen könne eine Kombination aus displaziver Modulation, Besetzungsmodulation und/oder Modulation der harmonischen ADPs sein.

In der vorliegenden Arbeit wurden Strukturverfeinerungen, Interpretation der Differenz-Fourier-Karten und die Analyse der MEM berechneten (3+1)-dimensionalen Elektronendichte kombiniert, um die inkommensurabel modulierten Strukturen besser beschreiben zu können. Unsere Forschungsergebnisse lassen den Schluss zu, dass die Modulation der harmonischen ADPs, anharmonische ADPs und die Modulation der anharmonischen ADPs ein intrinsischer Bestandteil der inkommensurabel mod-

ulierten Strukturen ist. Wir haben gezeigt, dass mit Datensätzen einer bestimmten Auflösung und Satellitenreflexen bis höherer Ordnung die Einbeziehung von Modulationen der harmonischen ADPs, anharmonischer ADPs und der Modulationen der anharmonischen ADPs die Übereinstimmung von Strukturmodell und Datensatz verbessern kann. Ein solches Strukturmodell bildet die wahre Natur der zu untersuchenden Strukturen besser ab.

Appendix A

Supplementary materials:



Table A.1: Basic positions (relative coordinates) of the crystallographically independent atoms in model A and model D_r .

Atom	Model A			Model D_r		
	x^0	y^0	z^0	x^0	y^0	z^0
Rb1	0.25	0.40659(8)	0.62976(8)	0.25	0.40660(4)	0.62969(4)
Rb2	0.25	0.81909(4)	0.48680(6)	0.25	0.81921(2)	0.48673(3)
Zn	0.25	0.42189(5)	0.22339(7)	0.25	0.42179(3)	0.22344(3)
Cl1	0.25	0.42044(14)	-0.01861(17)	0.25	0.41962(8)	-0.01837(9)
Cl2	0.25	0.58417(12)	0.32210(17)	0.25	0.58430(6)	0.32169(9)
Cl3	0.00210(13)	0.33922(10)	0.31206(13)	0.00171(7)	0.33945(6)	0.31245(8)

Table A.2: Basic-structure parameters (\AA^2) and modulation amplitudes (\AA^2) of the harmonic ADPs for model D_r . Values have been multiplied by 10^5 ; standard uncertainties are given in parenthesis.

Atom	Function	U_{11}	U_{22}	U_{33}	U_{12}	U_{13}	U_{23}
Rb1	Basic	4160(40)	6340(70)	1760(50)	0	0	-170(30)
	sin1	0	0	0	444(16)	-101(12)	0
	cos1	0	0	0	648(15)	-389(12)	0
	sin2	120(20)	470(40)	50(30)	0	0	-112(18)
	cos2	-110(20)	20(30)	10(20)	0	0	30(20)
Rb2	Basic	3410(40)	2020(40)	1540(40)	0	0	-80(19)
	sin1	0	0	0	-382(10)	294(10)	0
	cos1	0	0	0	113(9)	-45(9)	0
	sin2	3(17)	0(20)	-16(19)	0	0	-20(13)
	cos2	312(16)	50(20)	50(19)	0	0	-9(13)
Zn	Basic	2085(15)	1969(19)	1426(18)	0	0	-21(8)
	sin1	0	0	0	76(10)	-79(9)	0
	cos1	0	0	0	-16(10)	-15(9)	0
	sin2	-1(16)	-20(20)	-10(20)	0	0	5(17)
	cos2	48(16)	40(20)	-10(20)	0	0	-30(15)
Cl1	Basic	7660(60)	3730(50)	1390(40)	0	0	-430(20)
	sin1	0	0	0	1750(50)	160(40)	0
	cos1	0	0	0	-180(50)	-280(40)	0
	sin2	-470(80)	-70(70)	0(60)	0	0	-50(40)
	cos2	1520(90)	-70(70)	20(60)	0	0	-80(40)
Cl2	Basic	7500(70)	2320(40)	2170(40)	0	0	-680(20)
	sin1	0	0	0	100(50)	260(50)	0
	cos1	0	0	0	-760(40)	190(40)	0
	sin2	-50(80)	0(60)	20(60)	0	0	10(40)
	cos2	-2180(100)	60(60)	50(70)	0	0	-80(40)
Cl3	Basic	2730(50)	6800(100)	3250(80)	-2240(50)	-530(50)	1810(60)
	sin1	-80(30)	-490(60)	850(40)	310(30)	-60(20)	270(40)
	cos1	-490(20)	-450(50)	-720(40)	580(30)	240(20)	-480(30)
	sin2	130(30)	350(80)	290(60)	-310(40)	-190(30)	330(50)
	cos2	-330(30)	-1620(70)	-120(50)	770(40)	230(30)	-690(60)

Table A.3: Values of fourth-order anharmonic ADPs (D_{ijkl} multiplied by 10^5) of model D_r .

D_{ijkl}	Rb1	Rb2	Cl3
D_{1111}	-150(30)	-90(20)	-70(30)
D_{1112}	0	0	-16(12)
D_{1113}	0	0	-32(13)
D_{1122}	-53(5)	-34(3)	-28(8)
D_{1123}	-2(3)	-0.3(18)	-12(6)
D_{1133}	-47(6)	-64(4)	-73(9)
D_{1222}	0	0	6(8)
D_{1223}	0	0	4(5)
D_{1233}	0	0	-1(5)
D_{1333}	0	0	-13(12)
D_{2222}	-62(6)	-27(3)	-25(12)
D_{2223}	2(3)	-0.7(11)	4(7)
D_{2233}	21(3)	12.1(14)	44(6)
D_{2333}	8(4)	3(2)	20(9)
D_{3333}	-98(14)	-121(10)	-210(20)

Table A.6: Modulation amplitude (multiplied by 10^5) of third order anharmonic ADP(C_{ijk}) of model D_r (part 3).

Atom	Function	C_{111}	C_{112}	C_{113}	C_{122}	C_{123}	C_{133}	C_{222}	C_{223}	C_{233}	C_{333}	
Cl2	sin1	300(200)	0	0	0	0	0	0	0	0	0	
	cos1	-1520(160)	0	0	-35(19)	0	-70(40)	0	0	0	0	
	sin2	0	-120(50)	60(30)	0	0	0	0	0	0	0	
	cos2	0	0	-90(60)	0	0	0	0	-19(16)	0	0	
	sin3	400(200)	0	0	0	0	0	0	0	0	0	
	cos3	2200(300)	0	0	70(40)	0	90(80)	0	0	0	0	
	sin5	-1100(500)	0	0	-160(90)	70(100)	-210(170)	0	0	0	0	
	cos5	-2900(600)	0	0	0	0	30(180)	0	0	0	0	
	Cl3	sin1	-80(50)	100(30)	0	-90(20)	0	0	140(30)	81(150)	0	0
		cos1	250(40)	-210(20)	120(20)	234(18)	115(13)	0	-360(20)	-162(15)	109(15)	0
sin2		-70(60)	30(20)	40(30)	-46(19)	0	-40(30)	40(20)	0	-23(18)	-50(40)	
cos2		-150(60)	140(30)	90(30)	-130(20)	-72(18)	50(30)	170(30)	75(17)	0	-110(40)	
sin3		180(110)	-100(50)	-150(50)	130(30)	0	0	-130(50)	-100(30)	40(40)	-290(80)	
cos3		0	0	60(50)	-190(30)	-130(30)	0	260(40)	60(30)	30(30)	260(8)	
sin5		230(160)	-160(90)	-10(90)	110(60)	0	0	-280(90)	-70(70)	-20(80)	20(180)	
cos5		60(180)	-150(90)	0	120(60)	0	-80(80)	0	90(70)	100(70)	-90(170)	

Table A.7: Comparison of refinement of models against present data, number of parameters, $(\Delta\rho)_{max}$, $(\Delta\rho)_{min}$ and R values of each order reflections are given, models are different in number of atoms with fourth order anharmonic ADPs: D1(Zn), D2(Rb1), D3(Rb2), D4(Zn Rb1), D5(Rb1 Rb2), D6(Zn Cl1 Cl2), D7(Rb1 Rb2 Cl3), D8(Rb1 Rb2 Cl1 Cl3), D9(Rb1 Rb2 Zn Cl3), D10(Rb1 Rb2 Cl1 Cl2 Cl3), D11(Rb1 Rb2 Zn Cl1 Cl2 Cl3),.

	D1	D2	D3	D4	D5	D6	D7	D8	D9	D10	D11
All	0.0605	0.0620	0.0598	0.0582	0.0575	0.0597	0.0563	0.0554	0.0486	0.0549	0.0468
$m = 0$	0.0521	0.0545	0.0522	0.0495	0.0497	0.0516	0.0493	0.0484	0.0396	0.0482	0.0388
$ m = 1$	0.0638	0.0639	0.0616	0.0620	0.0593	0.0623	0.0561	0.0550	0.0513	0.0537	0.0472
$ m = 2$	0.0990	0.0982	0.0986	0.0983	0.0974	0.0982	0.0969	0.0969	0.0963	0.0969	0.954
$ m = 3$	0.2040	0.2035	0.2036	0.2024	0.2031	0.2033	0.2003	0.2005	0.1996	0.2001	0.1967
$ m = 4$	0.2901	0.2882	0.2903	0.2904	0.2908	0.2911	0.2987	0.2992	0.3133	0.2972	0.3025
$ m = 5$	0.1744	0.1734	0.1723	0.1730	0.1707	0.1740	0.1619	0.1623	0.1664	0.1625	0.1664
No. of parameters	365	365	365	374	374	383	389	398	398	407	416
$(\Delta\rho)_{max}$ ($e \text{ \AA}^{-3}$)	2.11	2.11	1.75	2.04	1.78	2.03	1.71	1.76	1.50	1.77	1.59
$(\Delta\rho)_{min}$ ($e \text{ \AA}^{-3}$)	-2.06	-2.06	-1.86	-2.03	-1.78	-2.02	-1.78	-1.78	-1.39	-1.80	-1.47
$(j.P.D.F)_{min}$ ($e \text{ \AA}^{-3}$)											
Rb1	0	-0.01	-0.00	-0.17	-0.21	0	-0.21	-0.40	-10.80	-0.19	-20.80
Rb2	0	-0.02	0	0	-1.05	-0.02	-1.04	-2.91	-67.54	-5.67	-145.24
Zn	-1.50	0.00	-0.03	-17.72	0	-3.59	0	-0.01	-447.10	-0.15	-1042.14
Cl1	-0.08	-0.01	-0.07	-0.01	-0.02	-6.40	-0.05	-61.13	-0.08	-106.02	-378.06
Cl2	-0.04	-0.41	-0.05	0	0	-0.80	0	0	0	-1.09	-69.42
Cl3	-0.54	-0.57	-0.30	-0.53	-0.54	-0.55	-2.05	-3.44	-39.12	-4.38	-80.03

Table A.8: Amplitudes (relative coordinates) of the displacement modulation function (multiplied by 10^5) after refinement of the model of Aramburu against Aramburu data.

Atom	n	A_x^n	A_y^n	A_z^n	B_x^n	B_y^n	B_z^n
Rb1	1	1250(40)	0	0	-1180(40)	0	0
	2	0	-33(18)	110(20)	0	-227(18)	20(20)
	3	-80(40)	0	0	10(40)	0	0
	5	129(18)	0	0	-140(20)	0	0
Rb2	1	1710(30)	0	0	-140(30)	0	0
	2	0	12(10)	-65(19)	0	12(10)	0(20)
	3	-100(30)	0	0	-120(30)	0	0
	5	132(15)	0	0	30(20)	0	0
Zn	1	1030(30)	0	0	330(30)	0	0
	2	0	-38(11)	2(9)	0	-6(10)	33(17)
	3	20(20)	0	0	-170(30)	0	0
	5	-108(15)	0	0	15(15)	0	0
Cl1	1	3980(90)	0	0	700(80)	0	0
	2	0	-110(40)	-10(40)	0	-130(30)	0(50)
	3	20(90)	0	0	120(70)	0	0
	5	390(50)	0	0	-20(60)	0	0
Cl2	1	820(80)	0	0	5420(90)	0	0
	2	0	-30(50)	40(50)	0	-80(30)	130(50)
	3	-710(100)	0	0	-1260(90)	0	0
	5	250(60)	0	0	250(70)	0	0
Cl3	1	580(50)	-60(30)	-1120(40)	-1860(50)	2690(30)	1440(50)
	2	50(50)	-10(30)	30(40)	40(30)	-40(30)	70(30)
	3	-160(40)	150(30)	170(60)	280(40)	-690(30)	-350(70)
	5	-260(30)	160(30)	210(20)	0(30)	170(30)	30(30)

Table A.9: Quality of the fit to the Aramburu data after refinements of models of increasing complexity. Given are R values of each order ($|m|$) of reflections, the number of parameters, $(\Delta\rho)_{max}$, $(\Delta\rho)_{min}$ and the number of observed reflections $N(\text{obs})$.

Pulished data	Model A'	Model B'	Model C _r '	Model C'	Model D _r '	N(obs)
All	0.0827	0.0739	0.0726	0.0719	0.0717	1695
$m = 0$	0.0794	0.0763	0.0765	0.0770	0.0755	778
$ m = 1$	0.0751	0.0479	0.0458	0.0444	0.0453	473
$ m = 2$	0.2044	0.1452	0.1205	0.0968	0.1199	251
$ m = 3$	0.3470	0.2957	0.1716	0.1103	0.1759	53
$ m = 4$	—	—	—	—	—	—
$ m = 5$	0.2100	0.1909	0.1658	0.1339	0.1651	140
No. of parameters	115	199	331	443	364	
$(\Delta\rho)_{max}$ (e \AA^{-3})	2.74	2.49	2.27	2.28	2.35	
$(\Delta\rho)_{min}$ (e \AA^{-3})	-2.05	-1.91	-1.86	-1.76	-1.79	

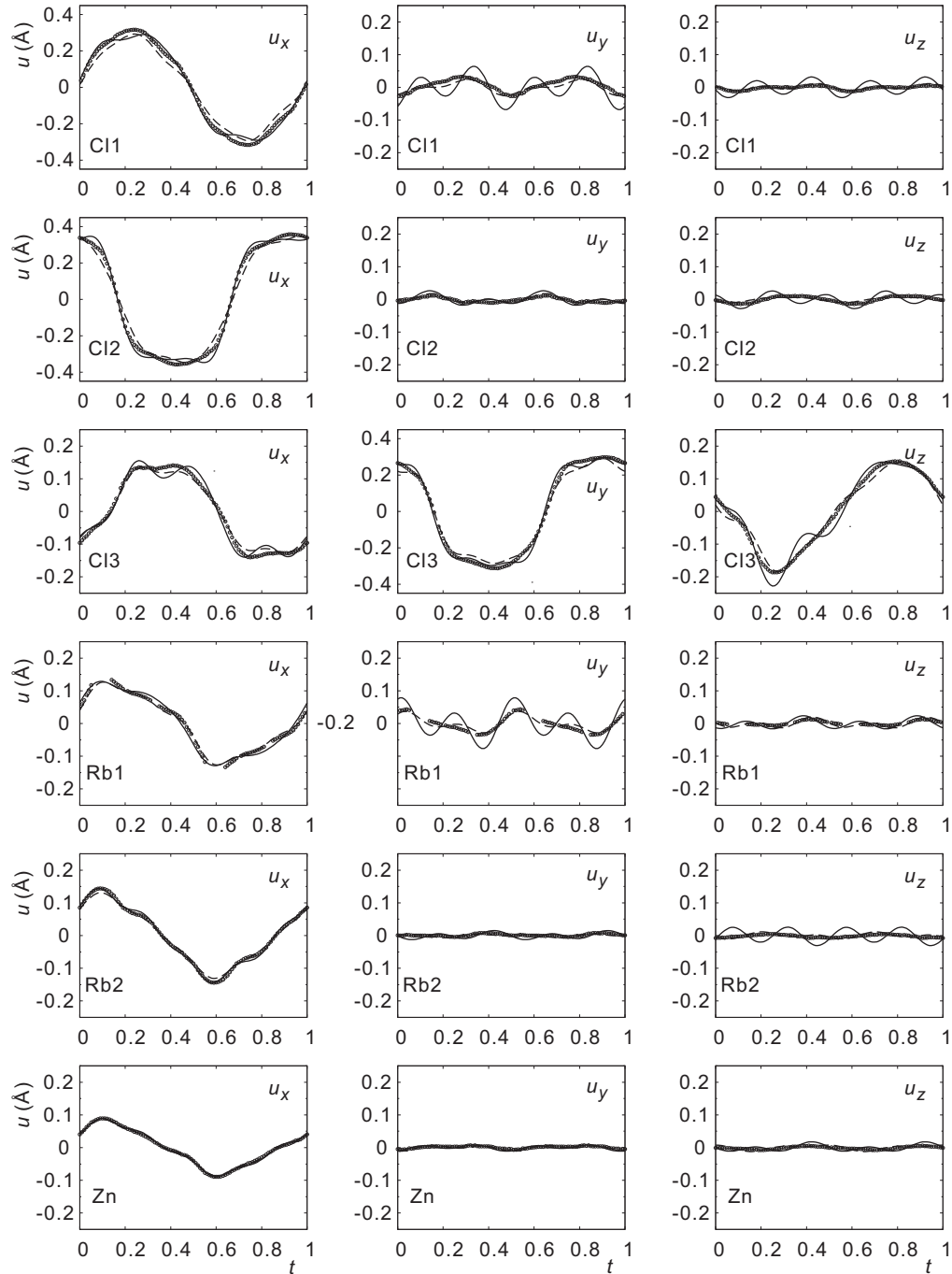


Figure A.1: Modulation functions of the crystallographically independent atoms of Rb_2ZnCl_4 of model A (real line) and model D_r (dashed line), Open circles are the center of charge. Displacement along x, y and z are given in Å.

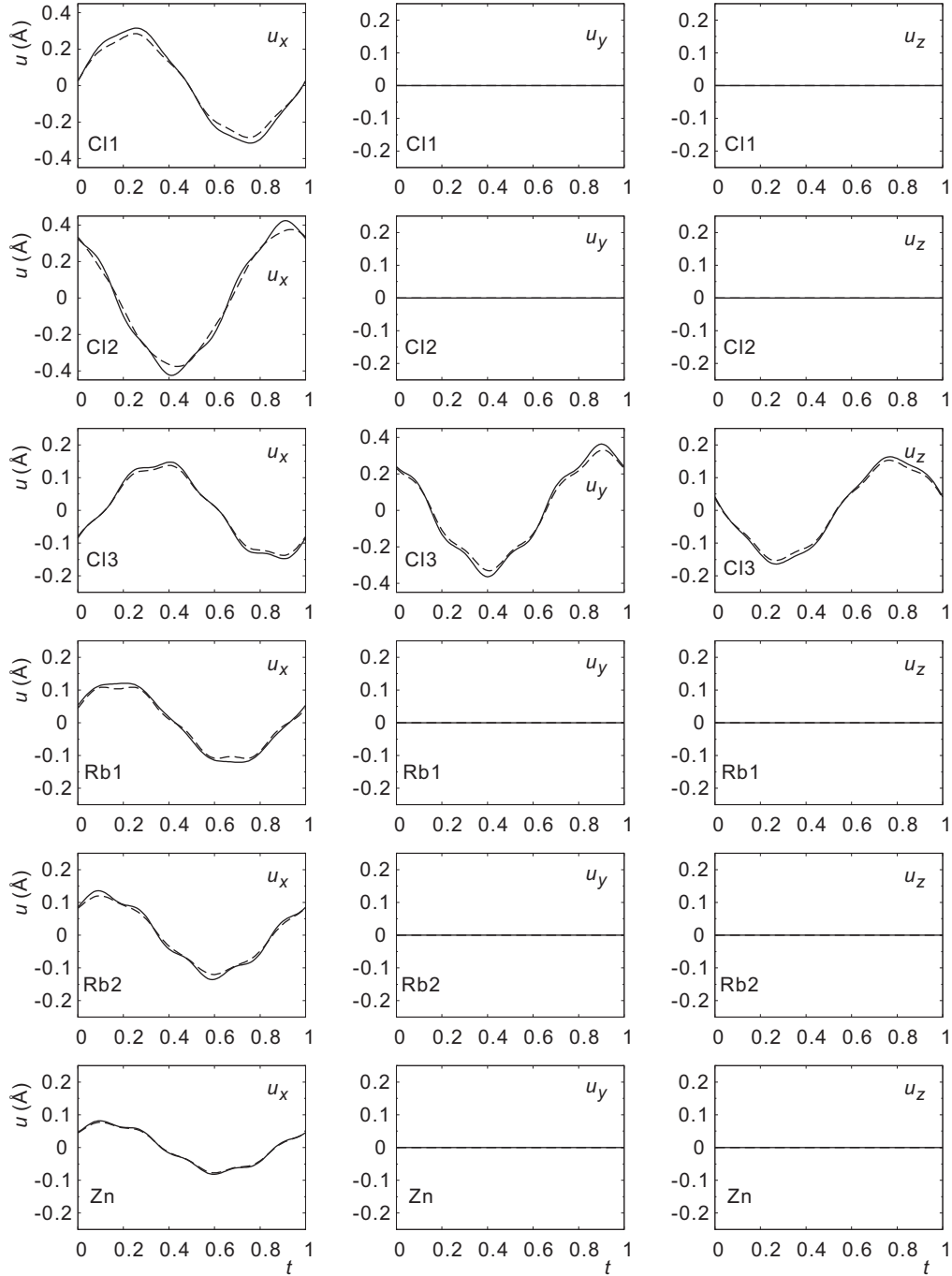


Figure A.2: Modulation functions only corresponding to the first and fifth-order harmonics of the crystallographically independent atoms of Rb_2ZnCl_4 of model A (full line) and model D_r (dashed line). Displacement along x, y and z are given in Å.

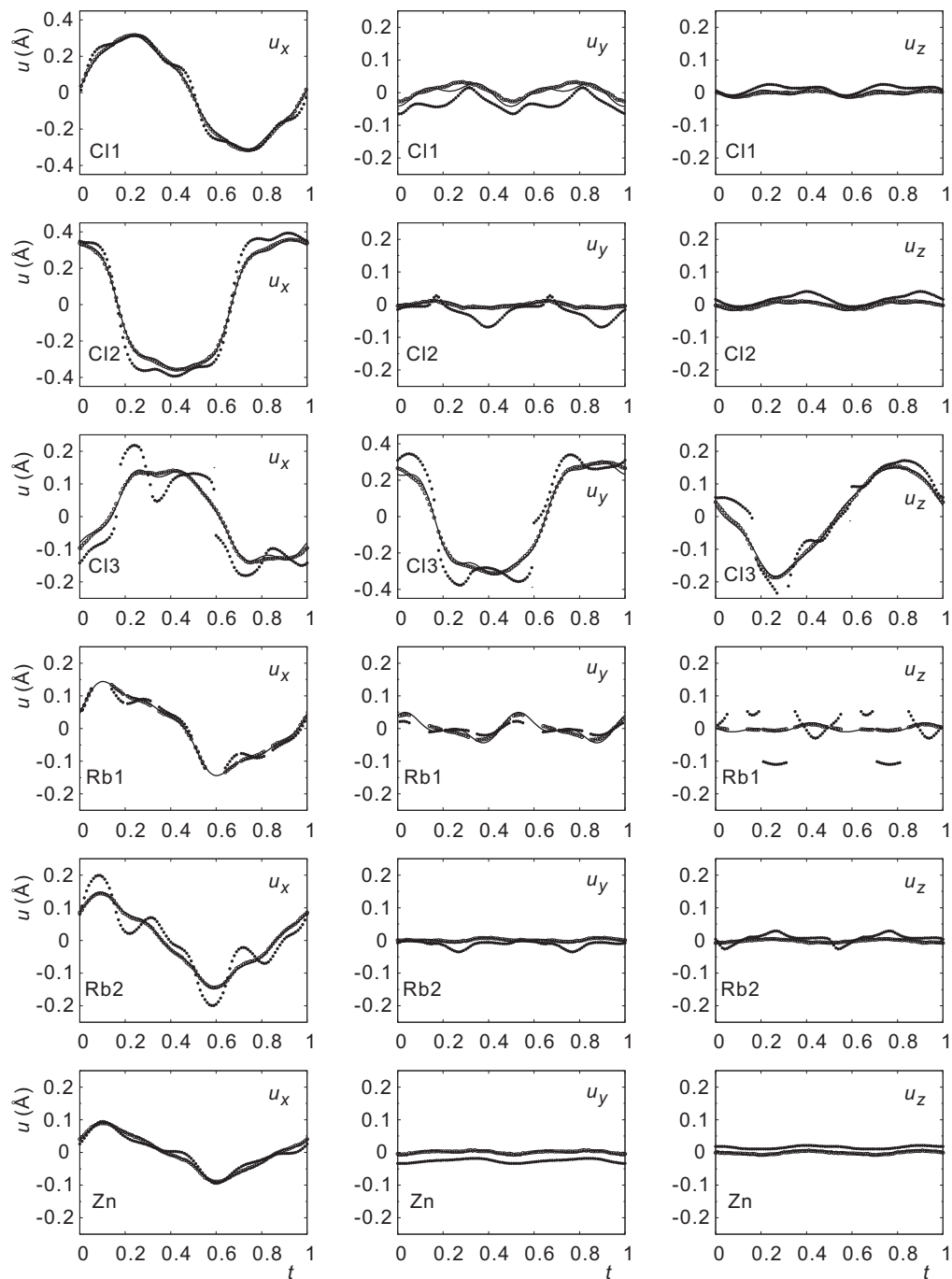


Figure A.3: Modulation functions of the crystallographically independent atoms of Rb_2ZnCl_4 . Displacement along x, y and z are given in Å. Open circles are the center of charge, filled circles are the maxima of electron density, real lines are the modulation function from model B.

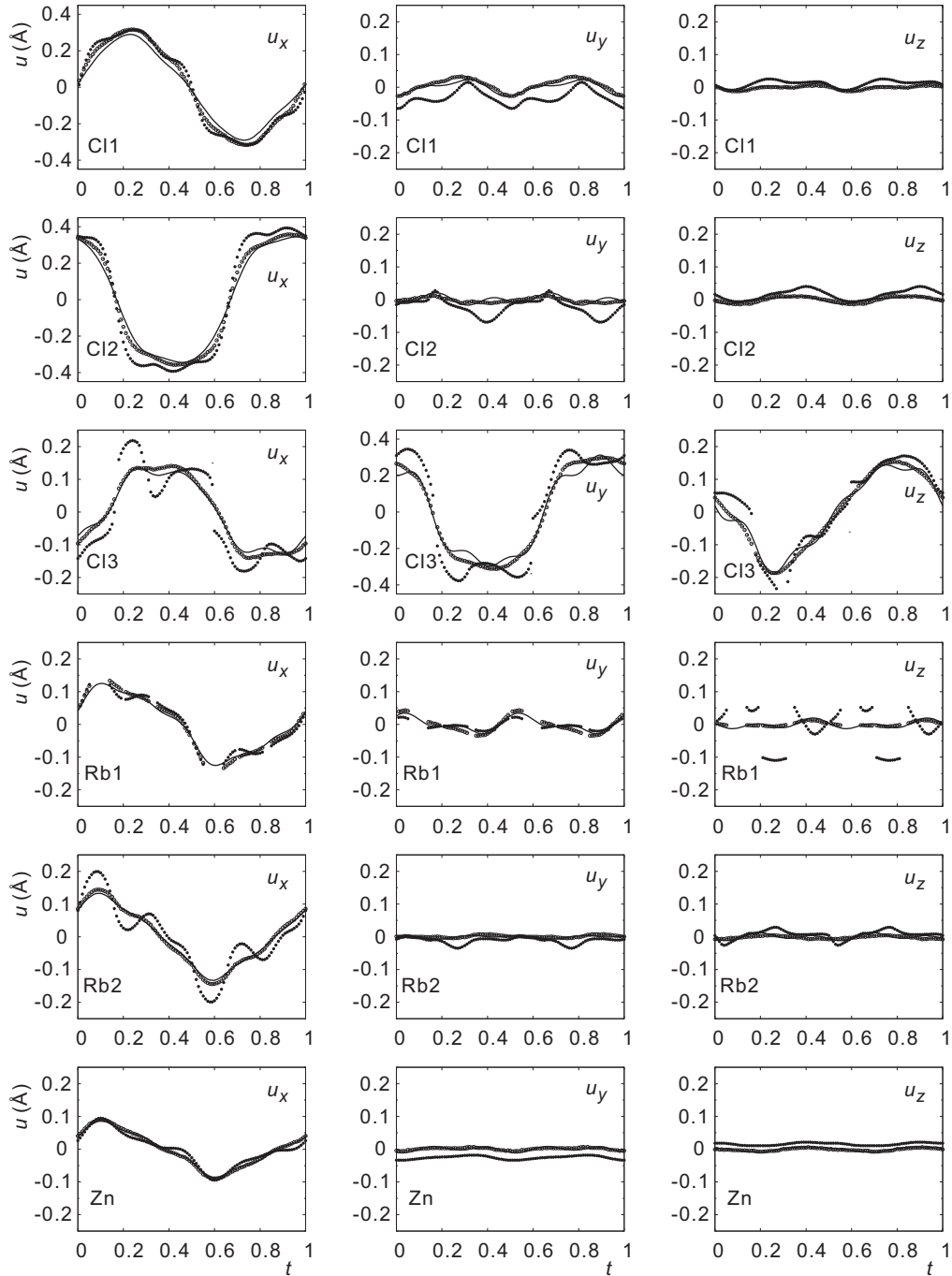


Figure A.4: Modulation functions of the crystallographically independent atoms of Rb_2ZnCl_4 . Displacement along x, y and z are given in \AA . Open circles are the center of charge, filled circles are the maxima of electron density, real lines are the modulation function from model C_r .

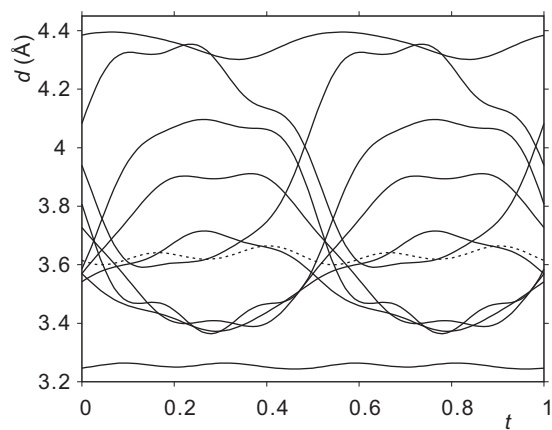


Figure A.5: Distance of atom Rb1 to its eleven caged Cl atoms, dashed line is made for clarity reason.

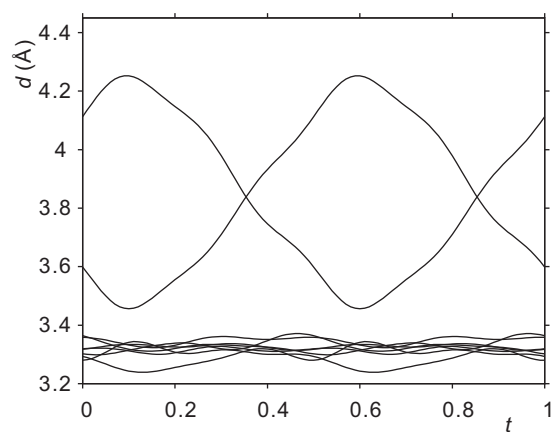


Figure A.6: Distance of atom Rb2 to its nine caged Cl atoms.

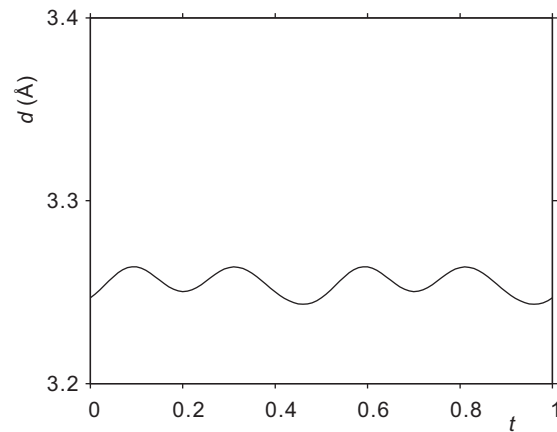


Figure A.7: Distance of atom Rb1 to atom Cl1(i) [symmetry code $(x_1, x_2, x_3 + 1, x_4)$].

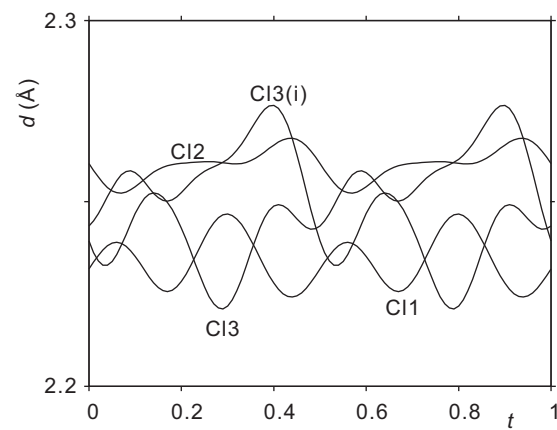


Figure A.8: Distance between atom Zn and the surrounding atoms Cl1, Cl2, Cl3 and Cl3(i) [symmetry code $(-x_1 + \frac{1}{2}, x_2, x_3, x_4 + \frac{1}{2})$].

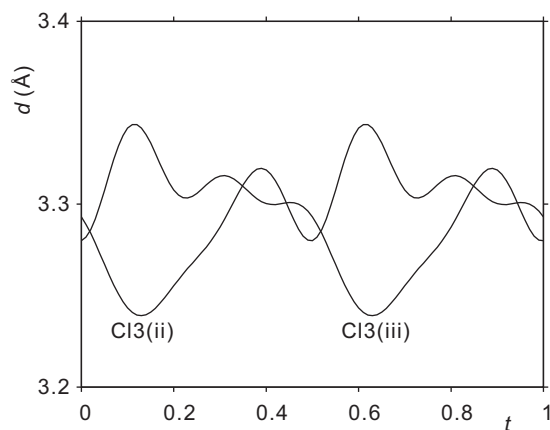


Figure A.9: Distance between atom Rb2 and two most near surrounding atoms Cl3(ii) [symmetry code $(-x_1, 1-x_2, 1-x_3, -x_4)$] and Cl3(iii) [symmetry code $(x_1 + \frac{1}{2}, 1-x_2, 1-x_3, -x_4 + \frac{1}{2})$].

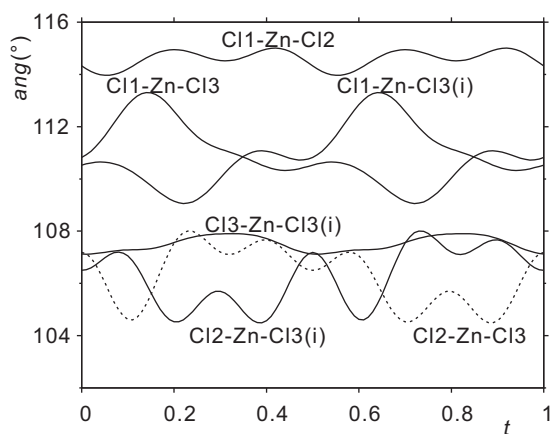


Figure A.10: Modulation of Cl-Zn-Cl angles, dashed line is made for clarity reason.

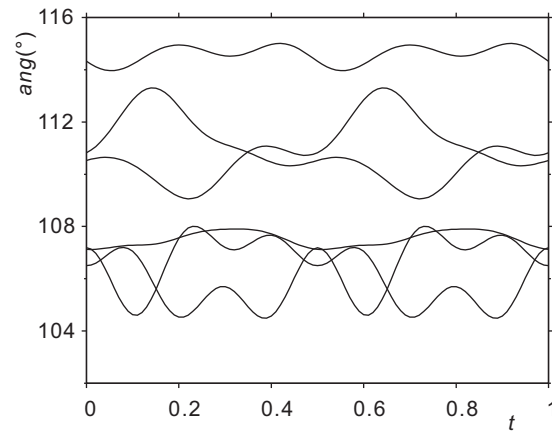


Figure A.11: Modulation of Cl-Zn-Cl angles, dashed line is made for clarity reason.

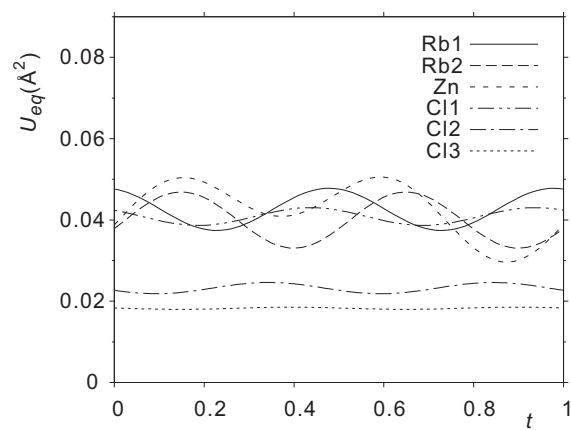


Figure A.12: Modulation of U_{eq} of atoms.

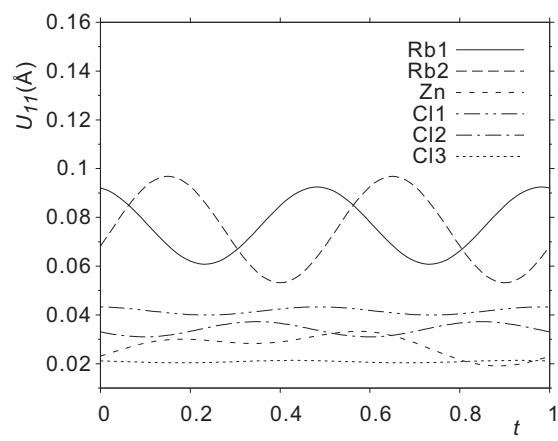


Figure A.13: Modulation of U_{11} of atoms.

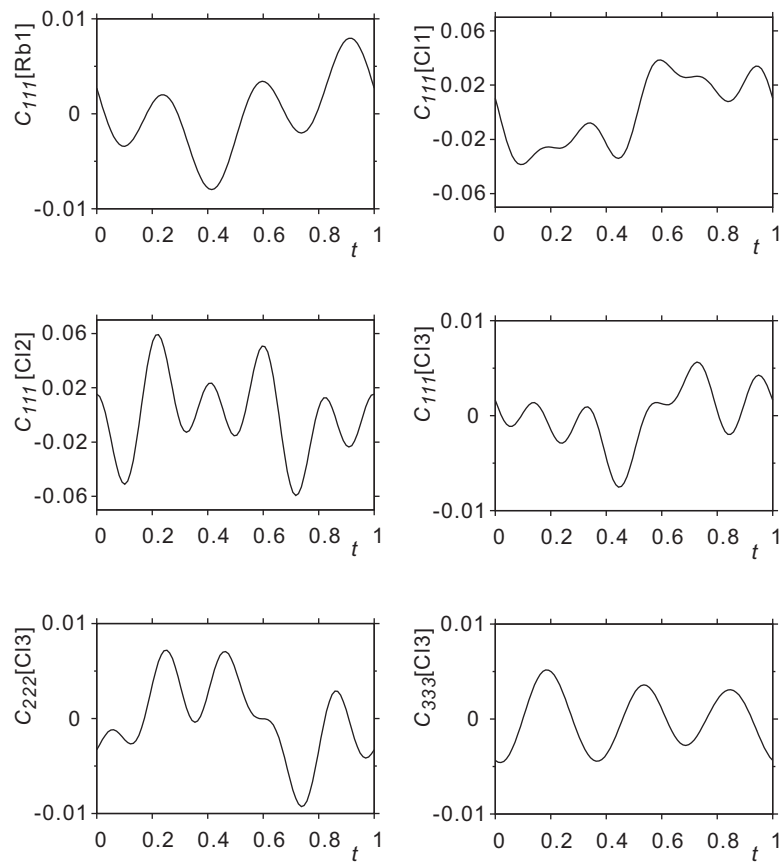


Figure A.14: Modulation of selected Gram-Charlier coefficients C_{ijk} of atoms.

Bibliography

- Aramburu, I., Friese, K., Pérez-Mato, J. M., Morgenroth, W., Aroyo, M., Breczewski, T. and Madariaga, G. (2006). Modulated structure of *rb2znc14* in the soliton regime close to the lock-in phase transition, *Phys. Rev. B: Condens. Matter* **73**: 014112.
- Aramburu, I., Madariaga, G., Grebille, D., Perez-Mato, J. M. and Breczewski, T. (1997). High-order diffraction satellites and temperature variation of the modulation in the incommensurate phase of *rb2znc14*, *J. Phys. I* **7**: 371–383.
- Bader, R. F. W. (1994). *Atoms in Molecules: A Quantum Theory*, Oxford University Press, Oxford.
- Bagautdinov, B., Luedecke, J., Schneider, M. and van Smaalen, S. (1998). Disorder in the crystal structure of Cs_2HgCl_4 studied by the maximum entropy method, *Acta Cryst. B* **54**: 626–634.
- Bricogne, G. (1988). A bayesian statistical theory of the phase problem. i. a multi-channel maximum-entropy formalism for constructing generalized joint probability distributions of structure factors, *Acta Cryst. A* **44**: 517–545.
- Castillo-Martínez, E., Schönleber, A., van Smaalen, S., Arévalo-López, A. M. and Alario-Franco, M. (2008). Structure and microstructure of the high pressure synthesized misfit layer compound $[\text{Sr}_2\text{O}_2][\text{CrO}_2]_{1.85}$, *J. Sol. State Chem.* **181**: 1840–1847.
- Cummins, H. Z. (1990). Experimental studies of structurally incommensurate crystal phases, *Phys. Rep.* **185**: 211–409.

- de Vries, R. Y., Briels, W. J. and Feil, D. (1994). Novel treatment of the experimental data in the application of the maximum-entropy method to the determination of the electron-density distribution from X-ray experiments, *Acta Cryst. A* **50**: 383–391.
- Dinnebier, R. E., Schneider, M., van Smaalen, S., Olbrich, F. and Behrens, U. (1999). Disorder determined by high-resolution powder diffraction: structure of pentamethylcyclopentadienyllithium, *Acta Cryst. B* **55**: 35–44.
- Dusek, M., Chapuis, G., Meyer, M. and Petricek, V. (2003). Sodium carbonate revisited, *Acta Crystallogr. B* **59**: 337–352.
- Dusek, M., Chapuis, G., Schobinger-Papamantellos, P., Wilkinson, C., Petricek, V., Tung, L. D. and Buschow, K. H. J. (2000). Modulated structure of $\text{La}_2\text{Co}_{1.7}$ from neutron and x-ray diffraction data, *Acta Crystallogr. B* **56**: 959–971.
- Fabry, J. and Perez-Mato, J. M. (1994). Some stereochemical criteria concerning the structural stability of A_2BX_4 compounds of type $\beta\text{-K}_2\text{SO}_4$, *Phase Transitions* **49**: 193–229.
- Friese, K., Madariaga, G. and Brezczewski, T. (2000). Incommensurately modulated phase Rb_2CoBr_4 at 295 and 200 k, *Acta Crystallogr. B* **56**: 17–21.
- Fuess, H. (ed.) (2006). *International Tables for Crystallography Vol. C*, Kluwer Academic Publishers, Dordrecht.
- Gilmore, C. J. (1996). Maximum Entropy and Bayesian statistics in crystallography: a review of practical applications, *Acta Cryst. A* **52**: 561–589.
- Glaum, R., Walter-Peter, M., Oezalp, D. and Gruehn, R. (1991). Beiträge zum thermischen Verhalten wasserfreier Phosphate. IV. Zum chemischen Transport von Pyrophosphaten $M_2P_2O_7$ ($m = \text{Mg, Cr, Mn, Fe, Co, Ni, Cu, Zn, Cd}$) — die erstmalige Darstellung von Chrom(II)-Pyrophosphat, *Z. Anorg. Allg. Chem.* **601**: 145–162.
- Gull, S. F. and Skilling, J. (1999). *MEMSYS5 v1.2 program package*, Maximum Entropy Data Consultants Ltd., OSuffolk, U.K.

- Hofmann, A., Netzel, J. and van Smaalen, S. (2007). Accurate charge density of Tri-alanine: A comparison of the multipole formalism and the maximum entropy method (MEM), *Acta Cryst. B* **63**: 285–295.
- Janssen, T., Chapuis, G. and de Boissieu, M. (2007). *Aperiodic Crystals. From Modulated Phases to Quasicrystals*, Oxford University Press (United Kingdom).
- Jaynes, E. T. (1957). Information theory and statistical mechanics, *Phys. Rev.* **106**(4): 620–630.
- Jobst, A. and van Smaalen, S. (2002). Intersubsystem chemical bonds in the misfit layer compounds $(\text{LaS})_{1.13}\text{TaS}_2$ and $(\text{LaS})_{1.14}\text{NbS}_2$, *Acta Crystallogr. B* **58**: 179–190.
- Kruger, H., Kahlenberg, V. and Friese, K. (2006). $\text{Na}_2\text{Si}_3\text{O}_7$: an incommensurate structure with crenel-type modulation functions, refined from a twinned crystal, *Acta Crystallogr. B* **6**: 440–446.
- Kumazawa, S., Takata, M. and Sakata, M. (1995). An accurate determination of the thermal vibration of rutile from the nuclear density distribution of the maximum-entropy analysis, *Acta Cryst. A* **51**: 651–658.
- Li, L., Schönleber, A. and van Smaalen, S. (2010). Modulation functions of incommensurately modulated $\text{Cr}_2\text{P}_2\text{O}_7$ studied by the maximum entropy method (MEM), *Acta Crystallogr. B* **66**: 130–140.
- McMahon, M. I., Degtyareva, O., Nelmes, R. J., van Smaalen, S. and Palatinus, L. (2007). Incommensurate modulations of Bi-III and Sb-II, *Phys. Rev. B: Condens. Matter* **75**: 184114.
- Netzel, J., Hofmann, A. and van Smaalen, S. (2008). Accurate charge density of α -glycine by the maximum entropy method, *Cryst. Eng. Comm* **10**: 335–343.
- Nishibori, E., Terauchi, I., Sakata, M., Takata, M., Ito, Y., Sugai, T. and Shinohara, H. (2006). High-resolution analysis of $(\text{Sc}_3\text{C}_2)\text{@C}_{80}$ metallofullerene by third generation synchrotron radiation x-ray powder diffraction, *J. Phys. Chem. B* **110**: 19215–19219.

- Oxford-Diffraction (2006). CrysAlis. Oxford Diffraction Ltd, Abingdon, England.
- Palatinus, L., Amami, M. and van Smaalen, S. (2004). The crystal structure of incommensurate ammonium tetrafluoroberyllate studied by structure refinements and the maximum entropy method, *Acta Crystallogr. B* **60**: 127–137.
- Palatinus, L., Dušek, M., Glaum, R. and El Bali, B. (2006). The incommensurately and commensurately modulated crystal structures of chromium(II) diphosphate, *Acta Cryst. B* **62**: 556–566.
- Palatinus, L. and van Smaalen, S. (2002). The generalized F -constraint in the Maximum Entropy Method—a study on simulated data, *Acta Cryst. A* **58**: 559–567.
- Palatinus, L. and van Smaalen, S. (2004). Incommensurate modulations made visible by the maximum entropy method in superspace, *Z. Kristallogr.* **219**: 719–729.
- Paulmann, C. (2009). Personal communication.
- Perez-Mato, J. M., Madariaga, G. and Elcoro, L. (1991). Influence of phason dynamics on atomic debye-waller factors of incommensurate modulated structures and quasicrystals, *Solid State Commun.* **78**: 33–37.
- Petricek, V., Dusek, M. and Palatinus, L. (2006). *The crystallographic computing system JANA2006*, Institute of Physics, Praha, Czech Republic.
- Roussel, P., Labidi, O., Huvea, M., Drache, M., Wignacourt, J.-P. and Petricek, V. (2009). The incommensurately modulated crystal structure of beta-Pb₂NiVO₆: interpretation of the phase transition alpha → beta → delta and conduction properties of related materials, *Acta Crystallogr. B* **65**: 416–425.
- Sakata, M. and Sato, M. (1990). Accurate structure analysis by the maximum-entropy method, *Acta Cryst. A* **46**: 263–270.
- Samy, A., Dinnebier, R. E., van Smaalen, S. and Jansen, M. (2010). Maximum entropy method and charge flipping, a powerful combination to visualize the true

- nature of structural disorder from *in situ* X-ray powder diffraction data, *Acta Crystallogr. B* **66**(2): 184–195.
- Sawada, S., Shiroishi, Y., Yamamoto, A., Takashige, M. and Matsuo, M. (1977). Ferroelectricity in rb_2zncl_4 , *J. Phys. Soc. Jpn.* **43**(6): 2099–2100.
- Schneider, M. and van Smaalen, S. (2000). Discrete Fourier transform in arbitrary dimensions by a generalized Beavers–Lipson algorithm, *Acta Cryst. A* **56**: 248–251.
- Schreurs, A. M. M., Xian, X. and Kroon-Batenburg, L. M. J. (2010). *EVAL15* : a diffraction data integration method based on *ab initio* predicted profiles, *J. Appl. Cryst.* **43**: 70–82.
- Shechtman, D., Blech, I., Gratias, D. and Cahn, J. W. (1984). Metallic phase with long-range orientational order and no translational symmetry, *Phys. Rev. Lett.* **53**(20): 1951–1953.
- Sheldrick, G. M. (1996). SADABS. University of Göttingen, Germany.
- Skilling, J. and Bryan, R. K. (1984). Maximum entropy image reconstruction: General algorithm, pp. 111–124.
- Steurer, W. (2004). Twenty years of structure research on quasicrystals. part 1. pentagonal, octagonal, decagonal and dodecagonal quasicrystals, *Z. Kristallogr.* **219**: 391–446.
- Takata, M. (2008). The MEM/Rietveld method with nano-applications—accurate charge-density studies of nano-structured materials by synchrotron-radiation powder diffraction, *Acta Cryst. A* **64**: 232–245.
- van Smaalen, S. (2007). *Incommensurate Crystallography*, Oxford University Press, Oxford.
- van Smaalen, S. and Li, L. (2009). Modulation functions of aperiodic crystals by the maximum entropy method in superspace, *Phys. Scr.* **79**: 048305.

- van Smaalen, S. and Netzel, J. (2009). The maximum entropy method in accurate charge-density analysis, *Phys. Scr.* **79**: 048304.
- van Smaalen, S., Palatinus, L. and Schneider, M. (2003). The maximum entropy method in superspace, *Acta Cryst. A* **59**: 459–469.
- Wang, C.-R., Kai, T., Tomiyama, T., Yoshida, T., Kobayashi, Y., Nishibori, E., Takata, M., Sakata, M. and Shinohara, H. (2001). A scandium carbide endohedral metallofullerene: $(\text{Sc}_2\text{C}_2)@C_{84}$, *Angew. Chem. Int. Ed.* **40**: 397–339.
- Yamamoto, A., Weber, S., Sato, A., Kato, K., Ohshima, K.-i., Tsai, A. P., Niikura, A., Hiraga, K., Inoue, A. and Masumoto, T. (1996). Electron density of icosahedral Zn–Mg–Y quasicrystals determined by a six-dimensional maximum entropy method, *Philos. Mag. Lett.* **73**: 247–254.

Publications

Parts of this thesis published in the international scientific literature or will be submitted for publication:

Chapter 5:

L. Li, A. Wölfel, A. Schönleber, S. Mondal, A. Schreurs, L. Kroon-Batenburg, S. Van Smaalen

Incommensurately modulated structure of Rb_2ZnCl_4 studied by the Maximum Entropy Method (MEM).

Will be submitted to *Acta Crystallographica B*.

Chapter 6:

L. Li, A. Schönleber, S. Van Smaalen.

Structure of incommensurately modulated chromium pyrophosphate studied by Maximum Entropy Method (MEM).

Journal of Physics: Conference Series, **226**, 012012 (2010).

Chapter 6:

L. Li, A. Schönleber, S. Van Smaalen.

Modulation functions of incommensurately modulated $\text{Cr}_2\text{P}_2\text{O}_7$ studied by the Maximum Entropy Method.

Acta Crystallographica B, **66**, 130 (2010).

Chapter 6:

S. Van Smaalen, L. Li.

Modulation functions of aperiodic crystals by the maximum entropy method in superspace.

Physica Scripta, **79**, 048305 (2009).

Acknowledgements

The first and most gratitude is given to my 'Doctorvater' Prof.dr. Sander van Smaalen, who has offer me a chance for Doctor study in Bayreuth. During this three and half years study, Sander helped me with basic knowledge, method, idea of project and writing articles, but he changed my attitude to scientific work virtually, he sucessfully improved the precision of my brain from hundredth of his to about tenth, this will affect me for life time. Dr Andreas schönleber helped me with the Zusammenfassung of this thesis. He always shows me his attitude and idea of the whole life, and these already become part of my own. The atmosphere in the team of the Laboratory of Crystallography is friendly and let me feel at home. Thank all of you for help in daily life, technical surpporting and fruitful discussions: Denise Kelk-Huth, Franz Fischer, Alfred Suttner , SK Imran Ali, Dr. Joachim Angelkort, Dr. Julian Henn, Prathapa Siriyara Jagannatha, Dr. Swastik Mondal, Dr. Jeanette Netzel, Alexander Wölfel and Zhang Jian. My acknowledgement specially goes to my wife Gao Yi for her comprehension and support.

Declaration

Die Dissertation wurde von mir selbstständig und nur unter Verwendung von zulässigen Hilfsmitteln erstellt.

Bayreuth, 2010

Li Liang

